Aus dem Institut für Physik der Universität Potsdam

ON THE RELEVANCE OF PARTICLE ADHESION: APPLICATIONS TO SATURN'S RINGS

Dissertation

zur Erlangung des akademischen Grades
„doctor rerum naturalium“
(Dr. rer. nat.)
in der Wissenschaftsdisziplin Theoretische Physik

eingereicht an der
Mathematisch-Naturwissenschaftlichen Fakultät
der Universität Potsdam

von

Nicole Albers

Potsdam, im Mai 2006

Abstract

Since their discovery in 1610 by Galileo Galilei, Saturn's rings continue to fascinate both experts and amateurs. Countless numbers of icy grains in almost *Keplerian* orbits reveal a wealth of structures such as ringlets, voids and gaps, wakes and waves, and many more. Grains are found to increase in size with increasing radial distance to Saturn. Recently discovered "propeller" structures in the *Cassini* spacecraft data, provide evidence for the existence of embedded moonlets. In the wake of these findings, the discussion resumes about origin and evolution of planetary rings, and growth processes in tidal environments.

In this thesis, a contact model for binary adhesive, viscoelastic collisions is developed that accounts for agglomeration as well as restitution. Collisional outcomes are crucially determined by the impact speed and masses of the collision partners and yield a maximal impact velocity at which agglomeration still occurs. Based on the latter, a self-consistent kinetic concept is proposed. The model considers all possible collisional outcomes as there are coagulation, restitution, and fragmentation. Emphasizing the evolution of the mass spectrum and furthermore concentrating on coagulation alone, a coagulation equation, including a restricted sticking probability is derived. The otherwise phenomenological *Smoluchowski* equation is reproduced from basic principles and denotes a limit case to the derived coagulation equation.

Qualitative and quantitative analysis of the relevance of adhesion to force-free granular gases and to those under the influence of *Keplerian* shear is investigated. Capture probability, agglomerate stability, and the mass spectrum evolution are investigated in the context of adhesive interactions. A size dependent radial limit distance from the central planet is obtained refining the *Roche* criterion. Furthermore, capture probability in the presence of adhesion is generally different compared to the case of pure gravitational capture. In contrast to a *Smoluchowski*-type evolution of the mass spectrum, numerical simulations of the obtained coagulation equation revealed, that a transition from smaller grains to larger bodies cannot occur via a collisional cascade alone. For parameters used in this study, effective growth ceases at an average size of centimeters.

Meinen Großeltern

Contents

Chapter 1

Introduction

Granular matter is defined as a large collection of mesoscopic objects which interact via inelastic collisions. Mesoscopic is a relative term ranging from submicron dust particles to millimeter size sand grains to boulder size rocks within planetary rings to even automobiles in traffic flow. Granular matter can be further classified as granular solids, granular liquids, and granular gases. The different physical states describe different density packings. This at first glance exotic matter can be found in everyday life in form of sugar, coffee powder, bottles, etc. Most commonly know to anyone from childhood, sand provides the best example of granular matter. Dry sand alone comes in various appearances and can be used to build "solid" castles or "flow" down a sandpile in an avalanche. As examples of granular matter cover as wide range, so do its applications. Industrial interest are high and concentrate on transport problems. These may concern pharmaceutical products, fruits or corn (Gan-Mor and Galili, 2000), or even traffic flows in congested areas (Wolf et al., 1996; Helbing, 2001).

Granular gases are dilute systems of granular matter and are treated according to thermodynamics and kinetic theory of gases. It is sufficient to consider binary contacts which are merely inelastic, physical collisions among constituents. This energy dissipation is mainly responsible for structure evolution, clustering, and the permanent cooling of ensembles in the absence of external energy sources (Haff, 1986; Petzschmann et al., 1999). Although these systems are usually in non-equilibrium states, they are attributed with typically equilibrium terms as e.g. temperature. In general, a granular temperature is defined via the mean random velocity of the ensemble. However, under anisotropical conditions one isotropic temperature is no longer sufficient and has to be replaced by a temperature tensor. Apart from theoretical considerations, experimental realizations of granular gases are rather hard to achieve, since earth-bound laboratories are subject to gravity.

The most spectacular granular gases cannot be found on Earth but in space. Planetary rings, surrounding all the giant planets of the Solar system, are truly beautiful examples of their kind. Countless numbers of particles ranging in size from microns up to house-sized boulders revolve the central planet on almost *Keplerian* orbits and thereby create a wealth of features such as voids and gaps, ringlet structures, waves and wakes, "spokes", "propellers", and many more. Displaying a variety of masses, sizes, and physical processes, ring systems around Jupiter, Saturn, Uranus, and Neptune, although being generally alike, are as different from one another as one can imagine (see Burns, 1999; Esposito, 2002, for a general introduction).

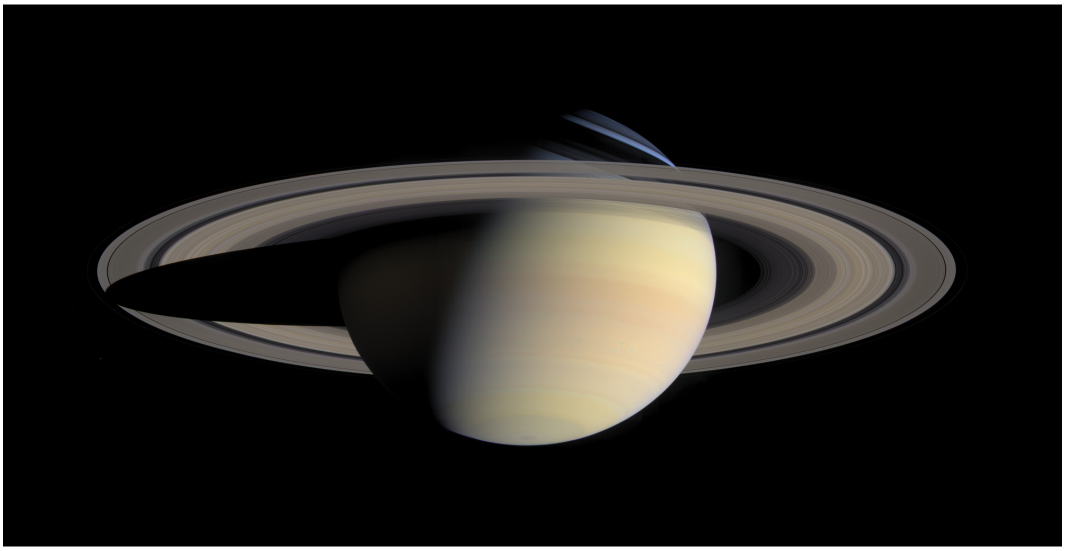

Figure 1.1: An image of Saturn and its main rings taken by the *Cassini* spacecraft (Planetary Photojournal, JPL, PIA06193) while approaching the planet in 2004. The A ring (outermost) and the brighter B ring are separated by the darker *Cassini* division. A much fainter ring, the C ring, lies yet inside the B ring. The *Cassini* division was the first structure observed in 1675 by Giovanni Cassini and has been associated with the proof that the ring is divided into many ringlets.

Yet common to planetary rings is their existence inside the *Roche* limit of any of the giant planets. The *Roche* limit denotes the distance from the central planet inside which a fluid particle would be disrupted by tidal stresses (Roche, 1847; Chandrasekhar, 1969; Albers and Spahn, 2005). Latter become more important closer to the planet and compete against coagulation[1]. James Clark Maxwell in 1859 already noted that the tendency of particles to coagulate into narrow rings opposes the disintegration process. Closely connected to this fact is the question about the origin and formation of planetary ring systems. While there are two major theories none specific could be singled out so far. On one hand, rings may originate from the same process as regular satellites and are simply the uncoagulated remnants of satellites that failed to form (Harris, 1984; Esposito, 2002). Clearly, in this case they must be as old as the Solar system. On the other hand, they may be simply the result of a disruption from a preexisting body. This could either mean a satellite previously in orbit around Saturn (Colwell and Esposito, 1992, 1993; Colwell et al., 2000) or remnants of a comet that came too close to the central planet (Dones, 1991). Tiscareno et al. (2006, (Spahn and Schmidt, 2006); see also Fig.1.4) discovered four building-sized moonlets in the Saturn A ring. They argue in favor of the latter formation scenario. However, the question of origin still remains open.

Apart from these more general questions, three size populations have to be mentioned: dust (spreading throughout the entire system), centimeter sized grains to boulders of tens of me-

---

[1] Coagulation, aggregation, and agglomeration are widely used throughout this thesis. In principle denoting different physical scenarios, they will be referred to the same thing, i.e. the sticking of two grains nevertheless if they form a new spherical grain or retain their shape. Otherwise, coagulation refers to the merging of two droplets while agglomeration and aggregation refer to the simple attachment of two grains without changing their shape.

ters (making up the main rings in case of Saturn), and moonlets up to satellites dominating the outer regions. These populations interact in form of resonances and gaps in the rings, created by satellites or embedded moons found to be coexisting within the *Roche* zone (Sicardy, 2005). The dynamics of a dense planetary ring is mainly determined by the gravity of the central body and the ring itself as well as by mutual inelastic collisions among the constituent grains. Energy is constantly being replenished due to viscous shearing. This is a result of the collective motion in the central gravity field, which in turn will be dissipated as heat during particle encounters. Mutual particle collisions are the main source of dissipation. The conserved angular momentum, on one hand, and inelastic particle collisions on the other are reasons for the extremely low vertical height of a planetary ring (Schmidt et al., 1999). Viscous heating due *Keplerian* shear balances the energy loss due to inelastic collisions. A quasi-equilibrium granular temperature crucially determines lifetimes and structures of the rings (Goldreich and Tremaine, 1978). The vertical extent or the ring is correlated to its granular temperature. The dust population, having a larger random walk speed, shows a broader spatial distribution than meter-sized grains. This segregation in size does not only appear on vertical scale but radially as well. While being by far thinner than 100 meters the radial extent of Saturn's rings is more than $120,000$ kilometers.

In contrast to the previously mentioned dense rings, dusty rings as e.g. the tenuous Jovian rings or the G and E ring of Saturn are not driven by collisions. Dust grains, generally charged, are subject to a variety of perturbing non-gravitational forces such as the Lorentz force due to the magnetic field of the central planet, direct Solar radiation pressure, Pointing-Robertson drag, or plasma drag. The E ring is the broadest ring of the Saturn system where dust is thought to originate from the surfaces of embedded moons (Showalter et al., 1991; Horanyi et al., 1992; Hamilton and Burns, 1994; Spahn et al., 1999, 2006a). As in case of the Jovian moons, their surfaces are exposed to a continuous bombardment of micrometeroids (Krivov et al., 2003; Sremčević et al., 2003, 2005). Enceladus, one of the embedded moons among Rhea, Tethys, and Mimas, recently made headlines for its prominent south pole source of dust (Spahn et al., 2006b), which proves to be the dominant source to replenish the E ring. Another example of optically thin dusty structures are Martian dust tori, first proposed by Soter (1971). These putative dusty complexes, originating from the Martian satellites Phobos and Deimos, still remain undetected, but are theoretically studied in great detail (e.g. Krivov and Hamilton, 1997; Makuch et al., 2005, 2006).

Saturn's rings are by far the most prominent and best studied among planetary rings. Since their discovery in 1610 by Galileo Galilei, they continue to fascinate both experts and amateurs. The rings mainly consist of icy grains as it has been inferred from spectrometry measurements (Planetary Photojournal, JPL, PIA05075). Radio occultation data suggests grain sizes ranging from centimeters up to tens of meters in the main rings (Marouf et al., 1983; Zebker et al., 1985; Showalter and Nicholson, 1990). Grains show no significant water ice pollution due to micrometeoroid bombardment (Cuzzi and Estrada, 1998). This points to rather young or freshly replenished material. Evidence from the Visual and Infrared Mapping Spectrometer (VIMS) of the *Cassini* spacecraft (Planetary Photojournal, JPL, PIA06349), see Fig. 1.2) suggests larger grain sizes with increasing distance to Saturn.

The *Roche* limit, as mentioned above, marks the borderline to denote the onset of growth processes and the existence of satellites. The disruption of a solid body with finite internal strength has been analyzed in various studies and a critical distance to a central body as a

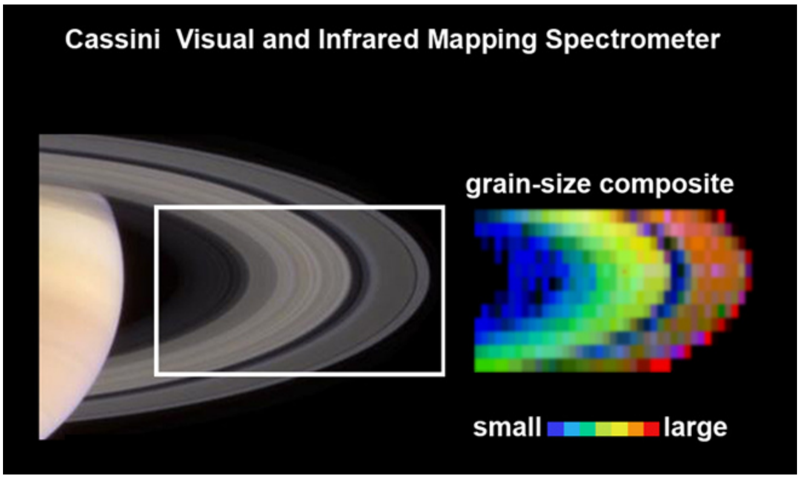

Figure 1.2: An increasing grain size is indicated by data from the visual and infrared mapping spectrometer (VIMS) on board of the *Cassini* spacecraft (Planetary Photojournal, JPL, PIA06349). Tidal shear counteracting agglomeration can be responsible for an radially dependent, upper limit size of the size distribution.

function of the satellite's size has been obtained (Aggarwal and Oberbeck, 1974; Dobrovolskis, 1990; Davidsson, 1999, 2001). Accretion within the *Roche* zone could yield temporary aggregates such as dynamic ephemeral bodies (DEBs) (Weidenschilling et al., 1984). Regions featuring a vivid size distribution dynamics such as the prominent F ring (Showalter et al., 1992; Porco et al., 2005) provoke questions about the likeliness of growth processes. The possibility of particles sticking has been inferred from laboratory experiments (Hatzes et al., 1991; Tremaine, 2003) but still lacks a theoretical modeling. However, a more detailed model of particle interactions including adhesive effects has not been studied in detail up to now but could significantly help to understand size and velocity distributions that are otherwise still poorly known. The relevance of particle adhesion is still putative.

Recently, propeller structures have been discovered in *Cassini* data (Tiscareno et al., 2006; Spahn and Schmidt, 2006) clearly indicating the existence of embedded moonlets as predicted by Showalter et al. (1986) (Spahn and Wiebicke, 1988; Spahn and Sremčević, 2000; Sremčević et al., 2002). Embedded moons can create gaps in the rings and leave traces as wavy, gap edges. This lead to the prediction of the existence of the moon Pan (Showalter et al., 1986; Spahn and Sponholz, 1989) which has later on been discovered while carefully re-examining *Voyager* data (Showalter, 1991). Since with the current technology moonlets escape direct detection, they may only be observed indirectly with respect to structures they produce (Seiß et al., 2005). There are, for instance, plenty of clumpy rings or ringlets that could be explained by embedded but yet unseen moons. In case of the F ring, those moonlets denote a reasonable explanation (Kolvoord et al., 1990; Kolvoord and Burns, 1992) to account for its azimuthal structure. Larger clumps are submitted to fragmenting and accreting collisions and thereby release large amounts of temporary dust (Barbara and Esposito, 2002), which could support the observed vivid size distribution (Murray et al., 1997; Poulet et al., 2000b). Particles, clumps, and moonlets are constantly fragmenting, eroding, but also recreating in agglomeration (Esposito et al., 2006) leaving questions about the age and origins about these moonlets in the same way as does apply to the entire ring system. In the light of these newly attained data from the *Cassini* spacecraft the discussion freshly

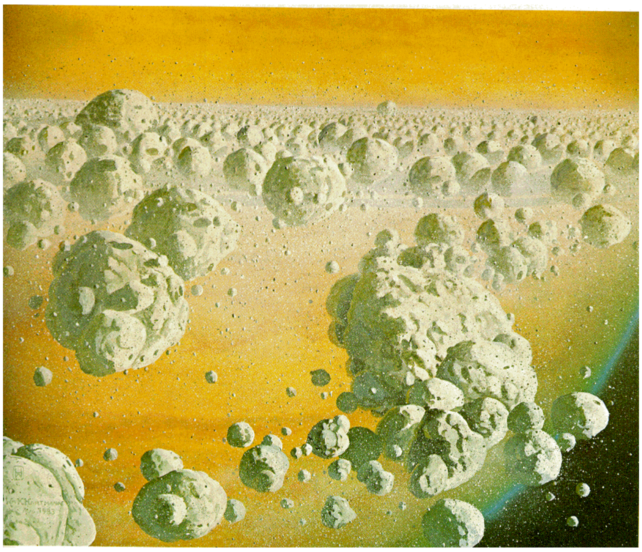

Figure 1.3: ”Dynamical Ephemeral Bodies” in the rings of Saturn as imagined by William K. Hartmann. From this position, Saturn fills most of the image in the background. Particles might temporarily aggregate into larger bodies, eventually sheared apart again by dynamical forces in the rings. Jacques Cassini, son of Giovanni Cassini, suggested in 1715 that the rings are made of many small satellites orbiting the planet which, however, are too small to be seen. Later, at the end of the 18^{th} century, Laplace proved the rings ringlet structure on the base of centrifugal forces.

resumes, whether these moonlets are remnants of a catastrophic disruption of a former satellite or were formed and reshaped by accretion and fragmentation during the evolution of the rings.

The question about planet formation is, besides appearance and evolution of planetary rings, another interesting subject where the theory of granular gases is applied. After gas of the pre-planetary disk condensated into heavy elements, cohesive collisions of grains lead to the formation of yet larger bodies (Hartmann, 1978; Weidenschilling et al., 1984). So called planetesimals will then either grow via further cohesive collisions or through gravitational instability (Safronov, 1969; Goldreich and Ward, 1973) and will eventually form protoplanets. The nonlinear increase of a privileged planetesimal’s cross section together with an almost steady granular temperature of smaller grains leads to the so-called “runaway” growth of the largest planetesimal in a certain region. This considerably amplifies the growth of planets (Wetherill, 1990; Wetherill and Stewart, 1993).

The formation of planets according to these current theories crucially depends on whether collisional growth is possible. How smaller grains aggregate up to planetesimals sizes is still not fully understood. The link between grains and planetesimals could be the “missing” link of planetogeny. Since experiments in this field of research are restricted to numerical simulations only, planetary rings may serve as a “laboratory” for planet formation scenarios. Although we are merely deemed to observe than to actually set up an experiment, understanding their dynamics is promising. It may provide answers to whether larger bodies can grow in a tidal environment and if it occurs via a collisional cascade of agglomeration as currently assumed. Since mutual collision, either scattering or physical ones, shape a

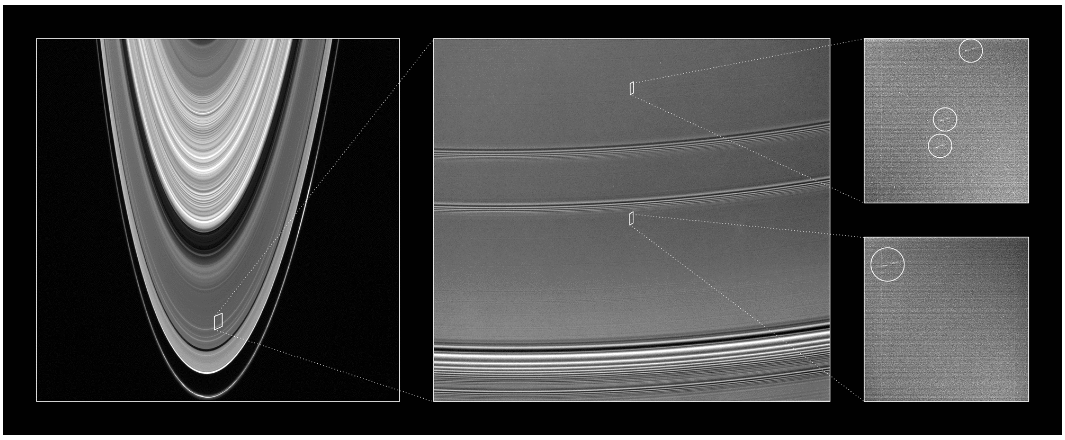

Figure 1.4: Collection of images of the *Cassini* spacecraft taken during orbit insertion in July 2004 (Planetary Photojournal, JPL, PIA07792). The most left part of the figure shows Saturn's main rings where the narrow F ring (bottom structure) is clearly separated from the A ring. Further up, the dark *Cassini* division and brighter B ring can be seen. As theoretically predicted, propeller like structures were found indicating the existence of embedded moonlets (Tiscareno et al., 2006). They are highlighted in the two close-up of an A ring region. Raising questions about origin and formation of the ring itself, these structures belong to one of the most striking findings of the *Cassini* mission.

planetary ring, collisions could bear the answers to at least some issues.

Since the *Cassini* spacecraft entered orbit around Saturn in July 2004, it continues to transmit astonishing data and pictures with resolutions so far unreached. A more detailed understanding of the underlying, physical collision dynamics together with a combined kinetic treatment may grasp the very essence of planetary rings.

This thesis proposes a contact model for adhesive, viscoelastic collisions of solid, homogeneous spheres. The model allows for agglomeration as well as restitution. Influences on the stability of agglomerates and capture probability in a gravitational field of a central body are discussed. Furthermore, a general kinetic concept is proposed and discussed in the context of growth processes based on the introduced collision dynamics. This work is organized as follows: Chapter 2 introduces a model of granular particle collisions. After commemorating the basics of contact dynamics, adhesive, viscoelastic collisions are discussed in detail. In particular, applications to ice at low temperatures are emphasized. A brief overview on simulations about planetary rings is given in Chapter 3. In order to show general effects of adhesive particle collision introduced in Chapter 2 on orbit dynamics, the stability of a two-body agglomerate and the mutual capture probability of two colliding grains is analyzed analytically and numerically. Result are discussed mainly in context of Saturn's rings. Implications with respect to pre-planetary aggregation are also addressed. In Chapter 4, growth processes are treated in terms of kinetic theory, while a general kinetic concept is proposed. The study concentrates on effects of adhesive collisions, and a coagulation equation is derived from basic principles. The otherwise phenomenological *Smoluchowski* equation (Smoluchowski, 1916) emerges as a limit case. A comparison of the former and the latter is given and its implications discussed. The conclusions in Chapter 5 summarize the results and give a brief outlook on future studies and possible applications.

Chapter 2

Granular Particle Collisions

Besides external forces, granular particles are subject to mutual collisions. In general, these interactions can be classified into long-range forces, such as gravity or electrostatic forces, and short-range interactions, such as contact forces. In case of relatively dilute systems, granular gases such as planetary rings, it is sufficient to consider binary collisions only. Any such collision can result in *(i)* agglomeration, *(ii)* restitution, or *(iii)* fragmentation (Spahn et al., 2004). Agglomeration becomes possible if attractive forces and dissipation dominate repulsive ones, while fragmentation, i.e. cratering and shattering impacts, occurs if relative velocities are large enough to erode attractive bonds. However, the main emphasis of this work is placed on aggregation and restitution.

In this chapter, we propose a dynamic contact model for adhesive, viscoelastic particles. The collision dynamics is described analytically in Sec. 2.2 and solved numerically in Sec. 2.3. A simplified, but reasonable, model is introduced in Sec. 2.3.1 and applied to icy grains in Sec. 2.4.1. A summary on model applicability and limitations is given at the end of this chapter.

2.1 Coefficients of Restitution

In this Section, we introduce the coefficients of restitution which are the most important parameters in describing granular gases. Besides a general theoretical interest, they are applied to agricultural studies of transport (Gan-Mor and Galili, 2000). There, the restitution coefficients of potatoes and tomatoes are investigated in order to allow for optimized fruit sorting mechanisms. Later on, these parameter will prove to be the decisive aspect to characterize a collisional outcome.

A collision between two solid, homogeneous spheres, $(m_1, \vec{r}_1)$ and $(m_2, \vec{r}_2)$ with velocity $\dot{\vec{r}}_1$ and $\dot{\vec{r}}_2$ and spin ω_1 and ω_2 can completely be described according to

$$\vec{r}_{\mathrm{c}} = \frac{m_1 \vec{r}_1 + m_2 \vec{r}_2}{m_1 + m_2} \quad ; \quad \vec{d} = \vec{r}_2 - \vec{r}_1 \;, \tag{2.1}$$

where $\vec{r}_{\mathrm{c}}$ and $\vec{d}$ denote the center of mass and relative distance between the grains, respectively. In terms of relative motion it is convenient to use the effective mass[1] $m_{\mathrm{eff}} = m_1 m_2/(m_1 + m_2)$. While the center of mass motion is continuous during collision $\ddot{\vec{r}}_{\mathrm{c}} = 0$,

---

[1] Effective values are generally obtained as $x_{\mathrm{eff}} = x_1 x_2/(x_1 + x_2)$.

the relative motion changes according to conservation of energy and momentum. At the very instant of the collision the dynamics can be treated in the collisional plane with $\vec{e}_d$ being its normal and $\vec{d} = d\vec{e}_d$. The impact is composed of its normal $\vec{N} \parallel \vec{e}_d$ and tangential component $\vec{T} \perp \vec{e}_d$. The relative velocity at impact is given by the relative surface velocity. It additionally accounts for each particles' rotation and thus reads

$$\begin{aligned} \vec{g} &= (\dot{\vec{r}}_2 - \vec{\omega}_2 \times R_2\vec{e}_d) - (\dot{\vec{r}}_1 + \vec{\omega}_1 \times R_1\vec{e}_d) \\ &= \dot{\vec{r}}_2 - \dot{\vec{r}}_1 - R_2\vec{\omega}_2 \times \vec{e}_d - R_1\vec{\omega}_1 \times \vec{e}_d \ , \end{aligned} \tag{2.2}$$

where R_i are the respective particle radii (Hertzsch et al., 1995; Brilliantov et al., 1996). The related normal and tangential impact velocity read $\vec{g}_N = (\dot{\vec{r}}_2 - \dot{\vec{r}}_1) \cdot \vec{e}_d = \dot{\vec{d}}$ and $\vec{g}_T = (\dot{\vec{r}}_2 - \dot{\vec{r}}_1 - R_2\vec{\omega}_2 - R_1\vec{\omega}_1) \times \vec{e}_d$. In case of perfectly elastic collisions no energy is dissipated and the process itself is reversible in time. In case of inelastic collisions and thus any real material application, energy is no longer conserved and expressed as a broken symmetry in time as illustrated in Fig. 2.1. The amount of dissipated, relative kinetic energy is characterized by the *coefficients of restitution*[2], where ε_N refers to normal and ε_T to tangential motion. They denote the ratio of relative impact speed before and after collision as

$$g'_\mathrm{N} = -\varepsilon_\mathrm{N} g_\mathrm{N} \ ; \ \varepsilon_\mathrm{N} \in [\ \ 0,1] \tag{2.3}$$

$$g'_\mathrm{T} = \varepsilon_\mathrm{T} g_\mathrm{T} \ ; \ \varepsilon_\mathrm{T} \in [-1,1] \tag{2.4}$$

where primed variables denote values after collision. The actual amount of dissipated energy in case of restitution can be written as (Brilliantov et al., 1996)

$$\Delta E = (\Delta E_\mathrm{N}) + (\Delta E_\mathrm{T}) = \frac{m_\mathrm{eff}}{2} g_\mathrm{N}^2 (\varepsilon_\mathrm{N}^2 - 1) + \frac{m_\mathrm{eff}}{2} \kappa_{12} g_\mathrm{T}^2 (\varepsilon_\mathrm{T}^2 - 1), \tag{2.5}$$

where κ_{12} accounts for the particle's moment of inertia. In case of uniform spheres $\kappa_{12} = 2/7$. Elastic and inelastic collisions can be distinguished as $\Delta E = 0$ for elastic and $\Delta E < 0$ for inelastic collisions. The limit case of $\Delta E = -E_\mathrm{kin} = -m_\mathrm{eff}\vec{g}^{\,2}/2$ denotes aggregation, where both particles stick together and move at the unchanged center of mass speed $\dot{\vec{r}}_\mathrm{c}$ since $\ddot{\vec{r}}_\mathrm{c} = 0$. The normal coefficient of restitution ε_N ranges between zero and unity i.e. between purely dissipative and perfectly elastic impacts. The tangential restitution coefficient ε_T, on the other hand, denotes a sliding motion for $\varepsilon_\mathrm{T} \geq 0$ and a spin-reversal for $\varepsilon_\mathrm{T} < 0$. In case of ideally smooth surfaces $\varepsilon_\mathrm{T} = 1$ and furthermore independent of the grain material.

Thus, as long as the duration of a collision is negligibly small its outcome is fully determined by the coefficients of restitution. Given a particular material, simulations or experiments denote ways to obtain these parameters. *Pade* approximation and the method of inverse collision are usually applied to obtain analytical expressions for ε_N (Ramírez et al., 1999). However, dissipation cannot satisfyingly accounted for in an analytic manner.

We will provide a detailed overlook on contact dynamics and propose a collision model denoting a significant extension to previously existing models.

---

[2] A third coefficient, the coefficient of binormal restitution ε_B, denotes the second tangential component perpendicular to the previous two. It, however, is usually disregarded in theoretical and experimental studies. The change of angular momentum for the binormal component is related to the radius of the contact area, whereas for the tangential one it is related to the radius of the spheres. Thus, the change of angular momentum is in case of binormal motion always smaller than in case of tangential motion.

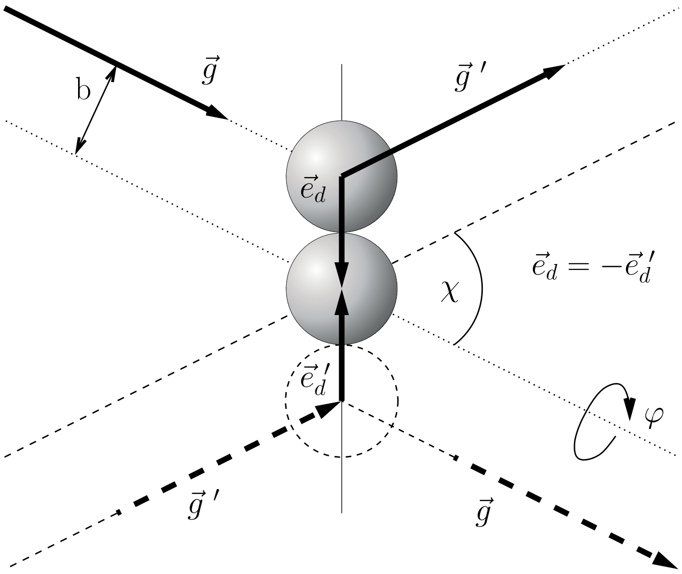

(a) elastic collision

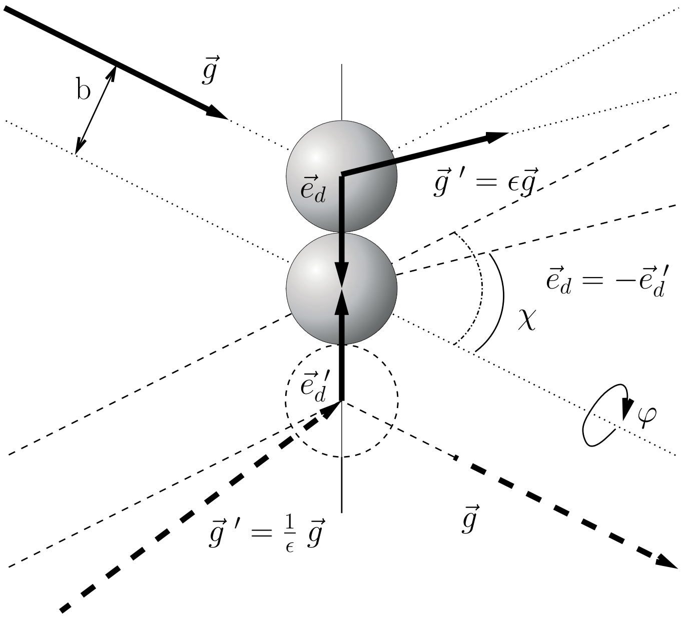

(b) inelastic collision

Figure 2.1: Sketch of the geometrical relations of velocities involved during collision. The collisions are rotationally symmetric with respect to φ and have an impact parameter b. Incoming particles will be scattered and ejected at an angle χ. Solid vectors denote the forward $(+t)$ and dashed ones the time reversed collision ($t \to -t$). For inelastic collisions the symmetry with respect to time is broken. The ejection angle χ is thus smaller than in the elastic case. Velocities are reduced by a factor of ε or in case of the time reversed collision have to be larger by exactly this factor.

2.2 Contact Model

Although particles in space can have all kinds of shapes, compositions, and surface structures, a simple model should suffice at this point. Grains are assumed to be solid, homogeneous spheres of mass m and radius R with perfectly smooth surfaces, i.e. $\varepsilon_\mathrm{T} = 1$, for simplicity. At this point, we concentrate on the normal component of relative motion $\vec{N}$.

If two particles collide they will temporarily experience a compression which can be defined as

$$\xi = R_1 + R_2 - |\vec{r}_2 - \vec{r}_1| \tag{2.6}$$

where $\xi \geq 0$ denotes the effective normal deformation if the particles are in contact and $\xi < 0$ the actual distance between the particle's surfaces, otherwise.

Material deformations have been studied extensively and, depending on the materials considered, may feature elastic, adhesive, viscoelastic, plastic, or even a mix of these types of behavior. Here, we shall revisit the basic theoretical considerations (see e.g. Landau and Lifshitz, 1959; Tschoegl, 1989) in order to compile a new model of contact dynamics.

A given point within a solid body is attributed with a position vector $\vec{x}$. Any deformation can be expressed as $\mathrm{d}x'_\mathrm{i} = \mathrm{d}x_\mathrm{i} + u_\mathrm{i}(x_\mathrm{i} + \mathrm{d}x_\mathrm{i}) - u_\mathrm{i}(x_\mathrm{i}) = \mathrm{d}x_\mathrm{i} + \mathrm{d}u_\mathrm{i}$ where $\vec{u}$ denotes the deformation and i indicates the according Cartesian coordinate. In case of small deformations $\mathrm{d}u_\mathrm{i} = u_\mathrm{i} + u_\mathrm{ik}\mathrm{d}x_\mathrm{k}$. Within the limit of linear elastic theory, higher order derivatives are neglected. The *strain* tensor or differential deformation[3] is given by

$$u_\mathrm{ik} = \frac{\partial u_\mathrm{i}}{\partial x_\mathrm{k}} = \frac{1}{2}\left(\frac{\partial u_\mathrm{i}}{\partial x_\mathrm{k}} + \frac{\partial u_\mathrm{k}}{\partial x_\mathrm{i}}\right) = \left(u_\mathrm{ik} - \frac{1}{3}\delta_\mathrm{ik}u_\mathrm{ll}\right) + \frac{1}{3}\delta_\mathrm{ik}u_\mathrm{ll}\ . \tag{2.7}$$

Any deformation may be split into a shearing deformation without volume changes (the expression in brackets has a vanishing trace $u_\mathrm{ii} = 0$) and pressure-driven deformation, that do invoke volume but no shape changes ($u_\mathrm{ik} = const.\delta_\mathrm{ik}$). u_ll denotes the relative volume change $\mathrm{d}V'/\mathrm{d}V$ or cubic strain with $\mathrm{d}V' = \mathrm{d}V(1 + u_\mathrm{ll})$, and δ_ik is *Kronecker*'s delta. In case of ideal elastic, infinitesimal deformations, the stress tensor $\hat{\sigma}$ does only depend on strain $\sigma^\mathrm{el}_\mathrm{ik} = C_\mathrm{ikjl}\, u_\mathrm{jl}$ where C_ikjl accounts for material parameters. Thus an ideal elastic body shows no stress without a deformation and vice versa. Material's elasticity is given by bulk and shear modulus. An isotropic medium can be characterized by two *Lamé* constants $(\lambda_\mathrm{I}, \lambda_\mathrm{II})$. In this case C_ikjl takes a simplified form[4] and the generalized *Hook*'s law reads

$$\sigma^\mathrm{el}_\mathrm{ik} = \lambda_\mathrm{I}\delta_\mathrm{ik}u_\mathrm{ll} + 2\lambda_\mathrm{II}u_\mathrm{ik}\ . \tag{2.8}$$

The material immediately responds to applied stresses and there is no need to indicate a time dependence or neither stress nor strain. Since there exists no perfectly elastic material, material dependent dissipation is inevitable.

Viscosity is, besides plasticity, one way to account for dissipation. It is generally velocity dependent and denotes a rather intuitive way to describe inner friction (cf. a damped

---

[3] While the subscript i denotes Cartesian coordinates, *Einstein*'s summation rule applies hereafter. Note, the strain tensor is symmetric $u_\mathrm{ik} = u_\mathrm{ki}$.

[4] While the stress-strain relation here is expressed in terms of *Lamé* constants for simplicity, it may also be written using e.g. *Young* modulus Y and *Poisson* ratio ν, or elasticity parameters E_I and E_II. However, all of these definitions yield the same and may be transformed into each other (cf. Eq. (2.18)).

harmonic oscillator). Viscosity arises as a memory effect. Materials need a characteristic time to respond to external stresses. Purely viscous materials react immediately whereas all energy will be dissipated as heat. Stress then has to be considered as a time dependent function since it does not depend on strain alone but on strain history as well. The viscoelastic behavior can be described in analogy to Eq. (2.8) where a *correspondence principle* is applied to $\sigma^{\mathrm{vis}}_{\mathrm{ik}} \sim \dot{u}_{\mathrm{ik}}$. This *correspondence principle* states that "if an elastic solution is known, substituting the *Laplace* transforms of stress and strain and the corresponding response functions for the elastic constants, immediately furnishes the viscoelastic solution" (Tschoegl, 1989). Thus, the stress strain-rate relation reads

$$\sigma^{\mathrm{vis}}_{\mathrm{ik}}(t) \quad = \quad \int_0^t \lambda_{\mathrm{I}}\psi(t-p)\delta_{\mathrm{ik}}\dot{u}_{\mathrm{ll}}(p)\mathrm{d}p + 2\int_0^t \lambda_{\mathrm{II}}\psi(t-p)\dot{u}_{\mathrm{ik}}(p)\mathrm{d}p \tag{2.9}$$

where $\psi(t)$ characterizes the stress relaxation function. This approach is also known as the *Boltzmann* superposition principle (Tschoegl, 1989; Greenwood and Johnson, 1981). The stress strain-rate relation may therefore be written as

$$\sigma^{\mathrm{vis}}_{\mathrm{ik}}(t) \quad = \quad \eta_{\mathrm{I}}\delta_{\mathrm{ik}}\dot{u}_{\mathrm{ll}}(t) + 2\eta_{\mathrm{II}}\dot{u}_{\mathrm{ik}}(t)\ . \tag{2.10}$$

The total stress for a viscoelastic material can be written as $\sigma_{\mathrm{ik}} = \sigma^{\mathrm{el}}_{\mathrm{ik}} + \sigma^{\mathrm{vis}}_{\mathrm{ik}}$ and represented as an electric circuit where dashpots and springs are connected either in series, in parallel, or in combination of both. The dashpot is then dissipating energy with a distinct delay while the spring is merely storing energy (see e.g. Tschoegl, 1989; Hudson, 1980).

Internal forces f_{i} can be expressed as $f_{\mathrm{i}} = \partial\sigma_{\mathrm{ik}}/\partial x_{\mathrm{k}}$ and the equation of motion for a continuous medium reads

$$\rho\frac{\partial^2 u_{\mathrm{i}}}{\partial t^2} \quad = \quad \frac{\partial\sigma_{\mathrm{ik}}}{\partial x_k} + \rho F_i\ , \tag{2.11}$$

where F_{i} denote external forces as e.g. gravity. Assuming no apparent external forces $F_{\mathrm{i}} = 0$ and substituting Eqs. (2.8) and (2.10) in Eq. (2.11) yields

$$\rho\frac{\partial^2 u_{\mathrm{i}}}{\partial t^2} \quad = \quad \lambda_{\mathrm{II}}\frac{\partial^2 u_{\mathrm{i}}}{\partial x_{\mathrm{k}}^2} + (\lambda_{\mathrm{I}}+\lambda_{\mathrm{II}})\frac{\partial^2 u_{\mathrm{k}}}{\partial x_{\mathrm{i}}\partial x_{\mathrm{k}}} + \eta_{\mathrm{II}}\frac{\partial^2 \dot{u}_{\mathrm{i}}}{\partial x_{\mathrm{k}}^2} + (\eta_{\mathrm{I}}+\eta_{\mathrm{II}})\frac{\partial^2 \dot{u}_{\mathrm{k}}}{\partial x_{\mathrm{i}}\partial x_{\mathrm{k}}}\ . \tag{2.12}$$

Eqs. (2.11) reads in a coordinate-free form $\rho\ddot{\vec{u}} = \nabla\cdot\hat{\sigma} + \rho\vec{F}$ and thus (2.12) may be rewritten using the vector identity $\Delta\vec{x} = \nabla(\nabla\cdot\vec{x}) - \nabla\times(\nabla\times\vec{x})$ and $\nabla\cdot\hat{\sigma} = \nabla\cdot(\hat{\sigma}^{\mathrm{el}} + \hat{\sigma}^{\mathrm{vis}})$ as

$$\rho\ddot{\vec{u}} \quad = \quad \lambda_{\mathrm{II}}\Delta\vec{u} + (\lambda_{\mathrm{I}}+\lambda_{\mathrm{II}})\nabla(\nabla\cdot\vec{u}) + \eta_{\mathrm{II}}\Delta\dot{\vec{u}} + (\eta_{\mathrm{I}}+\eta_{\mathrm{II}})\nabla(\nabla\cdot\dot{\vec{u}})\ . \tag{2.13}$$

Let us introduce material dependent longitudinal c_{l} and transversal c_{t} speed of sound as ${c_{\mathrm{l}}}^2 = (\lambda_{\mathrm{I}} + 2\lambda_{\mathrm{II}})/\rho$ and ${c_{\mathrm{t}}}^2 = \lambda_{\mathrm{I}}/\rho$. Corresponding viscous parameters read ${p_{\mathrm{l}}}^2 = (\eta_{\mathrm{I}} + 2\eta_{\mathrm{II}})/\rho$ and ${p_{\mathrm{t}}}^2 = \eta_{\mathrm{I}}/\rho$. Equation (2.13) can be rewritten as

$$\ddot{\vec{u}} \quad = \quad c_{\mathrm{l}}^2\nabla(\nabla\cdot\vec{u}) - c_{\mathrm{t}}^2\nabla\times(\nabla\times\vec{u}) + p_{\mathrm{l}}^2\nabla(\nabla\cdot\dot{\vec{u}}) - p_{\mathrm{t}}^2\nabla\times(\nabla\times\dot{\vec{u}})\ . \tag{2.14}$$

Furthermore, scaling Eq. (2.14) with a characteristic time T and length X results in

$$\frac{V^2}{c_{\mathrm{l}}^2}\ddot{\vec{u}} \quad = \quad \nabla(\nabla\cdot\vec{u}) - \frac{c_{\mathrm{t}}^2}{c_{\mathrm{l}}^2}\nabla\times(\nabla\times\vec{u}) + \frac{1}{T}\left(\frac{p_{\mathrm{l}}^2}{c_{\mathrm{l}}^2}\nabla(\nabla\cdot\dot{\vec{u}}) - \frac{p_{\mathrm{t}}^2}{c_{\mathrm{l}}^2}\nabla\times(\nabla\times\dot{\vec{u}})\right)\ , \tag{2.15}$$

where V denotes the characteristic speed $V = X/T$. If the characteristic deformation speed is much smaller than the speed of sound $V \ll c_\mathrm{l}$, no solid body (acoustic) waves will be excited. In other words, the collision time τ is sufficiently larger than the largest period of any vibration of either bodies. If additionally the dissipation in the bulk is low, i.e. ${p_\mathrm{l}}^2/X$ and ${p_\mathrm{t}}^2/X$ are of the order of unity, Eq. (2.14) reduces to the static problem $\nabla \cdot \hat{\sigma} = 0$ and a collision can be described as passing through consecutive equilibrium states. In case of rocky or icy materials the speed of sound is about $\mathrm{km\,s^{-1}}$ and thus low-velocity collisions as e.g. the random-walk speed in unperturbed planetary rings of $\mathrm{mm\,s^{-1}}$ to $\mathrm{cm\,s^{-1}}$ result in *quasistatic* or *quasiadiabatic* deformations.

In the following we will consider the static solutions of spheres in contact and will concentrate on normal deformations. This results in normal forces only, where $\vec{F} \parallel \vec{e}_d$. For simplicity, only their absolute values are given ($|\vec{F}| = F$). Since particles are thought to have smooth surfaces no friction will be present.

2.2.1 Elastic Contact of Two Spheres (*Hertz* theory)

The static problem of two perfectly elastic spheres in contact has been initially addressed by Hertz (1882) and has ever since entered textbooks (see e.g. Landau and Lifshitz, 1959). We will sketch this theory here in a simplified form. If both particles are in touch they will form a circular contact area of radius a. The problem itself goes back to the elastic contact of two flat surfaces. However, the geometry of the curved particle surface has to be taken into account. Thus, the effective deformation introduced in Eq. (2.6) can also be written as

$$\xi \;=\; (u_\mathrm{z})_1 + (u_\mathrm{z})_2 - A(x^2+y^2)\,, \tag{2.16}$$

where $(u_\mathrm{z})_n$ denotes the normal compression of each sphere and $2A = (1/R_1 + 1/R_2) = R_\mathrm{eff}^{-1}$ their curvature. Within the contact area surfaces are regarded as plane. Thus the textbook solution of two flat surfaces in contact can be applied and the normal stress tensor load then reads

$$\sigma^\mathrm{el}_\mathrm{zz} \;=\; (2\lambda_\mathrm{II}+\lambda_\mathrm{I})u_\mathrm{zz} + \lambda_\mathrm{I}\left(u_\mathrm{xx}+u_\mathrm{yy}\right) \;=\; \frac{3F_\mathrm{el}}{2\pi a^2}\sqrt{1-\frac{1}{a^2}(x^2+y^2)}\,. \tag{2.17}$$

F_el denotes the applied force which is directly proportional to the pressure distribution over the contact area. *Lamé* 's constants may be expressed in terms of more directly accessible material constants such as *Young* modulus Y and *Poisson* ratio ν as

$$\lambda_\mathrm{I} \;=\; \frac{Y\nu}{(1+\nu)(1-2\nu)} \quad,\quad \lambda_\mathrm{II} \;=\; \frac{2Y}{1+\nu}\,. \tag{2.18}$$

Solving the static problem for boundary conditions of a flat surface yields

$$(u_z)_n \;=\; \frac{1-\nu_n^2}{\pi Y_n}\int\!\!\int \frac{\sigma^\mathrm{el}_\mathrm{zz}(x',y')}{\sqrt{(x-x')^2+(y-y')^2}}\,\mathrm{d}x'\mathrm{d}y'\,. \tag{2.19}$$

Introducing the effective material parameter E_eff with $E_n \;=\; Y_n/(1-\nu_n^2)$ and substituting Eq. (2.19) into (2.16) results in

$$\frac{1}{\pi E_\mathrm{eff}}\int\!\!\int \frac{\sigma^\mathrm{el}_\mathrm{zz}(x',y')}{\sqrt{(x-x')^2+(y-y')^2}}\,\mathrm{d}x'\mathrm{d}y' \;=\; \xi + A(x^2+y^2)\,. \tag{2.20}$$

With Eq. (2.17) and by comparing the coefficients in Eq. (2.20) follows

$$\xi = \frac{3F_{\mathrm{el}}}{4\pi E_{\mathrm{eff}}} \int_0^\infty \frac{\mathrm{d}w}{(a^2+w)\sqrt{w}} = \frac{3F_{\mathrm{el}}}{4E_{\mathrm{eff}}} \frac{1}{a} \tag{2.21}$$

$$A = \frac{3F_{\mathrm{el}}}{4\pi E_{\mathrm{eff}}} \int_0^\infty \frac{\mathrm{d}w}{(a^2+w)^2\sqrt{w}} = \frac{3F_{\mathrm{el}}}{4E_{\mathrm{eff}}} \frac{1}{2a^3} \,. \tag{2.22}$$

Since $A = 2/R_{\mathrm{eff}}$, Eq. (2.21) and (2.22) fix the relation between contact radius a and compression ξ

$$\xi = \frac{a^2}{R_{\mathrm{eff}}} \,, \tag{2.23}$$

which reinserted into Eq. (2.21) yields

$$F_{\mathrm{el}}(\xi) = \frac{4}{3} E_{\mathrm{eff}} \sqrt{R_{\mathrm{eff}}}\, \xi^{3/2} \,. \tag{2.24}$$

This relation may be rewritten as

$$F_{\mathrm{el}}(a) = \frac{4}{3} \frac{E_{\mathrm{eff}}}{R_{\mathrm{eff}}} a^3 \quad \text{and} \quad \xi(a) = \frac{a^2}{R_{\mathrm{eff}}} \,. \tag{2.25}$$

Equation (2.25) is valid for the normal contact of spherical particles with smooth surfaces. The proportionality of ξ to a^2 will henceforth be referred to as *Hertzian* relation. If non-spherical particles were under consideration, the contact area would be elliptical instead of circular. The corresponding problem can nevertheless be mapped onto the circular case while force-deformation relations remain the same (Landau and Lifshitz, 1959; Hertzsch et al., 1995).

2.2.2 Extension to an Adhesive Elastic Contact

While elasticity gives rise to repulsive forces alone, actual surface structures may lead to attractive short-range interactions. In the context of smooth particle surfaces, the effects of adhesion on a static elastic contact based on *Hertz*'s theory (see Sec. 2.2.1) have been studied by Johnson et al. (1971). They introduced a surface energy $U_{\mathrm{S}} = -\pi\gamma_{\mathrm{S}} a^2$ where γ_{S} denotes the surface energy per unit area of both spheres as $\gamma_{\mathrm{S}} = \gamma_1 + \gamma_2 - \gamma_{12}$. Compared to a pure elastic contact, an adhesive one increases the apparent load compared to a pure elastic contact. This marks the essence of the JKR theory (Johnson, Kendall, and Roberts) which can be expressed as a superposition of the *Hertzian* stress distribution and a negative flat punch $\sigma_{zz}^{\mathrm{static}} = \sigma_{zz}^{\mathrm{el}} + \sigma_{zz}^{\mathrm{ad}}$ (Muller et al., 1980) where

$$\sigma_{zz}^{\mathrm{ad}} = -\frac{3F_{\mathrm{ad}}}{2\pi a^2} \left(1 - \frac{1}{a^2}(x^2+y^2)\right)^{-1/2} \,. \tag{2.26}$$

The resulting equation for the apparent outer force compared to the actually applied stress reads (Johnson et al., 1971, Eq. (19))

$$F_{\mathrm{applied}} = F_{\mathrm{actual}} + 3\pi\gamma_{\mathrm{S}} R_{\mathrm{eff}} + \sqrt{6\pi\gamma_{\mathrm{S}} R_{\mathrm{eff}} F_{\mathrm{actual}} + (3\pi\gamma_{\mathrm{S}} R_{\mathrm{eff}})^2} \,. \tag{2.27}$$

Applying the *Hertzian* elastic force $F_{\mathrm{applied}} = F_{\mathrm{el}}(a)$ as in Eq. (2.25) and solving for F_{actual}, Eq. (2.27) yields

$$F_{\mathrm{actual}}(a) = \frac{4}{3} \frac{E_{\mathrm{eff}}}{R_{\mathrm{eff}}} a^3 - \sqrt{8\pi E_{\mathrm{eff}} \gamma_{\mathrm{S}}}\, a^{3/2} \,. \tag{2.28}$$

In this static approach, an equilibrium deformation ξ_{ad} with the corresponding contact radius

$$a_{\mathrm{ad}}^3 = \frac{9\pi}{2}\frac{\gamma_{\mathrm{S}} R_{\mathrm{eff}}^2}{E_{\mathrm{eff}}} \tag{2.29}$$

will form for $F_{\mathrm{actual}}(a_{\mathrm{ad}}) = 0$ and a resulting adhesive bond

$$F_{\mathrm{bond}} = \frac{3}{2}\pi\gamma_{\mathrm{S}} R_{\mathrm{eff}} \tag{2.30}$$

is independent of elastic material properties. F_{bond} denotes the actual force that has to be applied in order to separate the two surfaces and thus destroy an adhesive bond. In this approach specific surface structures can only be accounted for in terms of γ_{S}. Larger contact areas result in a higher surface energy whereas the adhesive bond strength is linearly dependent on the effective grain radius. The corresponding ξ-a relation can thus be derived and the total force-deformation relation yields

$$F_{\mathrm{static}}(a) = \frac{4}{3}\frac{E_{\mathrm{eff}}}{R_{\mathrm{eff}}} a^3 - \sqrt{8\pi E_{\mathrm{eff}}\gamma_{\mathrm{S}}}\, a^{3/2} = F_{\mathrm{el}}(a) + F_{\mathrm{ad}}(a) \tag{2.31}$$

$$\xi(a) = \frac{a^2}{R_{\mathrm{eff}}} - \sqrt{\frac{2\pi\gamma_{\mathrm{S}}}{E_{\mathrm{eff}}}}\, a^{1/2}\,. \tag{2.32}$$

Equation (2.32) reduces to the *Hertzian* relation (Eq. (2.25)) in case of a pure elastic contact $\gamma_{\mathrm{S}} = 0$. In case of non-spherical particles, relations can be mapped onto the spherical case (Johnson and Greenwood, 2005) as before.

2.2.3 Viscoelastic Effects

As discussed above imperfect materials introduce an inner friction and thus energy dissipation to deformation processes. Nevertheless, within the limits of the *quasistatic approximation*, deformations are not explicitely time dependent and still satisfy the equilibrium solution. According to Secs. 2.2.1 and 2.2.2, a quasi-adiabatic deformation $u_{\mathrm{i}}(x_{\mathrm{i}},t)$ is parametrically dependent on the compression ξ. In particular, $u_{\mathrm{i}}(x_{\mathrm{i}},t) \approx u_{\mathrm{i}}(x_{\mathrm{i}},\xi) = \tilde{u}_{\mathrm{i}}(x_{\mathrm{i}},a)$. The strain rate may then be written as

$$\dot{u}_{\mathrm{ik}}(x_{\mathrm{i}},t) \approx \dot{\xi}\frac{\partial}{\partial\xi} u_{\mathrm{ik}}(x_{\mathrm{i}},\xi) = \dot{a}\frac{\partial}{\partial a}\tilde{u}_{\mathrm{ik}}(x_{\mathrm{i}},a)\,, \tag{2.33}$$

and Eq. (2.10) becomes

$$\sigma_{\mathrm{ik}}^{\mathrm{vis}} = \dot{\xi}\frac{\partial}{\partial\xi}(\eta_{\mathrm{I}}\delta_{\mathrm{ik}}u_{\mathrm{ll}} + 2\eta_{\mathrm{II}}u_{\mathrm{ik}}) \sim \dot{\xi}\frac{\partial}{\partial\xi}\sigma_{\mathrm{ik}}^{\mathrm{static}}[\lambda_{\mathrm{n}} \leftrightarrow \eta_{\mathrm{n}}]\,, \tag{2.34}$$

where the elastic constants λ_{n} have been exchanged with according viscoelastic ones η_{n} (Hertzsch et al., 1995; Brilliantov et al., 1996). Even in the presence of adhesion stresses and deformations in a viscoelastic solid may be inferred from the corresponding elastic problem by applying the *Boltzmann* superposition principle. Especially for low-velocity deformations it is sufficient to exchange the elastic moduli with their corresponding relaxed ones (Greenwood and Johnson, 1981) (see also Sec. 2.2). Concentrating on the collisional contact problem where

$$\sigma_{\mathrm{zz}}^{\mathrm{el}}(x,y,0) = \lambda_{\mathrm{I}}(u_{\mathrm{xx}} + u_{\mathrm{yy}} + u_{\mathrm{zz}}) + 2\lambda_{\mathrm{II}}u_{\mathrm{zz}} = \frac{3F_{\mathrm{el}}}{2\pi a^2}\sqrt{1 - \frac{1}{a^2}(x^2+y^2)} \tag{2.35}$$

$$\sigma_{\mathrm{zz}}^{\mathrm{ad}}(x,y,0) = \lambda_{\mathrm{I}}(u_{\mathrm{xx}} + u_{\mathrm{yy}} + u_{\mathrm{zz}}) + 2\lambda_{\mathrm{II}}u_{\mathrm{zz}} = \frac{3F_{\mathrm{ad}}}{2\pi a^2}\left[1 - \frac{1}{a^2}(x^2+y^2)\right]^{-1/2} \tag{2.36}$$

we transform the coordinates according ($x' = \alpha x$; $y' = \alpha y$; $z' = z$) and thus map $\sigma_{\mathrm{ik}}^{\mathrm{static}}[\lambda_{\mathrm{n}} \leftrightarrow \eta_{\mathrm{n}}]$ onto $\sigma_{\mathrm{ik}}^{\mathrm{static}}$ (Eq. (2.8)). In order to exchange the material constants, β is temporarily defined as

$$\beta = \frac{2\eta_{\mathrm{II}} + \eta_{\mathrm{I}}}{2\lambda_{\mathrm{II}} + \lambda_{\mathrm{I}}} \tag{2.37}$$

and from Eq. (2.34) follows

$$\begin{aligned}
\sigma_{\mathrm{zz}}^{\mathrm{vis}}(x,y,0) &= \dot{\xi}\frac{\partial}{\partial\xi}\left[(2\eta_{\mathrm{II}}+\eta_{\mathrm{I}})u_{\mathrm{zz'}} + \eta_{\mathrm{I}}\alpha(u_{\mathrm{xx'}}+u_{\mathrm{yy'}})\right] &(2.38)\\
&= \dot{\xi}\frac{\partial}{\partial\xi}\beta\left[(2\lambda_{\mathrm{II}}+\lambda_{\mathrm{I}})u_{\mathrm{zz'}} + \frac{2\lambda_{\mathrm{II}}+\lambda_{\mathrm{I}}}{2\eta_{\mathrm{II}}+\eta_{\mathrm{I}}}\,\eta_{\mathrm{I}}\alpha(u_{\mathrm{xx'}}+u_{\mathrm{yy'}})\right]\,. &(2.39)
\end{aligned}$$

Let then α be

$$\alpha = \frac{\lambda_{\mathrm{I}}}{\eta_{\mathrm{I}}}\,\frac{2\eta_{\mathrm{II}}+\eta_{\mathrm{I}}}{2\lambda_{\mathrm{II}}+\lambda_{\mathrm{I}}}\,.x \tag{2.40}$$

We further obtain

$$\begin{aligned}
\sigma_{\mathrm{zz}}^{\mathrm{vis}}(x,y,0) &= \dot{\xi}\frac{\partial}{\partial\xi}\beta\left[(2\lambda_{\mathrm{II}}+\lambda_{\mathrm{I}})u_{\mathrm{zz'}} + \lambda_{\mathrm{I}}(u_{\mathrm{xx'}}+u_{\mathrm{yy'}})\right] &(2.41)\\
&= \dot{\xi}\frac{\partial}{\partial\xi}\beta\left[\lambda_{\mathrm{I}}(u_{\mathrm{xx'}}+u_{\mathrm{yy'}}+u_{\mathrm{zz'}}) + 2\lambda_{\mathrm{II}}u_{\mathrm{zz'}}\right] &(2.42)\\
&= \dot{\xi}\frac{\partial}{\partial\xi}\beta\frac{3F_{\mathrm{el}}}{2\pi a'^2}\sqrt{1-\frac{1}{a'^2}(x'^2+y'^2)} &(2.43)\\
&= \dot{\xi}\frac{\partial}{\partial\xi}\frac{\beta}{\alpha^2}\frac{3F_{\mathrm{el}}}{2\pi a^2}\sqrt{1-\frac{1}{a^2}(x^2+y^2)}\,. &(2.44)
\end{aligned}$$

In analogy to elastic stresses, Eq. (2.44) has to be integrated with respect to the contact area in order to obtain a force relation. The dissipative force is given by $F_{\mathrm{vis}}(\xi,\dot{\xi}) \sim \dot{\xi}\ \partial/\partial\xi\ [F_{\mathrm{static}}(\xi,\dot{\xi})]$ (cf. Eq. (2.34)) and can be expressed as

$$F_{\mathrm{vis}}(\xi,\dot{\xi}) = \dot{\xi}\frac{\partial}{\partial\xi}\left(A_{\mathrm{vis}}F_{\mathrm{el}}(\xi) + B_{\mathrm{vis}}F_{\mathrm{ad}}(\xi)\right)\,. \tag{2.45}$$

The proportionality factor[5] (see Eq. (2.44)) reads

$$A_{\mathrm{vis}} = B_{\mathrm{vis}} = \frac{\beta}{\alpha^2} = \left(\frac{\eta_{\mathrm{I}}}{\lambda_{\mathrm{I}}}\right)^2 \frac{2\lambda_{\mathrm{II}}+\lambda_{\mathrm{I}}}{2\eta_{\mathrm{II}}+\eta_{\mathrm{I}}} = \frac{\eta_{\mathrm{II}}^2}{\eta_{\mathrm{I}}+2\eta_{\mathrm{II}}}\,\frac{(1-\nu^2)(1-2\nu)}{\nu Y}\,. \tag{2.46}$$

in accordance with (Hertzsch et al., 1995). A_{vis} and B_{vis} describe the viscous relaxation time ($[A_{\mathrm{vis}}] = [B_{\mathrm{vis}}] = \mathrm{s}$) and are material specific values. They remain widely unknown since there are no appropriate ways to measure them. The dissipative force corresponding to Eq.(2.31) reads

$$F_{\mathrm{vis}}(a,\dot{a}) = \dot{a}\left(4A_{\mathrm{vis}}\frac{E_{\mathrm{eff}}}{R_{\mathrm{eff}}}a^2 - \frac{3}{2}B_{\mathrm{vis}}\sqrt{8\pi E_{\mathrm{eff}}R_{\mathrm{eff}}}\,a^{1/2}\right) \sim \dot{a}\frac{\partial}{\partial a}F_{\mathrm{static}}(a)\,. \tag{2.47}$$

---

[5] Although A_{vis} and B_{vis} are the same parameter they will be distinguished here for an easier handling in later discussions (see Sec. 2.3.1)

As for the superposition principle the total stress consists of a static and a viscous part $\sigma_{\mathrm{ik}} = \sigma_{\mathrm{ik}}^{\mathrm{static}} + \sigma_{\mathrm{ik}}^{\mathrm{vis}}$ and thus the total force reads

$$F_{\mathrm{total}}(a) \;=\; F_{\mathrm{static}}(a) + F_{\mathrm{vis}}(a) \tag{2.48}$$

where $F_{\mathrm{static}}(a)$ and $F_{\mathrm{vis}}(a)$ are defined according to Eqs.(2.31) and (2.47). In contrast to Hertzsch et al. (1995) and Brilliantov et al. (1996), the presented model denotes an extended collision model. We are now able to allow for adhesive interactions in a non-static contact.

2.3 Equations of Motion

The contact dynamics is based on the time evolution of the compression $\xi(t)$. Within the limits of the *quasistatic approximation* it is described by an ordinary differential equation based upon field equation (2.11)

$$\begin{aligned} m_{\mathrm{eff}}\,\ddot{\xi}(t) + F_{\mathrm{static}}(\xi(t)) + F_{\mathrm{vis}}(\xi(t)) \;&=\; 0 \\ \dot{\xi}(0) \;=\; v_{\mathrm{imp}}\;;\; \xi(0) \;&=\; \xi_{\mathrm{init}}\,. \end{aligned} \tag{2.49}$$

Since contact forces (see Eqs. (2.31), (2.32), and (2.47)) cannot easily be expressed as functions of ξ, the contact dynamics can likewise be solved in terms of contact radius a. The equation of motion then reads

$$\begin{aligned} m_{\mathrm{eff}}\,\ddot{a}(t) + m_{\mathrm{eff}}\,\frac{\xi''(t)}{\xi'(t)}\dot{a}^2(t) + \frac{F_{\mathrm{static}}(a(t))}{\xi'(t)} + \frac{F_{\mathrm{vis}}(a(t))}{\xi'(t)} \;&=\; 0 \\ \dot{a}(0) \;=\; \left(\xi'_{t=0}\right)^{-1} v_{\mathrm{imp}}\;;\; a(0) \;&=\; a_{\mathrm{init}}\,, \end{aligned} \tag{2.50}$$

where $(.)'$ denotes the partial derivative with respect to a. They are obtained by differentiating Eq. (2.32) accordingly and read

$$\frac{\partial\xi}{\partial a} \;=\; \frac{2a}{R_{\mathrm{eff}}} - \frac{1}{2}\sqrt{\frac{2\pi\gamma_S}{E_{\mathrm{eff}}}}\,a^{-1/2} \tag{2.51}$$

$$\frac{\partial^2\xi}{\partial a^2} \;=\; \frac{2}{R_{\mathrm{eff}}} + \frac{1}{4}\sqrt{\frac{2\pi\gamma_S}{E_{\mathrm{eff}}}}\,a^{-3/2}\,. \tag{2.52}$$

The initial point for contact forces to set in is at the very first touching of both particles at $\xi_{\mathrm{init}} = \xi(0) = 0$ (see Eq. (2.6)). According to Eq. (2.32), the corresponding initial contact area a_0, however, is larger then zero

$$a_0^3 \;=\; 2\pi\,\frac{\gamma_S R_{\mathrm{eff}}^2}{E_{\mathrm{eff}}}\,, \tag{2.53}$$

which is the result of an instantaneous reorganization of the surfaces upon contact. Thus, particles will share a common contact area πa_{init}^2 where $a_{\mathrm{init}} = a_0$. This has also been referred to as “jumping in” and “out of” contact. It has been noticed in experiments (Muller et al., 1980; Greenwood, 1997) and is accompanied by the formation of a “bottle-neck” in between the particle surfaces which in theory is specific to the JKR approach[6]. This kind of initial “snapping” denotes an irreversible energy loss of E_{snap}.

---

[6] However, there are still discussions about what exactly a_{init} would be. Either contact dynamics starts at first contact where $\xi = 0$ and thus $a_{\mathrm{init}} = a_0$ or at the equilibrium contact radius $a_{\mathrm{init}} = a_{\mathrm{ad}}$ where $\xi > 0$ and thus the particle centers must have moved instantaneously. These two possibilities are discussed in more detail later (see Sec. 2.4.2).

A main feature of any dissipative contact dynamics is the asymmetric loading and unloading stages of the collision indicating a broken time symmetry (cf. Sec. 2.1). The compression can be described as a damped nonlinear oscillation. Although the dynamics is very sensitive to material parameters, two different collisional outcomes, aggregation and restitution, can be expounded. Short-range forces are able to prevent a post-collisional separation at the end of a collision at time $t = \tau_N$ and compression $\xi_{\text{final}} = \xi(\tau_N)$. It has been shown in experiments of adhesive collisions that a tearing off occurs rather late at $\xi_{\text{final}} < 0$ and $a_{\text{final}} > 0$ (Muller et al., 1980; Greenwood, 1997). The final contact radius $a_{\text{final}} = a_{\text{sep}}$ where $F_{\text{total}}(a)$ assumes its minimum of $-3\pi\gamma_S R_{\text{eff}}/2$ is determined by $\partial/\partial a\ (F_{\text{total}}(a_{\text{sep}})) = 0$ and $\partial^2/\partial a^2\ (F_{\text{total}}(a_{\text{sep}})) > 0$, yielding

$$a_{\text{sep}}^3 = \frac{9\pi}{8} \frac{\gamma_S R_{\text{eff}}^2}{E_{\text{eff}}} . \tag{2.54}$$

At this point, where a post-collisional separation occurs, $F_{\text{total}} = F_{\text{bond}}$ exactly matching the force necessary to break the bond and separate the grains (cf. Eq. (2.30)). However, there is experimental evidence that the force necessary to separate the particles is larger than that to overcome the surface forces alone. It is larger by a factor which is very dependent upon the separation rate (Greenwood and Johnson, 1981). Anyhow, fast initial as well as slow final snapping dissipate energy. The latter is given by the final contact area related to a_{sep}. The energy needed to deform two grains from one initial contact area a_1 to a second one a_2 reads

$$\Delta E_{(a_1 \to a_2)} = \int_{\xi_1}^{\xi_2} F_{\text{total}}(\tilde{\xi}) \mathrm{d}\tilde{\xi} = \int_{a_1}^{a_2} F_{\text{total}}(\tilde{a}) \frac{\partial \tilde{\xi}}{\partial \tilde{a}} \mathrm{d}\tilde{a} \tag{2.55}$$

$$= \pi\gamma_S\ (a_2 - a_1)(a_2 + a_1) + \frac{8}{15} \frac{E_{\text{eff}}}{R_{\text{eff}}^2}\ (a_2^5 - a_1^5) - \frac{20}{21} \frac{\sqrt{2\pi\gamma_S E_{\text{eff}}}}{R_{\text{eff}}}\ (a_2^{7/2} - a_1^{7/2}) . \tag{2.56}$$

The terms on the right-hand side of Eq. (2.56) signify in the order of their appearance surface energy for a given contact (cf. introduction of adhesive contacts in Sec. 2.2.2), restored elastic energy, and an additional adhesive term. The latter actually corrects the elastic energy for the fact that particles, while being deformed, attract and repel each other at the same time. The energy stored in a contact of arbitrary contact radius a (i.e. integrating from $a = 0$ to a) yields

$$E_{\text{snap}} = \pi\gamma_S\, a^2 + \frac{8}{15} \frac{E_{\text{eff}}}{R_{\text{eff}}^2}\, a^5 - \frac{20}{21} \frac{\sqrt{2\pi\gamma_S E_{\text{eff}}}}{R_{\text{eff}}}\, a^{7/2} . \tag{2.57}$$

Obtaining the coefficient of restitution ε_N, as introduced in Sec. 2.1, as the ratio of separation and impact speed but independently of the definition of either ξ_{init} or ξ_{final} by

$$\varepsilon_N = \frac{\dot{\xi}(\tau)}{\dot{\xi}(0)} \iff \varepsilon_N = \frac{\dot{a}(\tau) \cdot \xi'(a(\tau))}{\dot{a}(0) \cdot \xi'(a(0))} = \frac{\dot{a}(\tau) \cdot \xi'(a_{\text{final}})}{\dot{a}(0) \cdot \xi'(a_{\text{init}})} , \tag{2.58}$$

it is possible to distinguish between agglomeration and restitution in terms of the impact speed v_{imp}. Agglomeration, i.e. $\varepsilon_N = 0$, indicates a complete dissipation of the relative kinetic energy of normal motion $\dot{d} = \dot{\xi}(\tau_N) = 0$, whereas restitution $\varepsilon_N > 0$ implies a post-collisional separation of both particles at $\dot{d} = -\dot{\xi}(\tau_N) > 0$. For a purely elastic impact

($\varepsilon_N = 1$), no kinetic energy is dissipated. It has to be noted that considering initial and final surface reorganization in terms of E_{snap}, impact v_{imp}, and separation speeds v_{sep}, and thus the restitution coefficient ε_N have to be corrected according to Eq. (2.57).

2.3.1 Approximation for *Hertzian* Relation

Assuming the *Hertzian* relation $\xi R_{\mathrm{eff}} = a^2$ to be valid and considering maximal dissipation $B_{\mathrm{vis}} = 0$, Eqs. (2.25) and (2.47) become

$$\begin{aligned} F_{\mathrm{static}}(\xi) &= \frac{4}{3} E_{\mathrm{eff}} \sqrt{R_{\mathrm{eff}}}\, \xi^{3/2} - \sqrt{8\pi E_{\mathrm{eff}} \gamma_S}\, (R_{\mathrm{eff}} \xi)^{3/4} && (2.59) \\ F_{\mathrm{vis}}(\xi) &= 2 E_{\mathrm{eff}} \sqrt{R_{\mathrm{eff}}}\, \dot{\xi}\, \xi^{1/2}\,, && (2.60) \end{aligned}$$

respectively. The resulting equation of motion reads (Spahn et al., 2004)

$$m_{\mathrm{eff}}\, \ddot{\xi}(t) + \frac{3}{2} A_{\mathrm{vis}} H \xi(t)^{1/2}\, \dot{\xi}(t) + H\xi(t)^{3/2} - \sqrt{6\pi\gamma_S H R_{\mathrm{eff}}}\, \xi(t)^{3/4} = 0 \quad (2.61)$$

where in order of their appearance the acceleration terms signify inertia, viscoelastic dissipation, elasticity, and adhesion with the *Hertzian* factor $H = 4E_{\mathrm{eff}}\sqrt{R_{\mathrm{eff}}}/3$. Further on, $\gamma_S = \gamma_1 + \gamma_2$, i.e. $\gamma_{12} = 0$, as for particles in a vacuum space (Attard and Parker, 1992). Here, the initial conditions are a bit easier to determine. Initial contact of the particles will occur at $\xi_{\mathrm{init}} = 0$ at a corresponding contact radius of $a_{\mathrm{init}} = 0$. Both particles separate if a compression of $\xi_{\mathrm{final}} = \xi_{\mathrm{init}} = 0$ is reached. Agglomeration and restitution are crucially determined by the impact speed v_{imp}. While smaller impact speeds ($v_{\mathrm{imp}} < v_{\mathrm{cr}}$) will lead to agglomeration, higher impact speeds ($v_{\mathrm{imp}} > v_{\mathrm{cr}}$) cause restitution. In case of agglomeration when $\dot{\xi}(\tau_N) = 0$, a nonzero compression in accordance with Eqs. (2.29) and (2.61) remains

$$\xi_{\mathrm{ad}} = \frac{a_{\mathrm{ad}}^2}{R_{\mathrm{eff}}} = \left(\frac{6\pi\gamma_S R_{\mathrm{eff}}}{H}\right)^{2/3} \quad (2.62)$$

which actually is independent of the impact speed. It denotes the second fixed point solution of the contact dynamics additional to $\xi = 0$ and arises from an equilibrium between elastic restoring and adhesive attractive forces $F_{\mathrm{static}}(\xi_{\mathrm{ad}}) = F_{\mathrm{el}}(\xi) - F_{\mathrm{ad}}(\xi) = 0$. Figure 2.2 qualitatively compares the impact dynamics of different scenarios. Fixing the impact speed, merely the kind of contact was altered to be purely elastic, viscoelastic, purely adhesive elastic, or combined adhesive viscoelastic. An elastic contact (solid line) shows no dissipation and is reversible in time. This is clearly visible in the symmetric deformation during the first positive half-cycle. Although the overall shape of the deformation in time does change a bit[7], the same symmetry applies in terms of this simplified approach in case of an adhesive elastic contact (dotted line). Compression will be higher since superposed attractive forces are active during contact. However, only with the introduction of dissipation the dynamics becomes irreversible. Coefficients of restitution are less than one, the collision time τ_N is prolonged, and only in this case sticking is possible (dashed-dotted line). The adhesive viscoelastic contact continues to oscillate but is continuously damped until the equilibrium deformation ξ_{ad} has been reached. Thus, if $E_{\mathrm{snap}} = 0$, adhesion alone is not sufficient to enable aggregation. As elasticity, adhesion is a purely conservative force in the limit of this approximation. No hysteresis applies. Only in the presence of dissipation can particles eventually stick together.

---

[7] Adhesion generally features a hysteresis which is not apparent anymore in the limit of this approximation.

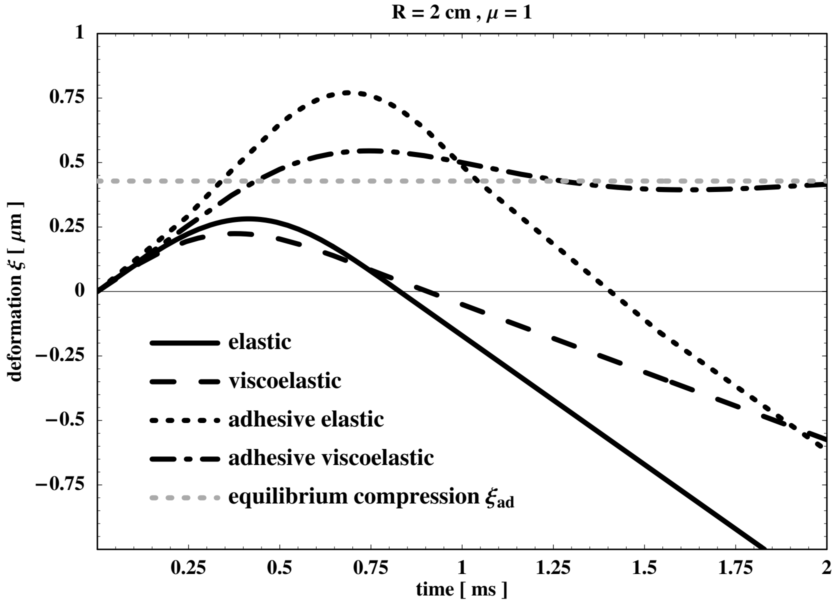

Figure 2.2: Qualitative solution of Eq. (2.61) for pure elastic (solid), viscoelastic (dashed), pure adhesive elastic (dotted), or combined adhesive viscoelastic contacts (dashed-dotted) for same material parameters and impact speed v_{imp}. Introducing adhesion clearly increases the overall compression. But only the introduction of dissipation, in this case viscous dissipation, prolongs the collision time τ and breaks the symmetry with respect to time in both cases. Furthermore, only the combined effects of adhesion and dissipation lead to sticking if $E_{\text{snap}} = 0$. Thus, within the *Hertzian* approximation dissipation crucially influences whether a collision will result in either agglomeration or restitution.

2.4 Full Numerical Solution

Numerically solving Eq. (2.50) yields the restitution coefficient ε_{N} as a function of the impact speed v_{imp} as presented in Fig. 2.3. We applied material parameters as given in Table 2.1 and used equally sized ($\mu = 1$) particles of 2 cm radius. The general behavior of ε_{N} is similar for different materials: small impact velocities result in an aggregation of particles ($\varepsilon_{\text{N}} = 0$) and after a more or less steep increase of ε_{N} it decreases again for larger impact speeds. In order to show the influence of the surface tension γ_{S} on ε_{N}, Fig. 2.4 shows the restitution coefficient for the same material but arbitrarily changed surface tensions.

Material	Y [Pa]	ν	ρ [kg m^3]	γ [N m^{-1}]	E_{eff} [Pa]
Quartz	5.4×10^{10}	0.17	2.6×10^3	0.025	2.78×10^{10}
Graphite	1.0×10^{10}	0.32	2.2×10^3	0.075	5.57×10^9
Ice	7.0×10^9	0.25	1.0×10^3	0.370	3.73×10^9

Table 2.1: Material parameters for various materials (Dominik and Tielens, 1997). Since we consider only collisions among particles of the same material the effective elasticity E_{eff} is given above. However, collisions between grains of different materials can easily be computed using appropriate material constants.

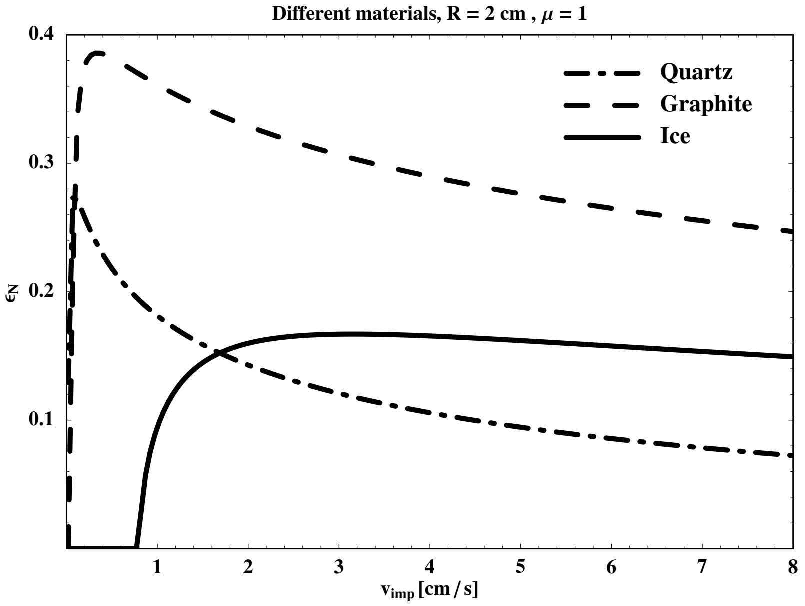

Figure 2.3: Coefficient of restitution for different materials as given in Table 2.1. Material response and thus collisional outcome are overall different and range from almost no aggregation at all for reasonable impact speeds to a significant amount of sticking. However, for materials presented here the dissipated energy amounts to at least half the kinetic impact energy.

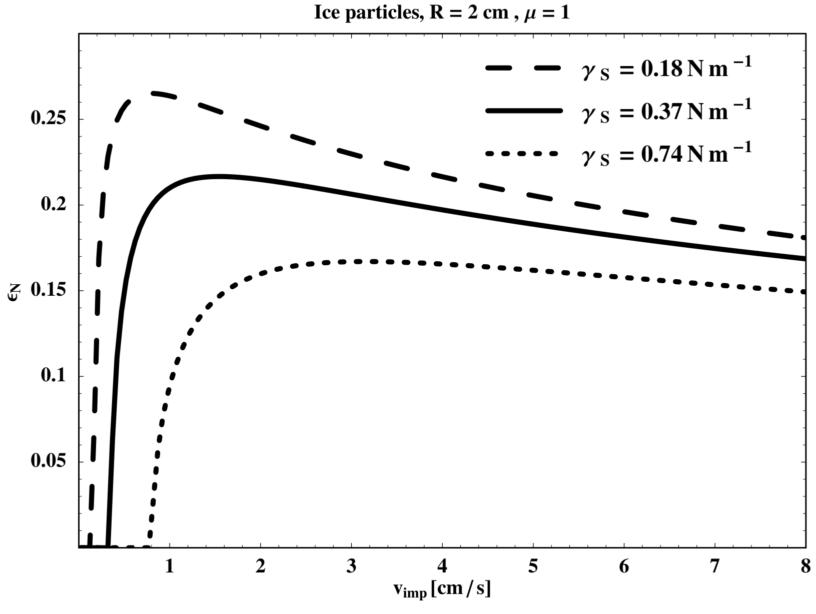

Figure 2.4: Coefficient of restitution for icy particles with artificially varying surface tensions γ_S in order to illustrate the influence of this parameter. Higher values of γ_S will lead to higher critical impact speeds as well as to overall more dissipative contacts within 10%. Note, $E_{\mathrm{snap}} = 0$ for the *Hertzian* approximation.

2.4.1 Application to Ice at Low Temperatures

Numerically solving the simplified Eq. (2.61) using material properties for ice at low temperatures as given in Table 2.1 yields aggregation as well as restitution (Albers and Spahn, 2006). The viscous parameter of $A_{\rm vis} = 10^{-4}\,$s were fitted to results in (Brilliantov et al., 1996). Restitution occurs for higher impact speeds ($v_{\rm imp} > v_{\rm cr}$), where both particles separate as indicated by $\xi < 0$. Gray curves depict this in Fig. 2.5. Displayed impact speeds have been chosen to illustrate the transition from agglomeration to restitution.[8] It is clearly visible in this direct comparison of different impact speeds for a single material, that any aggregative collision reaches its equilibrium compression $\xi_{\rm ad}$ independent from $v_{\rm imp}$. $\xi_{\rm ad}$ ranges within 10^{-7} to 10^{-5} m for grains of mm up to tens of meters in size, which is the size range of particles in planetary rings. The amount of dissipated energy $\Delta E_{\rm kin}' = (1-\varepsilon_N^2)E_{\rm kin}$ is illustrated in Fig. 2.6 for varying impact speeds via the restitution coefficient obtained by Eq. (2.58). In case of the *Hertzian* approximation, restitutive collisions including adhesion are generally more dissipative than pure viscoelastic ones, i.e. $\varepsilon_{\rm N}$ is overall smaller (see Sec. 2.3.1 and in particular Fig. 2.2). This finding is in accordance with experimental observations by Hatzes et al. (1991).

For perfectly smooth, icy spheres the restitution coefficient has been obtained numerically and analytically in previous studies (Dilley, 1993; Brilliantov et al., 1996; Thornton, 1997) and measured in lab experiments (Bridges et al., 1984; Hatzes et al., 1988; Supulver et al., 1995; Dilley and Crawford, 1996; Higa et al., 1998) with respect to an application to planetary rings. Experiments that studied collisions of frost covered icy particles (Hatzes et al., 1991; Bridges et al., 1996; Supulver et al., 1997) observed not only the restitution but also an agglomeration of grains under certain impact conditions. Theoretical considerations can account for both physical scenarios, restitution and agglomeration, if attractive forces are considered (e.g. Spahn et al., 2004; Albers and Spahn, 2006). Purely viscous surface layers however, can enable the complete dissipation of relative kinetic energy but will not result in the creation of a bond between the grains (Albers, 2002; Hertzsch, 2002)

Bridges et al. (1984) measured ε_N for ice particles of 2.75 cm radius in head-on collisions at low temperatures. Assuming a pure viscoelastic contact, i.e. applying $\gamma_{\rm S} = 0$ to Eq. (2.61), it is possible to reproduce their results qualitatively (dotted line in lower part of Fig. 2.6). Numerical results may be fitted to match experimental ones (as done in Brilliantov et al., 1996). Their results are depicted as the dashed-dotted line in Fig. 2.6. An agglomeration of particles has been observed in experiments with frost covered icy grains of 2.5 cm radius (Hatzes et al., 1991; Bridges et al., 1996). Particles had different frost coatings of various thicknesses. The measured sticking velocities were around 0.03 $\rm cm\,s^{-1}$ but never exceeded 0.4 $\rm cm\,s^{-1}$. Results obtained in our numerical studies for the critical impact speed $v_{\rm cr}$ are in good agreement with these observations. Note, that for a proper comparison of these results, $R_2 \rightarrow \infty$ has to be considered in order to account for a flat wall used in these experiments as one of the collision partners. Repeated collisions significantly change the surface structure by compressing the frost layer and thus strongly influence the sticking behavior (Hatzes et al., 1988). This leads to an overall more elastic contact, which is not accounted for in the present model. The sticking forces vary widely with the surface structure and impact speeds, where in this model $F_{\rm bond}$ does not depend on either one but merely on the effective grain size $R_{\rm eff}$. For the same reason, $\xi_{\rm ad}$ does not depend on $v_{\rm imp}$ in deviation from experimental findings. However, especially for varying surface structure and multiple collisions, $\gamma_{\rm S}$ is widely unknown.

Previous studies (Dilley, 1993; Dilley and Crawford, 1996; Higa et al., 1998) indicated the

---

[8] For the same reason increasing impact speeds $v_{\rm imp}$ are chosen in Figs. 2.5-2.8.

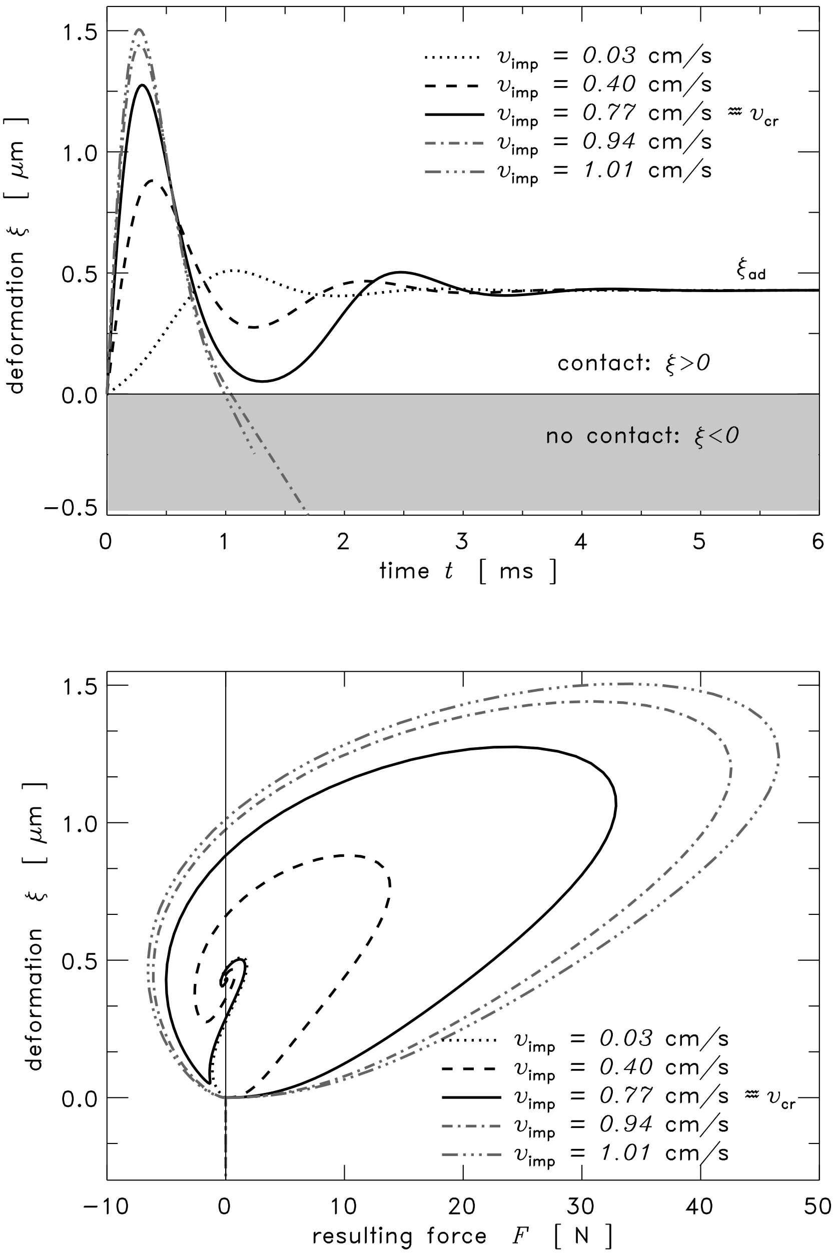

Figure 2.5: Contact Dynamics: The numerical solution of Eq. (2.61) for spherical icy grains ($R = 2\text{cm}, \mu = 1$) provides details about the indentation $\xi(t)$ (upper part) and the resulting contact force $F(\xi)$ (lower part) for varying impact velocities v_{imp}. Increasing impact speeds denote the transition between agglomeration and restitution. Any non-restitutive collision is a damped oscillation. In case of aggregation ($\tau_N \to \infty$, $v_{\text{imp}} < v_{\text{cr}}$) a nonzero deformation ξ_{ad} remains as given in Eq. (2.62), while the resulting force still vanishes (black lines). A remaining contact force F_{ad} according to Eq.(2.30) balances elastic repulsion leading to $F(\xi) = 0$. The maximum penetration increases with increasing impact speed. Grey lines denote restitutive impacts occurring at higher v_{imp}.

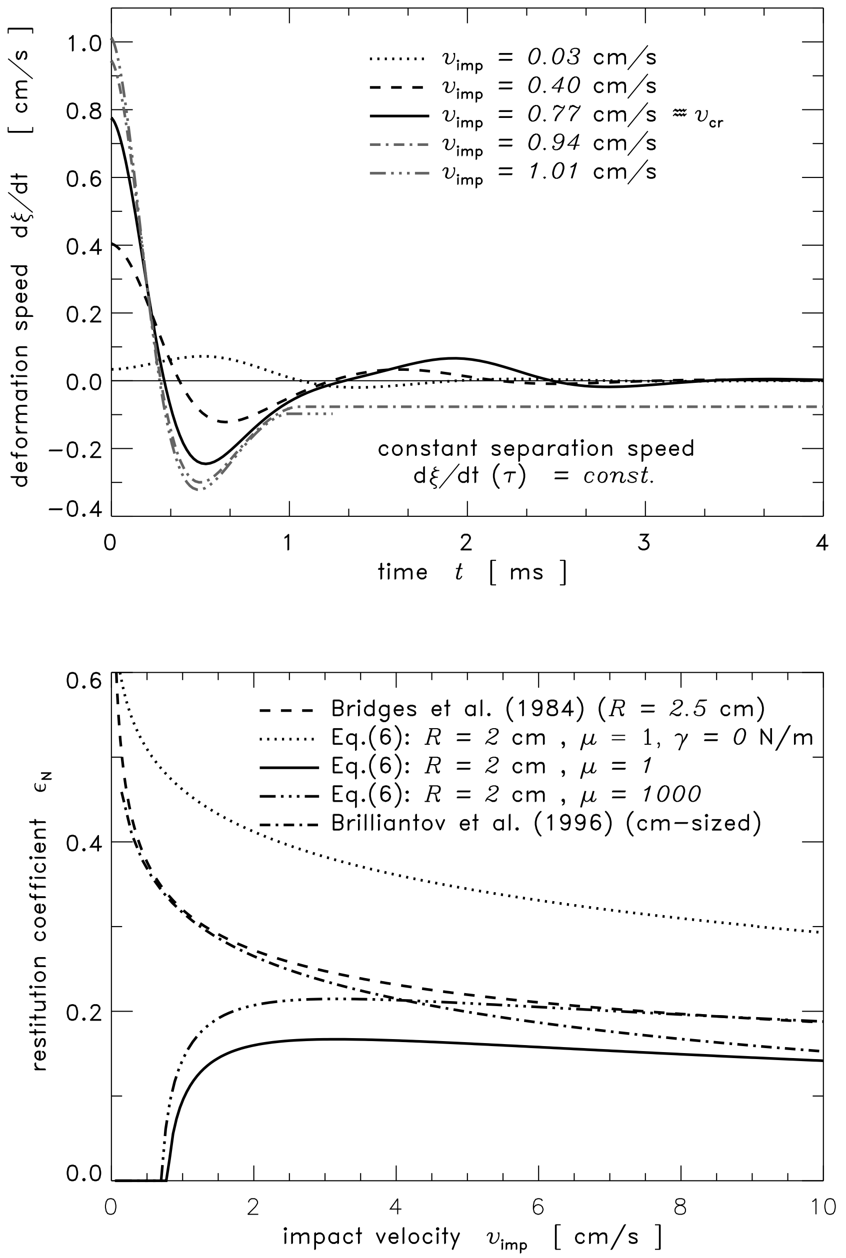

Figure 2.6: Restitution coefficient: Increasing impact speeds give rise to different impact scenarios: agglomeration and restitution. Both outcomes can be easily distinguished in terms of the restitution coefficient $\varepsilon_N(v_{imp})$ (lower part) ($\varepsilon_N = 0$: aggregation $\longleftrightarrow$ $\varepsilon_N > 0$: restitution). The indentation speed $\dot{\xi}(t)$ (upper part) is illustrated for icy grains ($R = 2\mathrm{cm}, \mu = 1$) as in Fig. 2.5 and vanishes in case of aggregation. The adhesive viscoelastic impact model is in qualitatively good agreement with lab measurements. Impacts are overall more dissipative than in the pure viscoelastic case in agreement with experimental findings (Hatzes et al., 1991).

importance of the size of colliding grains, yielding more elastic contacts for larger particles than for smaller ones. The size dependence of the collision dynamics of Eq. (2.61) is illustrated in terms of the collision time τ_N (Fig. 2.7, upper part) and the restitution coefficient ε_N (Fig. 2.7, lower part). The collision time τ_N increases with a decreasing impact speed. It usually ranges within a few milliseconds for cm-sized grains, but abruptly reaches infinity in case of agglomeration ($v_{\mathrm{imp}} \leq v_{\mathrm{cr}}$). Collisions themselves are more and more conservative for larger particles as indicated in Fig. 2.7. This trend towards pure elasticity also holds for contacts of different proportions ($\mu \neq 1$). Our results are in fair agreement with their findings as given in Higa et al. (1998) for frosted-surface ice.

In our numerical simulations, the collisional outcome is determined by the impact velocity on one hand and by grain sizes on the other. A mass-velocity parameter space is thus divided into sections of agglomeration and restitution (Spahn et al., 2004). Smaller particles (mm in size) are very likely to stick to each other or to larger ones, whereas larger particles have to have a rather small impact velocity in order to agglomerate. Nevertheless, the critical velocity for restitution to occur becomes drastically smaller for increasing masses as shown in Fig. 2.8.

2.4.2 Comparison of Approximative and Full Dynamics

In this Section two previously discussed approaches of treating the collision dynamics are compared. The approaches will hereafter be denoted as scenario A) and B) and denote:

A) Solving Eq. (2.50) in terms of the contact radius a while $a_{\mathrm{init}} = a_0$ and $a_{\mathrm{final}} = a_{\mathrm{sep}}$ taking into account initial and final snapping energies.

B) Solving Eq. (2.61) in terms of the compression ξ (Spahn et al., 2004; Albers and Spahn, 2006).

As long as the collision duration τ_N is negligible compared to timescales of ensemble dynamics, only the outcome of a collision is important to further kinetic studies. Since ε_N defines agglomeration and restitution as revealed before, we concentrate on this parameter for this comparison.

Two major assumptions distinguish approach B) from A):

- The actual ξ-a relation (see Eq. (2.32)) is approximated by the *Hertzian* relation (Eq. (2.25))
- The dissipation is approximated by its major contribution via A_{vis} and thus $B_{\mathrm{vis}} = 0$.

For comparison, different numerical solutions of ε_N are shown in Fig. 2.9 for exemplary material parameters of ice (Table 2.1). Grey lines denote simulation results according to the full dynamics (A) whereas black lines refer to results obtained according the approximative equation (B). Applying the same parameters to either Eq. (2.50) or (2.61), and thus solving either scenario A) or B) respectively, it becomes clear that the main difference between both approaches does not arise from a *Hertzian* contact area assumption ($a^2 \sim R_{\mathrm{eff}}$). Thus, applying the exact ξ-a relation does not significantly improve the approximation. However, varying the dissipative parameters A_{vis} and B_{vis} only slightly, results in more drastic changes. In this sense, it is possible to imitate results obtained by Eq. (2.61) by putting $B_{\mathrm{vis}} = 0$ in Eq. (2.50) within a few percent of accuracy. Note, Eq. (2.49) coincides with

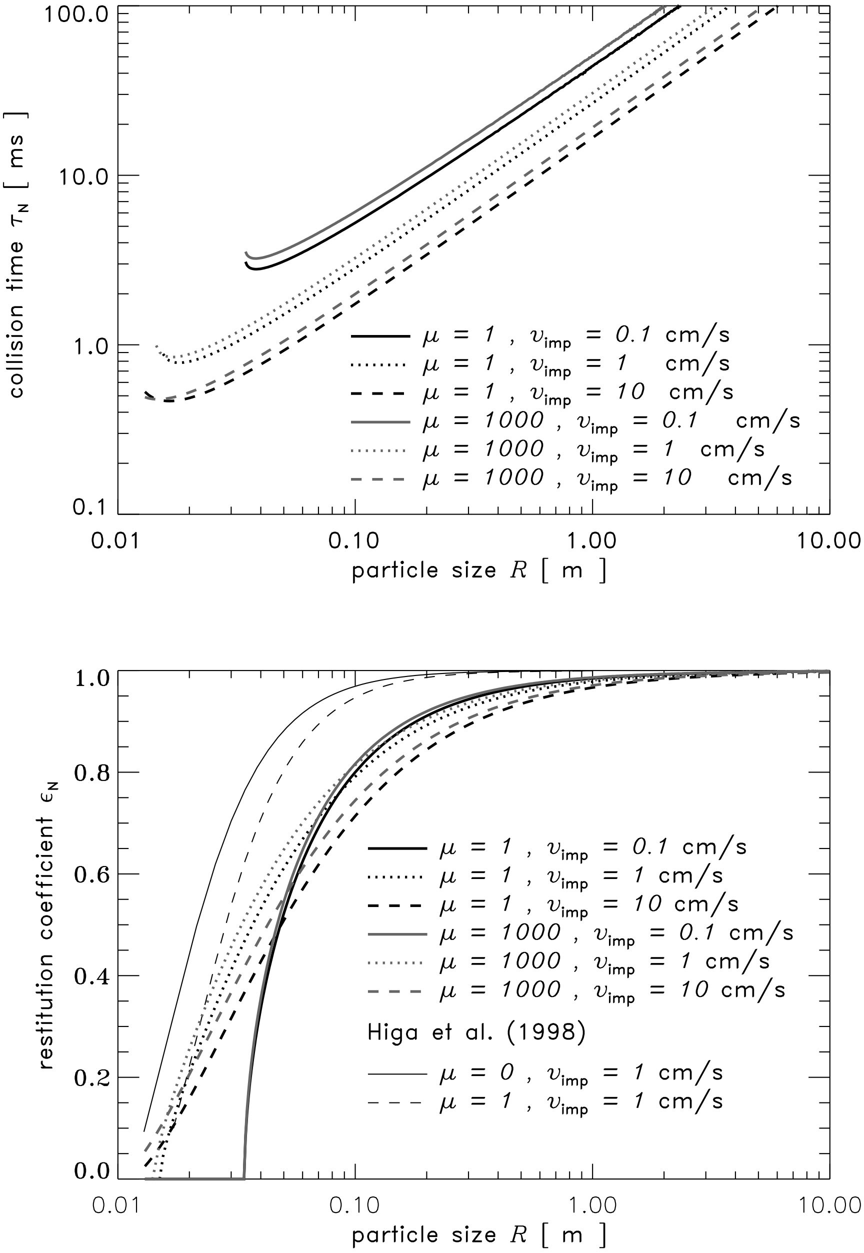

Figure 2.7: Size dependence: The collision time τ_N increases with increasing particle sizes (upper part). It is plotted for varying impact speeds v_{imp} and different particle size ratios μ. For larger grains it can be described by a power law $\tau_N \sim R^k$ where the index $k = 50/3 \approx 16.7$. A collision of cm-sized grains e.g. occurs within milliseconds. Larger grains show more elastic collisions (lower part). Despite its dependence on v_{imp} (cf. Fig. 2.6), the restitution coefficient ε_N is qualitatively insensitive to v_{imp} compared to its size dependence. Smaller grains stick together below a certain impact speed v_{cr}, which is smaller for larger particles (see also Fig. 2.8). Thin solid and dashed line denote the model presented in Dilley and Crawford (1996, Fig. 1) with parameters taken from Higa et al. (1998).

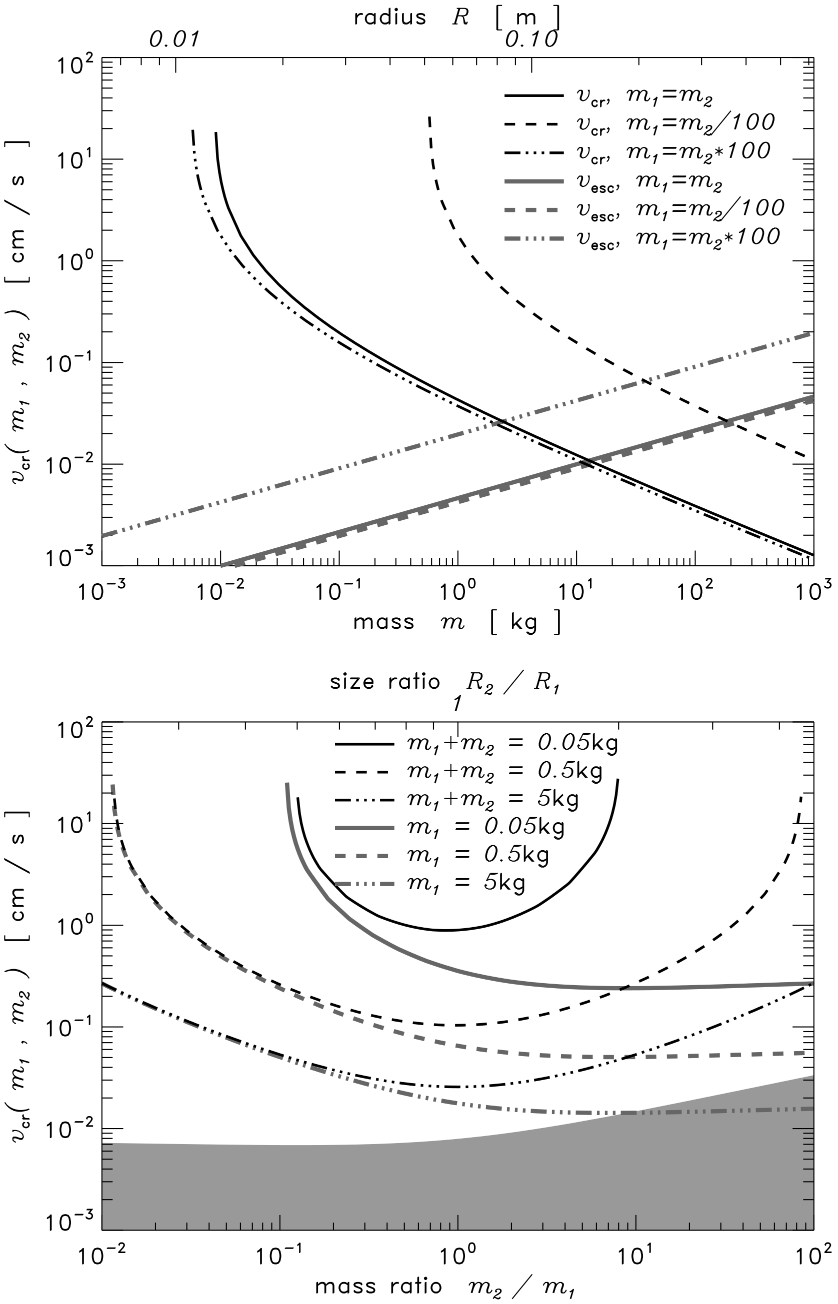

Figure 2.8: Critical velocity: The critical impact speed v_{cr} is obtained from numerical solutions of Eq. (2.61). The size (upper part) and size ratio dependence (lower part) are shown for different proportions. In general, smaller and slower grains tend to agglomerate while others do restitute. The gravitational escape velocity v_{esc} is given as a reference in either grey lines (upper part) or as a grey shaded area (lower part). The influence of either adhesive processes or gravitational influence can therefore be clearly distinguished.

Eq. (2.61) for $B_{\mathrm{vis}} = 0$. The additional damping term related to B_{vis} arising from the superposed adhesive force will always give a "positive" feedback due to its sign and actually decrease the effect of dissipation. This is clearly visible in Fig. 2.9, in particular for the gray, dashed-dotted line, since restitution coefficients are generally larger for $B_{\mathrm{vis}} \neq 0$ than for $B_{\mathrm{vis}} = 0$. Even while $B_{\mathrm{vis}} = 0$ the full dynamics does not reach the amount of dissipation as the approximative one (cf. the grey and black solid lines in Fig. 2.9). Thus, approach B) denotes a good approximation. Further investigations will show the overall impact of accounting for adhesive interactions. Uncertainties of e.g. viscous parameters can easily be improved by fitting to experimental data.

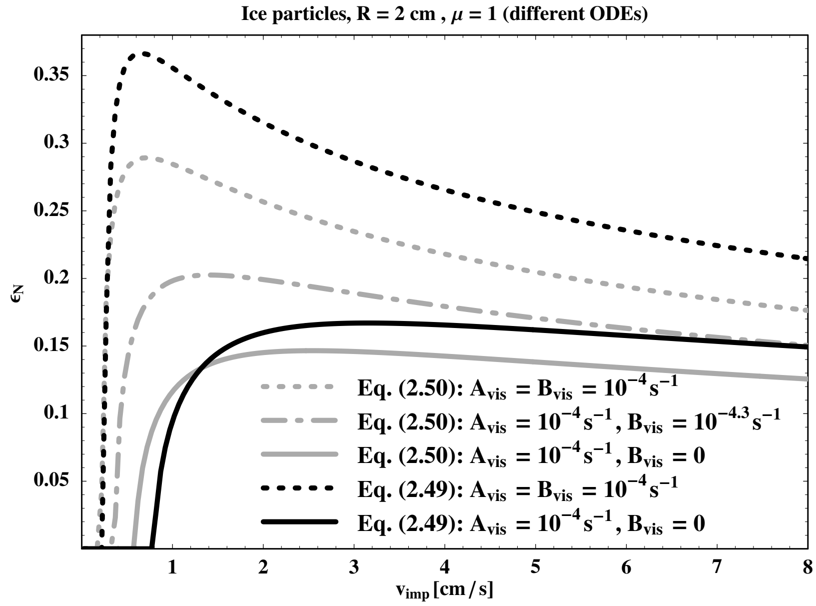

Figure 2.9: Restitution coefficients for different dynamical approaches: Gray lines refer to Eq. (2.50) which has been solved where $a_{init} = a_0$ and $a_{final} = a_{\mathrm{sep}}$ were applied. Initial and final snapping energies E_{snap} have been disregarded while different damping parameters A_{vis} and B_{vis} were applied. Black lines denote Eq. (2.49) which in case of $B_{\mathrm{vis}} = 0$ coincides with Eq. (2.61) (Albers and Spahn, 2006). The restitution coefficient ε_{N} is mainly influenced by different damping conditions. The approximation of applying the *Hertzian* relation is of minor importance.

However, as shown in Fig. 2.9, the influence of initial and final snapping energies has been neglected. Since these energies would be dissipated, the effect of their inclusion can easily be estimated:

- If energy is dissipated for a surface reorganization and slight compression of the grains during initial snapping, the actual impact speed v_{imp} will be smaller than the normal component of the particle's relative impact velocity g_{N}, chosen as the apparent impact speed in the results presented. The graph of the restitution coefficient would be shifted towards higher impact velocities without changing its actual shape. Collisions with impact speeds usually resulting in restitution would partially result in aggregation. Additionally, even in the absence of viscous dissipation, $A_{\mathrm{vis}} = B_{\mathrm{vis}} = 0$, agglomeration becomes possible. All relative kinetic energy would be dissipated while forming an equilibrium contact area. Therefore, due to a hysteresis, purely adhesive elastic collisions are irreversible and can lead to sticking in terms of approach A), whereas dissipation and adhesion is necessary to enable agglomeration in terms of approach B).

- Energy can only be dissipated during final snapping if particles separate. Thus, final snapping does influence restitution alone. The separation speed g'_N would then be yet smaller if corrected for the dissipated energy. The curve of the restitution coefficient could simply be multiplied with an impact speed dependent correction factor smaller than unity. Contrary to initial snapping, final snapping does influence the shape of the restitution coefficient but does not change the critical impact speed v_cr. Thus, it may be neglected while numerically determining the latter.

However, what happens during an initial contact is a complex surface reorganization and deformation of the material which is not covered by the presented continuum contact model, i.e. neither scenario A) nor B). Here, this would go into too much detail and miss the point of this study, namely to show the general effects of adhesive particle collisions on a granular ensemble either force-free or in a central field. Therefore, the actual energy lost during first contact will be approximated by Eq. (2.57) for $a = a_\mathrm{init}$ and has been quantified in Table 2.2 in terms of velocities for different contact radii a_0, a_ad, and a_sep. Values have exemplary been chosen for radii of $R = 0.02$ cm and $R = 2$ m, and size ratios of $\mu = 1$ and $\mu = 10^3$ for different materials as given in Table 2.1. Presenting the velocity rather than the energy E_snap allows for a simple estimate of how much the impact speed g would change by v if the effect of either initial or final snapping is taken into account. Note, E_snap is related to the relative kinetic energy by $E_\mathrm{snap} = E_\mathrm{kin} = m_\mathrm{eff}\, v^2/2$. Particles "jumping" into contact forming a_init of either a_0 or a_ad will dissipate the corresponding amount of energy and the apparent impact speed would read $v_\mathrm{imp} = g_\mathrm{N} - v$, whereas in case of separation at a contact radius of a_sep the separation speed reads $g'_\mathrm{N} = \dot{\xi}(\tau_\mathrm{N}) - v$. The restitution coefficient is then given by $\varepsilon_\mathrm{N} = g'_\mathrm{N}/g_\mathrm{N}$ as usual.

In case of scenario A) there is yet another, additional uncertainty about the initial contact area a_init. There have been discussions about whether particles would form an initial contact area of radius $a_\mathrm{init} = a_0$ or an equilibrium contact with radius $a_\mathrm{init} = a_\mathrm{ad}$. The latter not only assumes a surface reorganization but also a non-negligible motion of the particle's centers which is not covered by the model introduced here. In case of $a_\mathrm{init} = a_0$ only the surface reorganization is assumed to happen instantaneously while the following motion, the actual relative motion i.e. including the particles being pulled together in the first place, can be covered by the equations of motion presented here. We prefer the first ($a_\mathrm{init} = a_0$) and have used it in previous numerical solution. However, this discussion is of purely theoretical interest. It is quantified in Table 2.2 and additionally illustrated in Fig. 2.10. The influence of different initial conditions is negligible with respect to the critical velocity v_cr and leads to only 10% of change in the overall restitution.

Thus, to summarize and finalize the comparison of both approaches:

- Scenario A)
  - Description of the collision dynamics in terms of the contact radius a allows for an accurate treatment of the ξ-a relation.
  - Unresolved discussion about the initial contact radius points towards $a_\mathrm{init} = a_0$, however, proves to be of purely theoretical interest.

			a_0 [μm]	v [cm/s] $\times 10^{-4}$	a_{ad} [μm]	v [cm/s] $\times 10^{-4}$	a_{sep} [μm]	v [cm/s] $\times 10^{-4}$
$R = 0.02$ m	$\mu = 1$	Quartz	10	11	14	27	9	10
		Graphite	26	52	33	125	21	44
		Iron	32	221	42	531	27	188
		Ice	50	335	65	803	41	284
	$\mu = 10^3$	Quartz	17	13	22	30	14	11
		Graphite	41	59	53	141	34	50
		Iron	51	248	67	596	42	211
		Ice	79	375	104	901	65	319
$R = 2.0$ m	$\mu = 1$	Quartz	224	0.2	294	0.6	185	0.2
		Graphite	553	1.1	724	2.7	457	1.0
		Iron	693	4.8	908	11.4	572	4.0
		Ice	1075	7.2	1410	17.3	888	6.1
	$\mu = 10^3$	Quartz	356	0.3	466	0.7	294	0.2
		Graphite	877	1.3	1150	3.0	724	1.1
		Iron	1099	5.3	1441	12.8	908	4.5
		Ice	1706	8.0	2236	19.4	1409	6.9

Table 2.2: Velocity corrections for various materials to be applied for different contact radii: Contact radius and related velocity for 2 cm sized particles. Numerical results obtained by Eq. (2.50) have to be corrected by a factor of v obtained by $m_{\mathrm{eff}}\, v^2/2 = E_{\mathrm{kin}} = E_{\mathrm{snap}}$ (Eq. (2.57)). In case of a_0 and a_{ad}, the actual impact speed reads $v_{\mathrm{imp}} = g_{\mathrm{N}} - v$, while for a_{sep} the actual separation speed reads $g'_{\mathrm{N}} = \dot{\xi}(\tau_{\mathrm{N}}) - v$. However, since v ranges from $\mu\mathrm{m\,s^{-1}}$ to $\mathrm{mm\,s^{-1}}$ corrections are only of minor influence.

  - Including initial and final snapping energies would further diminish differences between scenario A) and B).
  - Initial and final snapping in scenario A) are not completely understood and assumed to happen instantaneously. Additionally, they are neither covered by scenario A) nor B).
  - The experimentally observed bottle-neck creation before separation implies a material flow, definitely breaching the assumption of two flat surfaces in contact (cf. Sec. 2.2.1).
  - Sticking is possible even without viscous dissipation.

- Scenario B)
  - It introduces a robust model that can easily be implemented in further applications.
  - Viscous dissipation crucially influences whether grains do stick or not.
  - Results obtained by scenario B) are well confirmed by a number of experiments (cf. Sec. 2.4.1) and reproduce characteristic features that have been observed such as the oscillating relative motion, the occurrence of sticking as well as the generally smaller value of the restitution coefficient ε_{N} (Hatzes et al., 1991), the size dependence (Dilley, 1993; Higa et al., 1998) and the general sensitive dependence on the deformation rate (Greenwood and Johnson, 1981).

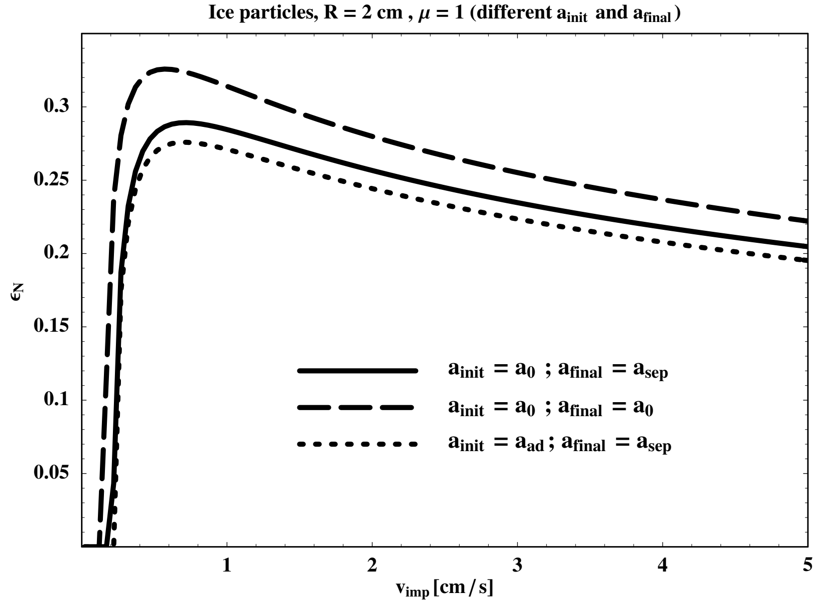

Figure 2.10: Restitution coefficient for different initial and final contact radii in Eq. (2.50). Although the absolute values of ε_{N} does change the critical velocity v_{cr} and the overall shape are the same. Differences sum up to about 10% where changes including corrections with respect to E_{snap} are negligible.

Despite minor differences leading to discrepancies within about 10% of the restitution coefficient, scenario B) denotes a reasonable, consistent model in order to treat the collision dynamics of adhesive, viscoelastic particles. It furthermore serves as an upper limit case for agglomeration since maximal dissipation is assumed. Results obtained by Eq. (2.61) denote a robust base and will be applied hereafter.

2.5 Applicability and Limitations

In this Chapter a model for low-velocity collisions of adhesive, viscoelastic particles was derived. It has been applied to various material parameters and compared to experimental data of ice at low temperatures to further detail. Being in fair agreement with experiments, it provides an essential, theoretical tool to cover the collisional interactions of granular particles in a more general context. This dynamical model meets the expectations in order to investigate coexisting collisional agglomeration and restitution on many-particle systems. Although collisional growth is possible it may be unlikely to account for a reasonable growth of larger objects. Nevertheless, as in case of pure gravity, smaller grains are likely to stick to larger ones, sensitively influencing the size distribution of such system. In the following chapters this model will be implemented in further studies on granular gases as there are the orbital evolution of two interacting grains under the influence of gravity and collisions (see Chapter 3) and a general kinetic study on growth processes (see Chapter 4).

However, the model presented here does neither include any specific surface coatings or textures nor repeated collisions. Since neither Eq. (2.50) nor Eq. (2.61) is valid for the tangential component of the contact dynamics, it only partially accounts for oblique impacts. If tangential loads are present in adhesive contacts studies showed a reduced contact load compared to the adhesive elastic one (Savkoor and Briggs, 1977). Note, that for an adhesive elastic contact the load was increased compared to the pure elastic, *Hertzian* case. For a better understanding, future models should yield a combined description including the collisional spin evolution. Furthermore, the model is limited by the *quasistatic* approximation, i.e. small viscosities and low impact velocities. It therefore cannot account for any sort of fragmentation. Impact speeds allowing for fragmentation denote the uppermost limit for even an extrapolated application of this theory.

Additionally, the currently published literature on material constants as well as the experimental findings on critical impact speeds is not satisfying. Elastic properties are well covered for a wide range of materials whereas viscoelastic properties and surface tensions are poorly known. Viscous parameters such as A_{vis} have been numerically fitted and showed that in a range of $\mathrm{cm\,s^{-1}}$ to $\mathrm{dm\,s^{-1}}$ with parameters between $A_{\mathrm{vis}} \in [0.8, 1.0] \times 10^{-4}\,\mathrm{s}$ a good agreement between theory and experiments can be achieved as has been done for purely viscous contacts before (Brilliantov et al., 1996). Anyhow, we would welcome more experiments on aggregative collisions. These would eventually improve theoretical modeling.

Chapter 3

Orbit Dynamics of Two Particles Subject to a Central Mass

The dynamics of granular gases under *Keplerian* shear differs fundamentally from force-free granular ensembles. Planetary rings mark the most striking examples of the first. Additional perturbations and the collective ensemble dynamics give rise to interesting structures such as voids and gaps. These ensemble assume a disk-like appearance due to the conservation of angular momentum. Examples vary from galactic disks, accretion disks, to planetary rings. Although different in nature, these astrophysical disks are subject to the same fundamental physical processes. Hydrodynamic modeling is one of the theoretical approaches to describe either planetary rings (Stewart et al., 1984; Shu et al., 1985b,a; Schmit and Tscharnuter, 1995, 1999; Spahn and Sremčević, 2000; Schmidt et al., 2001), accretion disks (Lynden-Bell and Pringle, 1974; Papaloizou and Lin, 1989; Kleiber and Glatzel, 1999), or galactic disks (Toomre, 1964; Binney and Tremaine, 1987). While direct collisions among the constituents can be neglected in galactic disks[1], they have a major impact in dense planetary rings. Due to inelastic collisions, latter are extremely flattened. Especially important to planetary rings' dynamics is the epicyclic motion of the particles that can be taken into account in a kinetic description of the N-particle dynamics (Goldreich and Tremaine, 1978; Shukhman, 1984; Araki and Tremaine, 1986). Besides these methods, also Monte-Carlo like N-body simulations of planetary rings (Frezzotti, 2001) and a local simulation method (Wisdom and Tremaine, 1988; Salo, 1991; Lewis and Stewart, 2000; Salo et al., 2001; Seiß et al., 2005) are employed. A detailed description of the latter may be found in Salo (1995).

A more detailed understanding of the underlying collision dynamics provides better insights into the evolution of planetary rings. Simulations done so far did only account for either a constant (Wisdom and Tremaine, 1988; Ohtsuki, 1993) or, more advanced, a velocity dependent coefficient of restitution (Salo, 1991; Salo et al., 2001; Schmidt et al., 2001) but did not allow for a vanishing restitution.

However, numerical simulations, as mentioned above, are quite time consuming and CPU demanding. Since the relevance of adhesive collision to planetary rings is still putative, we use a simplified approach to point out possible influences. Results will show whether an implementation of adhesion into large-scale simulations might be worthwhile. Here, the

---

[1] Stars within a galactic disk have a small cross-section and are massive enough for gravitational scattering to outweigh physical collisions.

collision dynamics presented in the previous chapter is applied to the relative orbital motion of two grains. Its effects are studied in an analytical approach in Sec. 3.1 and compared to simple numerical simulations in Sec. 3.2. Results are discussed in the context of Saturn's rings but can easily be translated to other planetary ring systems. For an application to pre-planetary disks, the influence of their gas component is considerable and results are only partially applicable.

3.1 Analytical Estimates

Considering two particles of masses, m_1 and m_2, in orbit about a central mass M, their equations of motion including pairwise interactions (*PI*) read

$$\begin{aligned} m_1\ddot{\vec{r}}_1 &= -\frac{GMm_1\vec{r}_1}{r_1^3} + PI\,[\,(\vec{r}_1-\vec{r}_2)\,]\,, && (3.1)\\ m_2\ddot{\vec{r}}_2 &= -\frac{GMm_2\vec{r}_2}{r_2^3} + PI\,[\,(\vec{r}_2-\vec{r}_1)\,]\,. && (3.2) \end{aligned}$$

Their dynamics may as well be expressed in their center of mass frame

$$\vec{r}_\mathrm{c} = \frac{m_1\vec{r}_1 + m_2\vec{r}_2}{m_1+m_2} \quad , \quad \vec{d} = \vec{r}_2 - \vec{r}_1\,, \tag{3.3}$$

where $\vec{d}$ denotes the relative distance between both particles as in Eq. (2.1). After series expanding the central gravity around $\vec{r}_\mathrm{c}$ and changing to a co-moving frame, the equations of motion may be written as

$$\begin{aligned} \frac{\mathrm{d}^2\vec{r}_\mathrm{c}}{\mathrm{d}t^2} &= -GM\frac{\vec{r}_\mathrm{c}}{r_\mathrm{c}^3}\,, && (3.4)\\ \ddot{\vec{d}} + 2\vec{\Omega}\times\dot{\vec{d}} + \vec{\Omega}\times(\vec{\Omega}\times\vec{d}) &= -\Omega^2\left(\vec{d} - \frac{3(\vec{d}\cdot\vec{r}_\mathrm{c})\vec{r}_\mathrm{c}}{r_\mathrm{c}^2}\right) + PI\,[\,\vec{d}\,]\,. && (3.5) \end{aligned}$$

where $\vec{\Omega} = \Omega\vec{e}_z$ with $\Omega = \sqrt{GM/r_\mathrm{c}^3}$ denotes the *Keplerian* orbit frequency. Equation (3.5) describes the relative motion and covers all inertia forces. As shown in Chapter 2, the collision dynamics allows for agglomeration and restitution. Since the dynamical timescales of restituting collisions, $\tau_\mathrm{N} \sim$ ms for cm-sized grains, are by orders of magnitude smaller than the average time between collisions for Saturn's rings, particle impacts are considered as instantaneous hereafter. Thus, only the collisional outcome is important to the dynamical evolution of the system, validating kinetic assumptions (e.g. Longaretti, 1989; Spahn et al., 2004). In case of restitution, particles are henceforth only influenced by the central body, their mutual gravity and mutual collisions. Agglomeration, on the other hand, revealed a remaining attractive bond ($\vec{F}_\mathrm{bond} = F_\mathrm{bond}\vec{e}_d$, Eq. (2.30)), which has to be taken into account for any ongoing orbital motion as a constant attractive force. In order to account for both collisional outcomes, particle interactions $PI\,[\,d\,]$ must be expressed accordingly

$$\begin{aligned} PI_\mathrm{rest}\,[\,\vec{d}\,] &= -G\frac{m_1m_2}{d^2}\,\vec{e}_d\,, && (3.6)\\ PI_\mathrm{agg}\,[\,\vec{d}\,] &= -\left(G\frac{m_1m_2}{d^2} + \frac{3}{2}\pi\gamma_\mathrm{S}R_\mathrm{eff}\,d\right)\vec{e}_d\,, && (3.7) \end{aligned}$$

where the former refers to restitution and the latter to agglomeration. An agglomerate of two grains is moving at the grains' center of mass velocity $\dot{\vec{r}}_c$. Exposed to tidal shear it can only exist, if it's internal bonds are strong enough to support it. Here, they are denoted by adhesive bonds F_{bond}. Additional to tidal disruptions, further perturbations as other collisions or scattering might destroy an agglomerate. Processes considered as erosion or fragmentation together with agglomeration could ensure a steady size distribution and will be discussed in subsequent chapters. In Sec. 3.1.1 the stability of aggregates in a tidal environment with respect to adhesive bonds is discussed qualitatively. Thus, instead of solving the dynamics of Eqs. (3.4)-(3.7) we will determine whether adhesion plays a noticeable role.

3.1.1 Stability of Two-Body Agglomerates

In this section, the stability of an agglomerate held together by adhesion and mutual gravity is discussed. A critical distance r_{crit} from the planet's center is found by analyzing particular grain configurations in orbit about a central planet. Any agglomerate, which is closer to the central body than this critical distance ($r < r_{\text{crit}}$), will inevitably be torn apart. Hereafter, agglomerates able to resist the tidal shear are referred to as stable and those torn apart as unstable. In order to determine the functional dependence of the borderline between stability and instability, two solid, spherical grains of arbitrary size are assumed to have formed an agglomerate according to Sec. 2.2.2 and "place" it at an arbitrary orbit location. At this point, complex dynamics such as the likelihood of a collision is waived in order to appraise the general effects of adhesion.

As shown in Sec. 2.3.1, the contact of such aggregates is static $\ddot{d} = \dot{d} = 0$ and implies a constant distance $d = R_1 + R_2 - \xi_{\text{ad}} = const.$ Since ξ_{ad} is of the order of $10^{-7} - 10^{-5}$ m, it is thus negligible and the second part of Eq. (3.3) can be approximated by $d \approx R_1 + R_2$. The properties of such two-particle agglomerates are particle radius $R = R_1$, size ratio $\mu = R_2/R_1$, spin angular velocity $\dot{\alpha}(t)$, orientation $\alpha(t)$, and surface energy γ_S. According to Fig. 3.1 we introduce $\vec{d} = d\vec{e}_d = d\cos\alpha\,\vec{e}_r + d\sin\alpha\,\vec{e}_\varphi$. For simplicity and in order to give a conservative estimate for maximal sizes of stable agglomerates, we assume $\vec{\omega} \perp \vec{d}$ and $\vec{d}||\vec{r}$, denoting maximum tidal and centrifugal forces, where ω is the spin of the aggregate. Equation (3.5) and Eq. (3.7) yield

$$-\Omega^2 d(1-3\cos^2\alpha) - \frac{G(m_1+m_2)}{d^2} + (\dot{\alpha}+\Omega)^2 d - \frac{3}{2}\pi\frac{\gamma_S R_{\text{eff}}}{m_{\text{eff}}} \quad = \quad 0\,. \tag{3.8}$$

The equilibrium distance r_{crit} emanates from the orbit frequency $\Omega^2_{\text{crit}} = GM/r^3_{\text{crit}}$ and can be obtained by solving Eq. (3.8). Note, $\dot{\alpha}$ denotes the spin with respect to the co-moving frame while the total spin is given by $\omega = \dot{\alpha} + \Omega$. It is sufficient to exceed the maximum bond strength once at a single point in time in order to break the bond. The further on motion is irrelevant and thus $\alpha = 0$ as a snapshot in time is assumed and will serve to describe the maximal tidal shear. However, although $\alpha = 0$ different rotation rates may be discussed. For convenience, we denote $\dot{\alpha} = k\Omega_{\text{crit}}$, where k is a real number. The critical orbit distance results in

$$r^3_{\text{crit}} \quad = \quad \frac{GMd\, m_{\text{eff}}\,[(k+1)^2+2]}{AD+SG}\,, \tag{3.9}$$

where $AD = 3\,\pi\gamma_S R_{\text{eff}}/2$ and $SG = G\,m_1 m_2\,d^{-2}$ refer to adhesive and gravitational particle interactions, respectively. Resolving the aggregate properties given above, Eq. (3.9) yields

$$r_{\text{crit}}^{3} = \frac{24GM\rho R^{3}\mu^{2}(1+\mu)^{3}\,[(k+1)^{2}+2]}{(1+\mu^{3})[27\gamma_{\text{S}}(1+\mu)+32\pi G\rho^{2}\mu^{2}R^{3}]}\,, \tag{3.10}$$

which further reduces in case of equally sized grains ($\mu = 1$) to

$$r_{\text{crit}}^{3} = \frac{48GM\rho R^{3}[2+(k+1)^{2}]}{27\gamma_{\text{S}}+16\pi\rho^{2}GR^{3}}\,. \tag{3.11}$$

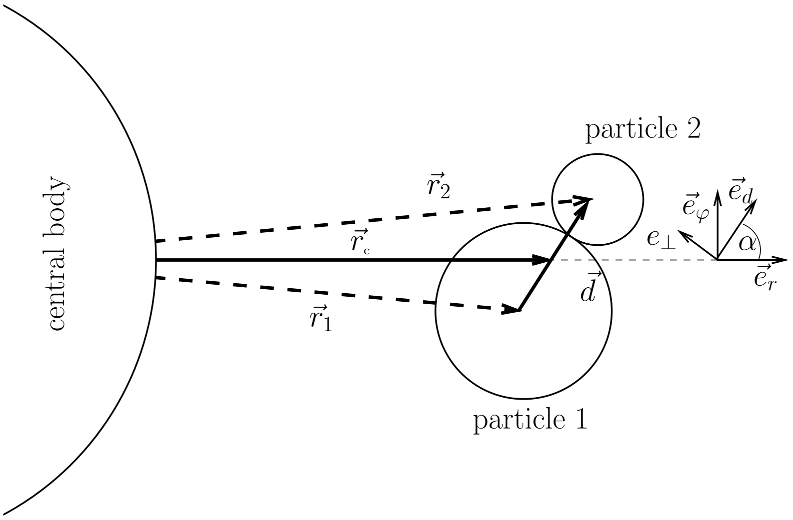

Figure 3.1: Schematic top-on view: The center of mass $\vec{r}_{\text{c}}$ of two orbiting particles is revolving anti-clockwise around the central body. Particles in contact may agglomerate and are able to spin around their main axis. The co-moving frame originates at $\vec{r}_{\text{c}}(\vec{e}_r,\ \vec{e}_\varphi)$ and the relative motion can be described in $(\vec{e}_d, \vec{e}_\perp)$. In case of two particles in contact α denotes the orientation of the agglomerate.

Generally, the critical distance r_{crit} may as well be obtained as an effective value according to

$$\frac{1}{\left(r_{\text{crit}}\right)^{3}} = \frac{1}{\left(r_{\text{crit}}^{\text{SG}}\right)^{3}} + \frac{1}{\left(r_{\text{crit}}^{\text{AD}}\right)^{3}}\,, \tag{3.12}$$

where

$$\left(r_{\text{crit}}^{\text{SG}}\right)^{3} = \frac{3M\,[(k+1)^{2}+2]}{4\pi\rho}\,\frac{(1+\mu)^{3}}{(1+\mu^{3})}\,, \tag{3.13}$$

$$\left(r_{\text{crit}}^{\text{AD}}\right)^{3} = \frac{8GM\rho\,[(k+1)^{2}+2]}{9\gamma_{\text{S}}}\,\frac{\mu^{2}(1+\mu)^{2}}{(1+\mu^{3})}\,R^{3}\,. \tag{3.14}$$

Yet additional attractive forces can easily be implemented. It is important to mention, that the inclusion of adhesion allows for a size dependent critical distance to the planet expressed by Eq. (3.12). Equation (3.13) denotes the equilibrium distance, if mutual gravity is considered alone. It then depends only on the agglomerate proportions but does otherwise not imply any critical agglomerate sizes. Note, the critical distance, as well as the adhesive bond, does not depend on the mechanical properties of the grains.

Figure 3.2 illustrates r_{crit} in case of two radially-aligned, and synchronously rotating particles in contact. Results are given with respect to the Saturnian system, mass M_{S} and radius R_{S}, and material parameters of ice at low temperatures are applied as provided in Table 2.1. The critical range r_{crit} is sensitive to agglomerate sizes and clearly arises as an effective value of pure adhesive, Eq. (3.14), and gravitational particle interaction, Eq. (3.13). The asymptotic limit for large bodies coincides with the outer edge of the B ring for $\mu = 1$. It denotes the asymptotic value for larger bodies ($R \to \infty$) that are liable to gravity. In case of smaller grains ($R < 10$ m), adhesion dominates where $r_{\mathrm{crit}} \approx r_{\mathrm{crit}}^{\mathrm{AD}}$. As soon as smaller particles stick to larger ones ($\mu \ll 1$ or $\mu \gg 1$), these agglomerates are stable even as close to Saturn as the D ring. In the lower part of Fig. 3.2, the obvious symmetry with respect to μ is visible. Aggregates become unstable for $0.1 < \mu < 10$. The remaining parameter space refers to stable radially-aligned agglomerates.

In case of non-synchronously spinning aggregates ($k \neq 0$) centrifugal forces additionally tear at an adhesive bond. Figure 3.3 shows the influence of different spin configurations. Non-spinning aggregates ($\omega = 0$, $k = -1$) logically appear to be the most stable ones. Any rotation, clockwise or anti-clockwise, shifts r_{crit} farther outward. Only smaller aggregates can sustain themselves at high rotation rates.

Rotation rates of ring particles have been investigated in previous studies for non-gravitating particles (Salo, 1987), gravitating particles of identical size (Salo, 1995), and gravitating particles with size distribution (Ohtsuki, 2005), and revealed a decreasing spin rate with increasing particles size. Spin rates of moonlets embedded in planetary rings were discussed in (e.g. Morishima and Salo, 2004; Ohtsuki, 2004). It has further been shown, that not only the average rotation rate but also the spin dispersion is of major importance to the dynamics of rings. But implementing a spin dispersion $\sim 1/(R(1+\mu))$ (Salo, 1987) shows no significant influence on r_{crit}. Resulting variation in r_{crit} remain within $0.05 R_{\mathrm{S}}$.

Weidenschilling et al. (1984, pp. 376-377) gave expressions for the distance where the net attraction between two spherical, radially-aligned particles in contact is zero. They considered several cases as follows: equally sized bodies in synchronous rotation (their Eq. (2)) and not rotating (their Eq. (3)); a small particle resting on a larger one in synchronous rotation (their Eq. (4)) and not rotating (their Eq. (5)). Applying these parameters to Eq. (3.9), we find a good agreement with our results as shown in Fig. 3.4. Each thick horizontal line is denotes one particular set of parameters, which is reproduced as an asymptotic limit in case of large R.

Longaretti (1989) deduced a critical density in case of only gravitational attraction. He also noted that aggregates with $\mu \neq 1$ effectively attract each other, implying an indirect dependence of these findings on the radial distance. Much before the more recent studies, Roche (1847) investigated the existence of satellites around central bodies and derived the closest distance from a planet of radius R_{planet} and density ρ_{planet} at which a homogenous, self-gravitating liquid satellite of density $\rho_{\mathrm{satellite}}$ can exist in a circular orbit in synchronous rotation. This limit distance became known as the *Roche* limit given by

$$\frac{r_{Roche}}{R_{\mathrm{planet}}} = 2.456 \left(\frac{\rho_{\mathrm{planet}}}{\rho_{\mathrm{satellite}}} \right)^{1/3} \qquad (3.15)$$

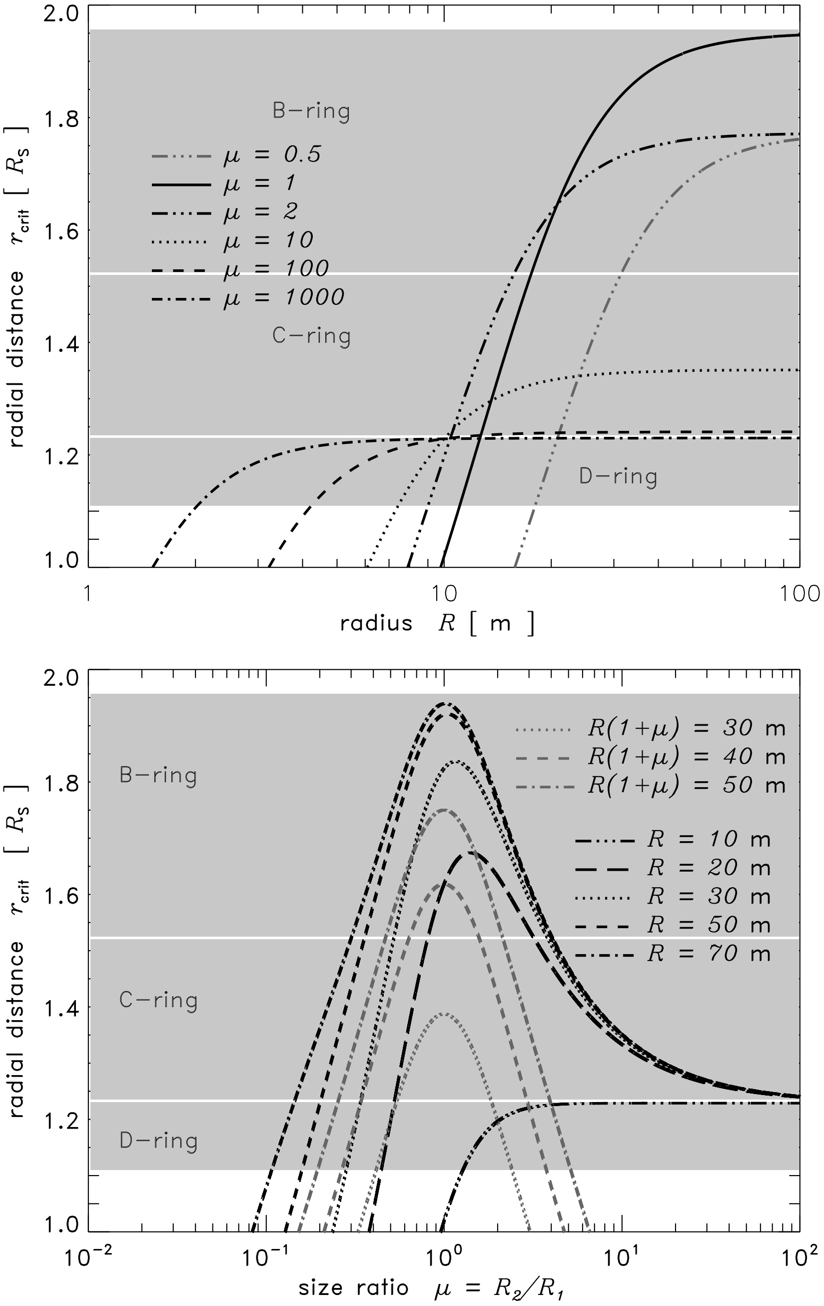

Figure 3.2: Stability region I: The critical distance r_{crit} in Saturnian radii R_{S} is illustrated for two radially-aligned ($\alpha = 0$), and synchronously rotating ($k = 0$) particles in contact of different proportions. Grey shaded regions denote certain rings as a reference. Either the proportion μ (upper) or the agglomerate or grain size R (lower) has been kept constant and the dependence on either of them is given for $\gamma_{\mathrm{S}} = 0.74$.

Not only the existence of satellites but also the onset of growth processes, limited by tidal stresses, is usually denoted by the *Roche* limit (Roche, 1847; Chandrasekhar, 1969). Since the Saturnian ring system mainly consists of icy particles ($\rho = 10^3$ kg m^{-3}), the corresponding classical *Roche* limit is located at 2.2 Saturn radii (mid A ring). However, as long as

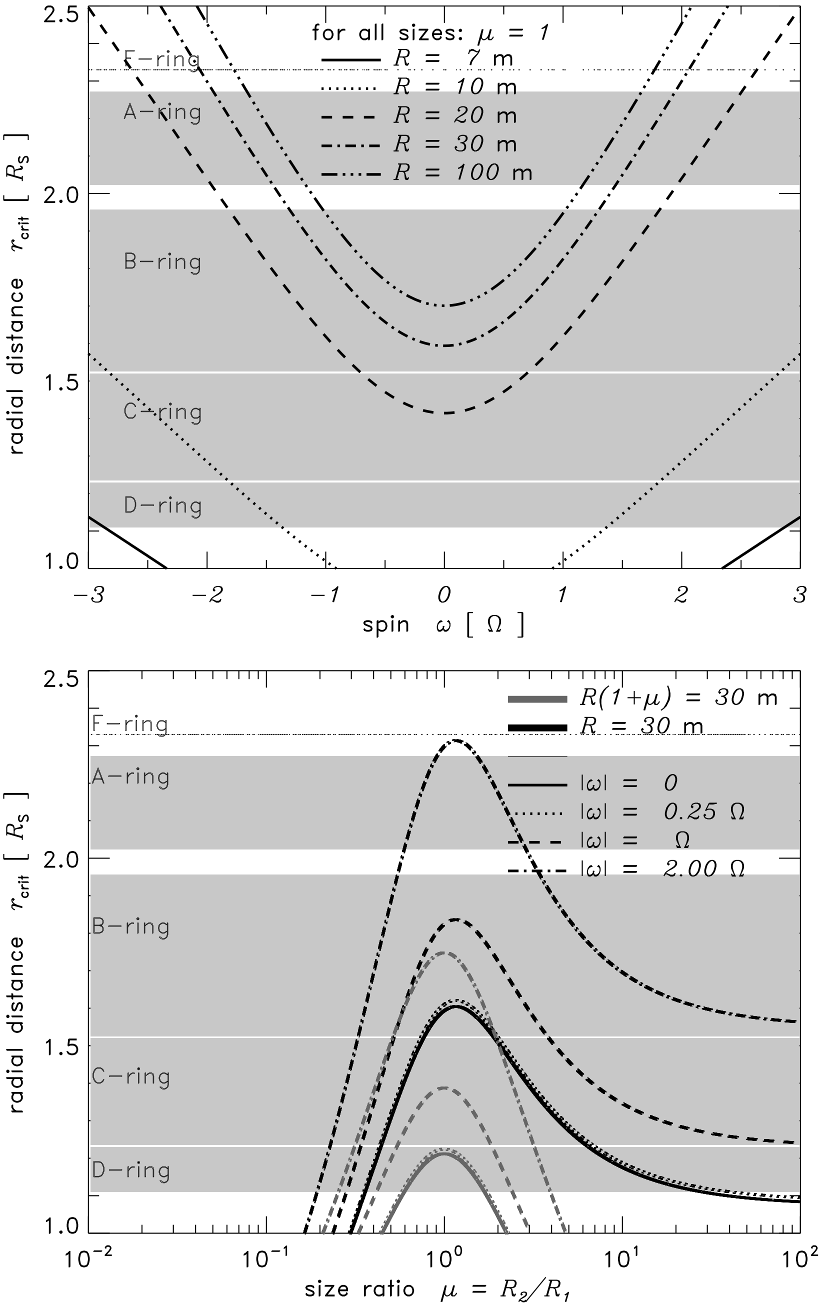

Figure 3.3: Stability region II: The critical distance $r_{\rm crit}$ in Saturn radii $R_{\rm S}$ is illustrated for different agglomerate spins $\omega = \dot{\alpha} + \Omega$. Values represent snapshots of radial alignment ($\alpha = 0$) and equal sizes ($\mu = 1$). Any spin of an agglomerate shifts $r_{\rm crit}$ farther outward. Non-rotating and aggregates ($\omega = 0, \dot{\alpha} = -\Omega$) reveal the closest equilibrium distance and are thus the most stable but also unlikely ones. $r_{\rm crit}$ is depending on $|\omega|$ only and is thus symmetric with respect to prograde and retrograde spins.

gravity is considered alone these criteria do only depend on the distance from the central planet and the size ratio of colliding grains (Weidenschilling et al., 1984; Ohtsuki, 1993) but not the total size of the agglomerate as it has also been observed by *Cassini*.

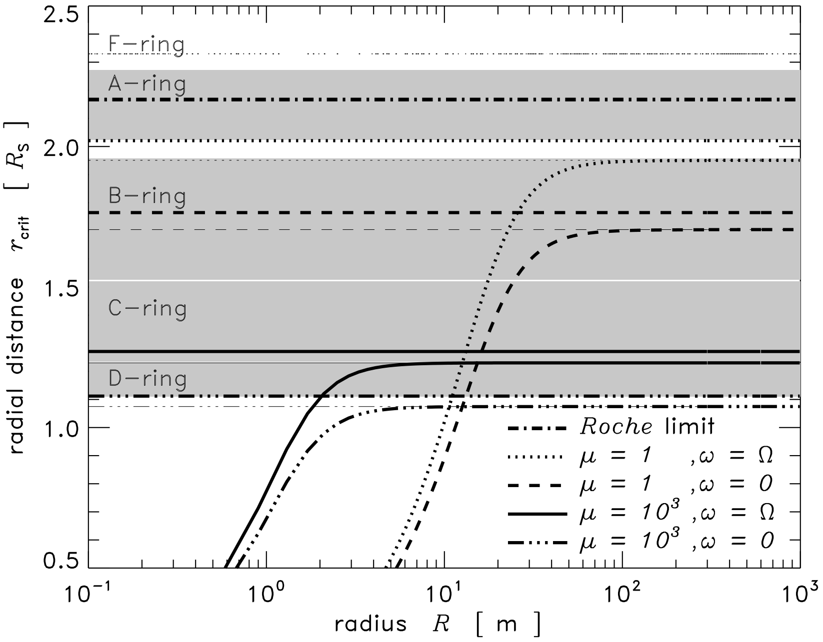

Figure 3.4: Comparisons: The critical distance $r_{\rm crit}$ is plotted for different parameter sets (μ, ω) each with $\alpha = 0$. Thicker and thinner horizontal lines refer to adaptive *Roche* limits presented in Weidenschilling et al. (1984) (dotted - their Eq. (2); dashed - their Eq. (3); solid - their Eq. (4); dashed-dotted - their Eq. (5)) and limits given by gravity only, respectively. These emerge as asymptotic values only and are not valid for all sizes. The critical distance is definitely size dependent. Saturn's rings are sketched as a reference where for $r_{\rm crit} \leq 1$ we find the planet itself.

However, stability seems to be highly pronounced compared to observations implying agglomerates of tens of meters in size. Hatzes et al. (1991) obtained maximum sizes for N-body agglomerates in a tidal regime of about $R = 6\,\mathrm{m}$ for 10 cm and $R = 70\,\mathrm{m}$ for 1 meter-sized spherical particles. But since no other perturbing or erosive processes, such as *e.g.* further collisions, have been considered, results presented here denote an upper limit of particle sizes for a given location. Including all these processes, grain sizes are expected to be much smaller as as adumbrated below.

3.1.2 Collisional Stability Estimate of Two-Body Agglomerates

As for the stability discussion in Sec. 3.1.1, a rough estimate for the effects of including erosive processes is presented in this section. To this aim, we check the bond strength (adhesive and gravitational) against the impact energy of yet another body. A sufficient break-up energy $E_{\rm break} = QM_{\rm coll}$ is required to ensure the destruction of the agglomerate, where Q denotes the critical specific energy per unit mass (Durda et al., 1998) and $M_{\rm coll} = 4\pi\rho R_{\rm coll}^3/3$ describes the mass of the impacting body with radius $R_{\rm coll}$. This critical specific energy accounts for the internal strength (elastic energy of deformation, number and strength of internal bonds between constituents, etc.) and the gravitational binding energy. The impact energy must exceed E_{break} to destroy the target.

Agglomerates discussed in this section are built in a rather simple way, because they contain only a single bond with a binding energy of $E_{\text{bond}} = E_{\text{ad}} + E_{\text{grav}}$. The adhesive energy[2] is then determined by

$$E_{\text{ad}} = \int_0^{\xi_{\text{ad}}} F_{\text{static}}(\xi)\mathrm{d}\xi = \frac{36}{7}\,(6\pi^5)^{1/3}\left[\frac{\gamma_S^5 R_{\text{eff}}^4}{E_{\text{eff}}^2}\right]^{1/3}\,, \tag{3.16}$$

where F_{static} and ξ_{ad} are given in Eq. (2.59) and (2.62), respectively. The gravitational potential reads $E_{\text{grav}} = G m_1 m_2 d^{-1}$. Although impact velocities can reach escape velocities of the largest ring boulders (Ohtsuki, 1993), $v_{\text{coll}} = 3d\Omega/2$ is assumed for simplicity. In doing so, we evaluate the influence of further collisions. Anyhow, higher-velocity impacts result in even more destructive encounters producing smaller debris. Our estimates denote upper limits. This is supposed to serve as an exemplary correction of results on stability obtained in the previous section.

In analogy to Sec. 3.1.1, r_{crit} emanates from Ω_{crit} and reads

$$r_{\text{crit}}^3 = \frac{9GM_S}{8}\frac{m_{\text{eff}}M_{\text{coll}}}{(E_{\text{ad}}+E_{\text{gr}})(m_{\text{eff}}+M_{\text{coll}})}\,. \tag{3.17}$$

Fig. 3.5 shows the limiting distance for agglomerates of equally sized constituents but different sizes of an impacting third body. We chose equally-sized constituents since they represent a limit case of least stable aggregates. The stability region is by far not as pronounced as in Sec. 3.1.1. Maximum sizes are within the range of decimeters for the inner rings, which is fairly close to *Voyager* and *Cassini* observations. Smaller agglomerates are not as easily broken as larger ones, since adhesive bonds are relatively stronger and tidal forces weaker (cf. previous sections). It implies that smaller particles reside closer to the planet than larger. This tendency is retained and again matches observations.

3.1.3 Summary

In terms of these analytical estimates, agglomerates are most fragile if they consist of equal sized particles. Small particles stick more easily to larger ones (indicated by a comparably high critical velocity, see also Fig. 2.8). Additionally, the stability zone for $\mu \neq 1$ (see Fig. 3.2) is definitely broader. For $\mu \approx 1$, particles are located outside, whereas smaller particles resting on a larger one, are well inside the *Hill*-sphere of the latter (Ohtsuki, 1993). Therefore, the agglomeration of smaller particles ($\mu \neq 1$) appears always possible, further promoting the existence of regolith layers. Their thickness will strongly depend on the size of the largest body of the agglomerate and thus indirectly on the radial distance from the central planet. Regolith layers, in turn, strongly determine the elasticity of further impacts. Hence, the average elasticity of a collision may not only be dependent on the impact speed but is also determined by the location within the rings.

---

[2] For reasons given above (cf. Sec. 2, in particular Sec. 2.4.2), details of the collision dynamics including the interparticle bond will be adopted according to the approximative description given in Sec. 2.3.1. Note, that the adhesive part of the static force is a potential force. The bond energy is thus different from the final snapping energy E_{snap}.

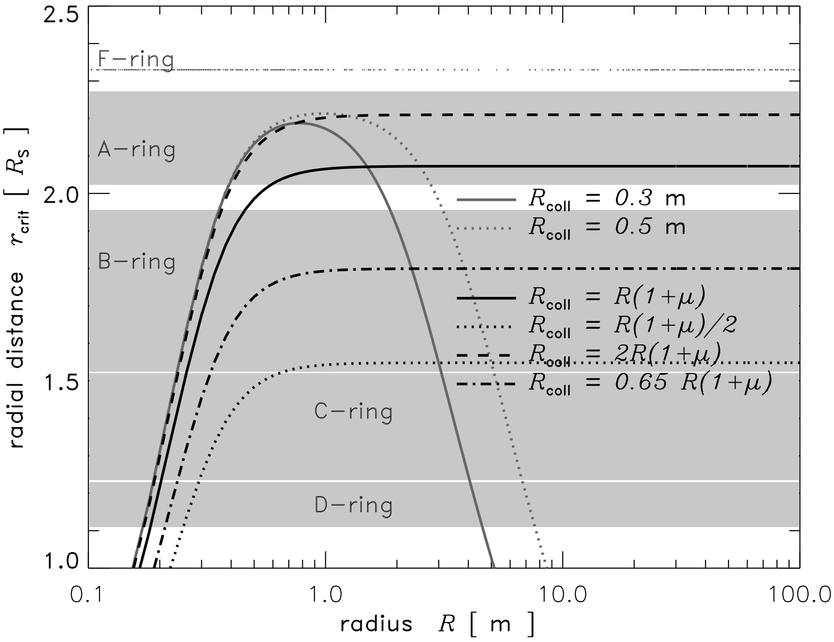

Figure 3.5: Collisional stability: The critical distance $r_{\rm crit}$ is plotted for an agglomerate ($\mu = 1$) impacted by a grain of radius $R_{\rm coll} = nR$, where $n \in [0.5,\ 0.65,\ 1.0,\ 2.0]$. Collisional erosive processes enormously limit the agglomerate sizes to a few decimeters in size.

Grain sizes are obviously mainly determined by collisions and not by tidal stresses (cf. Longaretti, 1989). Impact energies are underestimated leading to larger stable agglomerates than can be expected in reality. However, these estimates provide a rough upper limit for stability and as all calculations in Sec. 3.1.1 and 3.1.2 should just be taken as guidelines for further, more detailed studies.

3.2 Numerical Simulations

For a more precise analysis of the dynamics of Eqs. (3.4-3.7) we perform at least simple numerical studies. This allows to account for collision frequency and likelihood of a collision.

3.2.1 Orbital Motion and *Hill*'s Equations

The dynamics of two particles, m_1 and m_2, in a co-rotating frame is given by Eqs. (3.4-3.7). Here, the equations of motion describe the center of mass and the relative motion. Considered masses are by far smaller than the mass of the central body[3], here Saturn, $M_S \ll m_1, m_2$. *Hill*'s equations[4] (Hill, 1878) may be applied to almost circular orbits. This approach is usually applied to the restricted three-body problem and denotes a linearization of general equations, where a test particle is studied in a system of a secondary object orbiting the central body. The study of mutual collisions and gravitational scattering is much easier in the framework of these equations. A scattering matrix for a test particle under the gravitational influence of an embedded moon, has been obtained by the same approach (Spahn and

---

[3] However, presented analysis is valid for any central mass M.

[4] *Hill*'s equations were introduced to study the lunar orbit and denote a linearization of the otherwise nonlinear potential force of a central body $GM\vec{r}/r^3$.

Wiebicke, 1988; Spahn and Sremčević, 2000; Sremčević et al., 2002). Somewhat closer to this thesis, Ohtsuki (1993) investigated collision and capture probability for two particles in orbit about a central body based on the relative orbital motion.

Hill's equations are usually used to study the so called restricted three-body problem, i.e. the motion of a test particle m_2 in the central field M_S and field of the secondary body m_1 ($M_S >> m_1 >> m_2$). However, in this thesis we follow studies of Nakazawa and Ida (1988) and Ohtsuki (1993), where the *relative* motion of two particles ($m_1 \sim m_2$) is described in terms of *Hill*'s equations. As described in detail in Nakazawa and Ida (1988), *Hill*'s equation may be rewritten using Eq. (3.3) and yield in Cartesian coordinates, the center of mass motion with respect to the central body $\vec{r}_\mathrm{c} = (x_\mathrm{c}, y_\mathrm{c}, z_\mathrm{c})$

$$\begin{aligned} \ddot{x}_\mathrm{c} &= +2\,\Omega_\mathrm{c}\,\dot{y}_\mathrm{c} + 3\,\Omega_\mathrm{c}^2\,x_\mathrm{c} \\ \ddot{y}_\mathrm{c} &= -2\,\Omega_\mathrm{c}\,\dot{x}_\mathrm{c} \\ \ddot{z}_\mathrm{c} &= \qquad\qquad - \;\Omega_\mathrm{c}^2\,z_\mathrm{c} \end{aligned} \tag{3.18}$$

and the relative motion $\vec{d} = (x, y, z)$

$$\begin{aligned} \ddot{x} &= +2\,\Omega_\mathrm{c}\,\dot{y} + 3\,\Omega_\mathrm{c}^2\,x - \frac{\nu}{r^3}x \\ \ddot{y} &= -2\,\Omega_\mathrm{c}\,\dot{x} \qquad\quad - \frac{\nu}{r^3}y \\ \ddot{z} &= \qquad\qquad - \;\Omega_\mathrm{c}^2\,z - \frac{\nu}{r^3}z \end{aligned} \tag{3.19}$$

where ν is given by

$$\nu = \frac{m_1 + m_2}{M_\mathrm{S}}\,a_\mathrm{c}^3\,\Omega_\mathrm{c}^3\,, \tag{3.20}$$

and a_c and Ω_c denote the semimajor axis and orbit frequency of the center of mass, respectively. The system is naturally described in a non-dimensional form where time and distance are normalized by Ω_c^{-1} and $a_\mathrm{c}h$,

$$\tilde{t} = t\,\Omega_\mathrm{c} \tag{3.21}$$

$$\vec{\tilde{d}} = (\tilde{x}, \tilde{y}, \tilde{z}) = \frac{(x, y, z)}{a_\mathrm{c}\,h}\,, \tag{3.22}$$

and h denotes the reduced *Hill* radius of the two grains defined by

$$h = \left(\frac{m_1 + m_2}{3M_\mathrm{S}}\right)^{1/3}\,. \tag{3.23}$$

Rescaling Eqs. (3.19) as introduced in Eqs. (3.21) and (3.22), the relative motion may be expressed as

$$\begin{aligned} \ddot{\tilde{x}} &= +2\,\Omega_\mathrm{c}\,\dot{\tilde{y}} + 3\,\Omega_\mathrm{c}^2\,\tilde{x} - \frac{\tilde{x}}{r^3} \\ \ddot{\tilde{y}} &= -2\,\Omega_\mathrm{c}\,\dot{\tilde{x}} \qquad\quad - \frac{\tilde{y}}{r^3} \\ \ddot{\tilde{z}} &= \qquad\qquad - \;\Omega_\mathrm{c}^2\,\tilde{z} - \frac{\tilde{z}}{r^3}\,. \end{aligned} \tag{3.24}$$

If the relative distance $\tilde{d}$ between both particles is sufficiently large, the mutual interaction term can be neglected and the system of equations (Eq. (3.24)) describes a *Keplerian* motion with the analytical solution (Petit and Henon, 1987)

$$\begin{aligned}\tilde{x}(\tilde{t}) &= \tilde{b}-\tilde{e}\cos(\tilde{t}-\tau)\\ \tilde{y}(\tilde{t}) &= -\frac{3}{2}\tilde{b}(\tilde{t}-\phi)+2\tilde{e}\sin(\tilde{t}-\tau)\\ \tilde{z}(\tilde{t}) &= \tilde{\imath}\sin(\tilde{t}-\omega)\ , \end{aligned} \tag{3.25}$$

where the set of equivalent *Keplerian* orbital elements of *relative* motion reads: $\tilde{b}$ semimajor axis (here also denoting the impact parameter), $\tilde{e}$ eccentricity, $\tilde{\imath}$ inclination, τ longitude of perihelion, ω longitude of ascending node, and ϕ time of pericenter passage. The first three shape the orbit and are defined in terms of orbital elements of masses m_1 and m_2 as

$$\begin{aligned}\tilde{b} &= \frac{b}{a_c h} = \frac{b_1-b_2}{a_c h}\\ \tilde{e} &= \frac{e}{h} = \frac{1}{h}\left[e_1^2+e_2^2-2e_1e_2\cos(\tau_2-\tau_1)\right]\\ \tilde{\imath} &= \frac{i}{h} = \frac{1}{h}\left[i_1^2+i_2^2-2i_1i_2\sin(\omega_2-\omega_1)\right]\ . \end{aligned} \tag{3.26}$$

Note that even if $e_1 \neq 0$ and $e_2 \neq 0$ the resulting eccentricity $\tilde{e}$ can be zero. The latter three are angular orbital elements determining orientation of and position on the relative orbit.

3.2.2 Binary Particle Collisions

In planetary rings particle collisions are an essential component of rings' dynamics and occur several times per orbit. As demonstrated in Sec. 2 and applied in Sec. 3.1, collisions happen almost instantaneously compared to the timescale of orbital motion. Thus, only the outcome of the collision and therefore the coefficient of restitution is important for a further dynamical evolution. A collision model as introduced in Sec. 2 can be applied straight away. To outline this task one has firstly to detect a collision and secondly to "correct" the rebound velocity for ε_N.

As an initial orbital setup, the masses, m_1 and m_2, may be placed at a sufficiently large relative azimuthal distance where their gravitational interaction is negligible. Fixing the relative orbital elements ($\tilde{b}$, $\tilde{e}$, $\tilde{\imath}$, τ , ω , ϕ) the set of Eq. (3.25) is applied to obtain corresponding initial Cartesian coordinates at $\tilde{t} = 0$. For simplicity, ϕ is not directly chosen in numerical simulations. Instead we use an azimuthal, Cartesian distance referred to as $\tilde{y}_{\max}$. It ensures a sufficiently large relative distance and is defined as $\tilde{y}_{\max} = \max[\,40,\ 20\tilde{e}\,]$ (Ida and Nakazawa, 1989; Ohtsuki, 1993). Due to their mutual gravity grains attract each other and in case they do not collide are at least scattered. Any scattering, geometrical or physical, changes the grain's velocity and the velocity distribution. Therefore, effects of self-gravity are crucial as has been shown in various studies (Salo et al., 2004; Lewis and Stewart, 2005).

In order to illustrate the relative motion, Fig. 3.6 shows trajectories obtained by Eq. (3.24) where $\tilde{b} = 1.79$, $\tilde{e} = 0$, $\tilde{\imath} = 0$, $\tau = 0$, $\omega = 0$, $\tilde{y}_{\max} = 40$, and $r_p = 0.97$ are applied as initial conditions. The gray area ($\tilde{x}^{\,2}+\tilde{y}^{\,2}+\tilde{z}^{\,2} < 1$) describes the effective target of relative motion. An impact can be illustrated as a point mass hitting a second particle of radius $R_1 + R_2$ instead of two separate grains approaching each other. Identical initial conditions but different coefficients of restitution[5] are chosen. Note, since the same initial conditions are applied in all cases, the incoming trajectory is always the same and enters the plot at the top. However, rebound trajectories differ and are denoted as solid, dashed-dotted, and dotted lines. For $\varepsilon_N = 1$ no energy is dissipated (solid line). Reducing the value of ε_N clearly diminishes the relative distance after impact, since the rebound velocity is smaller (dashed-dotted line). Yet further increasing dissipation decreases the separation speed such that the trajectory is completely changed by mutual gravity.

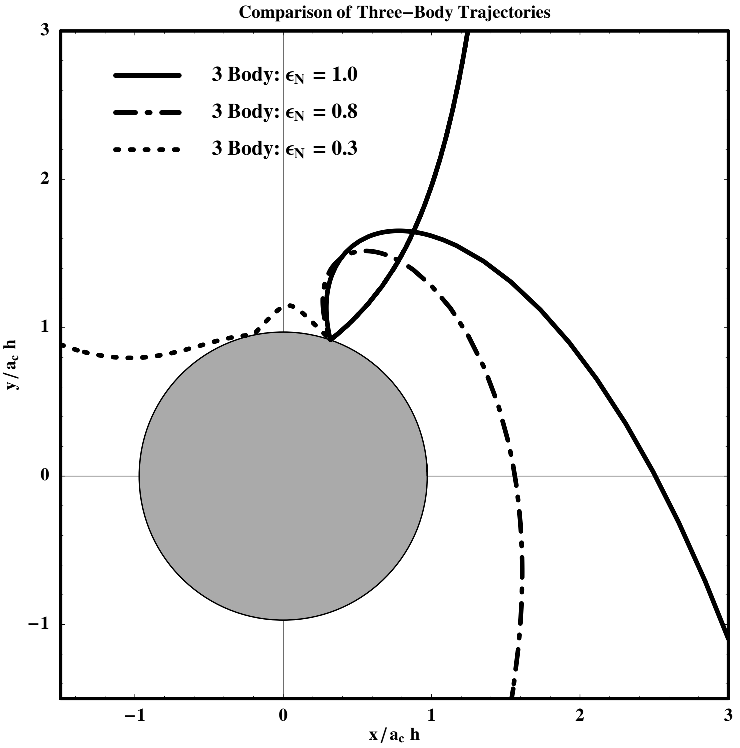

Figure 3.6: Comparison of different trajectories corresponding to different ε_N are obtained by solving Eq. (3.24) using the same initial conditions: $\tilde{b} = 1.79$, $\tilde{e} = 0$, $\tilde{i} = 0$, $\tau = 0$, $\omega = 0$, $\tilde{y}_{\max} = 40$, $r_p = 0.97$. The more dissipative the impact the more important mutual gravity becomes to the ongoing relative motion. Note, results are shown in units of their *Hill* scaling and the gray area denotes the target of effective size $R_1 + R_2$.

3.2.3 Capture Probability

Since we are not primarily interested in details of orbital motion but in the overall influence of collision dynamics, it is sufficient to concentrate on values such as collision and capture probability. Despite the investigation of special cases it is more interesting to obtain results with respect to an entire grain ensemble. Therefore, it is necessary to implement the distribution of orbital elements while preparing sets of initial conditions. The angular orbital elements (τ, ω) are drawn uniformly within $\tau \in [0, 2\pi]$ and $\omega \in [0, \pi]$. The third angular orbital element ϕ should only ensure a sufficiently large initial distance between the grains

---

[5] Since the description in terms of *Hill*'s equations does not include the spin of particles, the tangential coefficient of restitution ε_T can safely be put to unity.

as mentioned before. Semimajor axis $\tilde{b}$, or impact parameter, as well as eccentricity and inclination are discussed below.

In general, particles collide more than once and, correspondingly to that, the trajectory is very complex and chaotic (Petit and Hénon, 1986). Following Ohtsuki (1993) we use the *Jacobi* constant

$$E_{\mathrm{J}} = \frac{1}{2}(\dot{\tilde{x}}^{2}+\dot{\tilde{y}}^{2}+\dot{\tilde{z}}^{2})+U(\tilde{x},\tilde{y},\tilde{z}) \, , \tag{3.27}$$

where

$$U(\tilde{x},\tilde{y},\tilde{z}) = -\frac{3}{2}\tilde{x}^{2}+\frac{1}{2}\tilde{z}^{2}-\frac{3}{\tilde{r}}+\frac{9}{2} \, , \tag{3.28}$$

which is the integral of motion (energy integral) of Hill's equations valid between two collisions. The *Jacobi* integral can also be expressed in terms of the relative orbital elements as (Ohtsuki, 1993)

$$E_{\mathrm{J}} = \frac{1}{2}(\tilde{e}^{2}+\tilde{\imath}^{2})-\frac{3}{8}\tilde{b}^{2}-\frac{3}{\tilde{r}}+\frac{9}{2} \, . \tag{3.29}$$

The additive constant $9/2$ of the energy integral is chosen in such a way that $U = 0$ at the Hill's sphere border. Therefore in order to save CPU time, we can use the following criterion for the capture $E_{\mathrm{J}} < 0$, evaluated *after* each collision, as particle cannot escape the potential well. Additionally, if particles stick together an adhesive bond, Eq. (2.30). If this bond is found to be stronger than disruptive inertia forces, grains will be captured.

The impact parameter $\tilde{b}$ may be chosen with respect to the likeliest collision orbits of two grains. We choose $\tilde{b}_{\mathrm{min}} \leq \tilde{b} \leq \tilde{b}_{\mathrm{max}}$ where $\tilde{b}_{\mathrm{min}} = 8/(2.5+2\tilde{e})$ and $\tilde{b}_{\mathrm{max}} = (12+4(\tilde{e}^{2}+\tilde{\imath}^{2})/3)^{1/2}$ as was used in comparable studies (Ida and Nakazawa, 1989). This helps to save CPU time, while concentrating on actual collision orbits. Two additional orbital elements, $\tilde{e}$ and $\tilde{\imath}$, remain to be fixed.

Eccentricity and inclination determine the relative orbital velocity as $\tilde{v}^{2} = \tilde{e}^{2}+\tilde{\imath}^{2}$ (Ohtsuki, 1993) and thus effectively correspond to the granular temperature of the ensemble. The two-body escape velocity v_{esc} reads

$$v_{\mathrm{esc}} = \sqrt{\frac{2G(m_1+m_2)}{R_1+R_2}} = \sqrt{\frac{6}{r_{\mathrm{p}}}} \, , \tag{3.30}$$

where r_{p} denotes the scaled sum of particle radii as

$$r_{\mathrm{p}} = \frac{R_1+R_2}{a_{\mathrm{c}}h} = \left(\frac{9M_{\mathrm{S}}}{4\pi\rho}\right)^{1/3}\cdot\frac{1}{a_{\mathrm{c}}}\cdot\frac{(R_1+R_2)}{(R_1^3+R_2^3)^{1/3}} \, , \tag{3.31}$$

with a_{c} being the semimajor axis of the center of mass. In case of equal sized particles ($\mu = 1$), and thus $R_1 = R_2$, neither r_{p} nor a_{c} are dependent on the size of the individual particles and both are inversely proportional to each other $r_{\mathrm{p}} \sim 1/a_{\mathrm{c}}$. Additionally, rewriting Eq. (3.31) yields

$$r_{\mathrm{p}} = \left(\frac{9M_{\mathrm{S}}}{4\pi\rho}\right)^{1/3}\cdot\frac{1}{a_{\mathrm{c}}}\cdot\frac{1+\mu}{(1+\mu^3)^{1/3}} \, , \tag{3.32}$$

clearly independent of the actual grain size. As characteristic for gravity, only the size ratio μ matters. Choosing a value of r_p clearly fixes a particular application where then only an initial velocity has to be adjusted. Examples of possible applications are given in Table 3.1 (cf. Ohtsuki, 1993, Table 1). In case of collisions, r_p does further denote the scaled minimal distance two particles can have.

Central Body	Orbit Location	$\mu = 0.1$	$\mu = 1$	$\mu = 10$	$\mu = 100$
Sun	Saturn	0.9×10^{-3}	1.2×10^{-3}	0.9×10^{-3}	0.8×10^{-3}
	Jupiter	1.6×10^{-3}	2.3×10^{-3}	1.6×10^{-3}	1.5×10^{-3}
	Earth	8.3×10^{-3}	1.2×10^{-3}	0.8×10^{-3}	7.6×10^{-3}
Saturn	Titan	0.06	0.1	0.07	0.06
	Enceladus	0.35	0.5	0.3	0.3
	$1.5\,R_\mathrm{S}$	0.9	1.3	0.9	0.9
	$2.0\,R_\mathrm{S}$	0.7	1.0	0.7	0.6
	$2.3\,R_\mathrm{S}$	0.6	0.9	0.6	0.5

Table 3.1: Values of r_p for different regions of interest. Choosing a particle size ratio μ additionally to central mass, here M_S, and semimajor axis a_c clearly determines the application. Examples are given with respect to Saturn's rings and other systems (cf. Ohtsuki, 1993, Table 1) where a density of $\rho = 10^3\,\mathrm{kg\,m^{-3}}$ is applied. The main rings of Saturn cover a parameter range of roughly $r_\mathrm{p} \in [0.5, 1.5]$.

With a set of independently chosen initial parameters $(\tilde{b}, \tilde{e}, \tilde{\imath}, \tau, \omega)$, collision p_coll and capture counters p_capt can be defined as (Ohtsuki, 1993)

$$p_\mathrm{coll}(\tilde{b}, \tilde{e}, \tilde{\imath}, \tau, \omega) = \begin{cases} 1 & \text{if particles collide} \\ 0 & \text{otherwise} \end{cases} \tag{3.33}$$

and

$$p_\mathrm{capt}(\tilde{b}, \tilde{e}, \tilde{\imath}, \tau, \omega) = \begin{cases} 1 & \text{if \textit{Jacobian} integral is negative after impact} \\ 0 & \text{otherwise} \end{cases} . \tag{3.34}$$

Basically, simply counting all positive events is sufficient in order to obtain the according probabilities. This is correct if the initial variables are uniformly distributed. However, the distribution of the impact parameter $\tilde{b}$ and especially the distributions of eccentricities $\tilde{e}$ and inclinations $\tilde{\imath}$ are not uniform. Leaving $\tilde{e}$ and $\tilde{\imath}$ aside, the corresponding equations for collision $C_\mathrm{coll}(\tilde{e}, \tilde{\imath})$ and capture rate $C_\mathrm{capt}(\tilde{e}, \tilde{\imath})$ read (Nakazawa et al., 1989; Ida and Nakazawa, 1989)

$$C_\mathrm{coll}(\tilde{e}, \tilde{\imath}) = \int\limits_{\tilde{b}_\mathrm{min}}^{\tilde{b}_\mathrm{max}} \mathrm{d}\tilde{b} \int\limits_0^{2\pi} \mathrm{d}\tau \int\limits_0^{\pi} \mathrm{d}\omega \, \frac{3}{2} |\tilde{b}| (2\pi)^{-2} \, p_\mathrm{coll}(\tilde{b}, \tilde{e}, \tilde{\imath}, \tau, \omega) \tag{3.35}$$

and

$$C_\mathrm{capt}(\tilde{e}, \tilde{\imath}) = \int\limits_{\tilde{b}_\mathrm{min}}^{\tilde{b}_\mathrm{max}} \mathrm{d}\tilde{b} \int\limits_0^{2\pi} \mathrm{d}\tau \int\limits_0^{\pi} \mathrm{d}\omega \, \frac{3}{2} |\tilde{b}| (2\pi)^{-2} \, p_\mathrm{capt}(\tilde{b}, \tilde{e}, \tilde{\imath}, \tau, \omega) \, . \tag{3.36}$$

Only colliding grains may capture each other and the capture probability P_{capt} is a conditional probability expressed as

$$P_{\mathrm{capt}}(\tilde{e},\tilde{\imath}) = \frac{C_{\mathrm{capt}}}{C_{\mathrm{coll}}} . \tag{3.37}$$

At this point we will follow two exemplary applications given in Ohtsuki (1993), namely for $r_{\mathrm{p}} = 0.008$, i.e. collisions between planetesimals in heliocentric orbits of $a_{\mathrm{c}} = 1$ AU, and $r_{\mathrm{p}} = 0.1$. The capture probability is obtained as a function of relative velocity $\tilde{v}$ as illustrated in Fig. 3.7. Eccentricity $\tilde{e}$ and inclination $\tilde{\imath}$ are chosen to match relative velocities $\tilde{v}$ while $\tilde{b}$, τ, and ω are drawn uniformly. In contrast to Ohtsuki (1993), who employed extensive numerical calculations by splitting the parameter space into a grid and laboriously scanning for collision orbits, a *Monte-Carlo* approach is employed in our study. It allows for a good statistical representation of results with fewer collisions. Simulation results are presented in Fig. 3.7. Each data point is obtained by averaging over 1000 collisions. A fair agreement of both methods is reached as demonstrated in Fig. 3.7 for both $\varepsilon_{\mathrm{N}} = 0.9$ and $\varepsilon_{\mathrm{N}} = 0.5$.

Instead of fixing the coefficient of restitution ε_{N} to a constant value as done by most authors, the collision model presented in Chapter 2 is applied. Since Eq. (2.61) does not only depend on the size ratio μ of both grains but on their actual size R as well, an additional parameter, not covered by (Ohtsuki, 1993), is introduced. Additionally, the possibility of aggregation raises questions whether cohesive forces overall increase the capture probability. Therefore, whenever a collision is detected, Eq. (2.61) is applied to obtain the appropriate restitution coefficient. The normal rebound velocity is then calculated accordingly while the tangential restitution is fixed to $\varepsilon_{\mathrm{T}} = 1$ at all times. As mentioned above, we define a capture, if the *Jacobian* integral (Eq. (3.29) is less than zero *after* impact, and stop the simulation. If the normal impact speed is sufficiently low, grains will form a sticking bond ($\varepsilon_{\mathrm{N}} = 0$) according to Chapter 2. This bond is given by Eq. (2.30) and may prevent a post-collisional separation. In our numerical study it became evident, that the majority of sticking contacts leads to capture.

Another effect is found in case of small impact speeds: during repetitive collisions sliding motion may occur, especially if $\varepsilon_{\mathrm{T}} = 1$. In particular, the likelihood of such sliding is increased due to a vanishing normal restitution coefficient for relatively small impact speeds. Comparable studies noticed this effect as well, as it causes numerical difficulties (Petit and Henon, 1987; Wisdom and Tremaine, 1988; Ohtsuki, 1993). In the present numerical study, the motion of particles in contact is covered in terms of spherical coordinates while keeping $r = R_1 + R_2$ as long as the attractive bond according, Eq. (2.30), is stronger than disruptive inertia forces. At this point of contact, the relative motion is restricted to $r = const$ and the remaining two angular degrees of freedom are solved using *Hill*'s equation in spherical coordinates. This rolling motion is traced unless it continues for more than 2π. If so, we additionally define a capture event. Friction naturally restricts the sliding phase.

In order to quantify these result more precisely and also to be able to directly compare to results of Sec. 3.1, the orbit dynamics will be applied directly to the Saturnian system in the next section.

3.2.4 Applications to Saturn's Rings

In order to study planetary rings and to obtain capture probabilities, we randomly choose the initial orbital elements as before, since this approach allows for less extensive simulations.

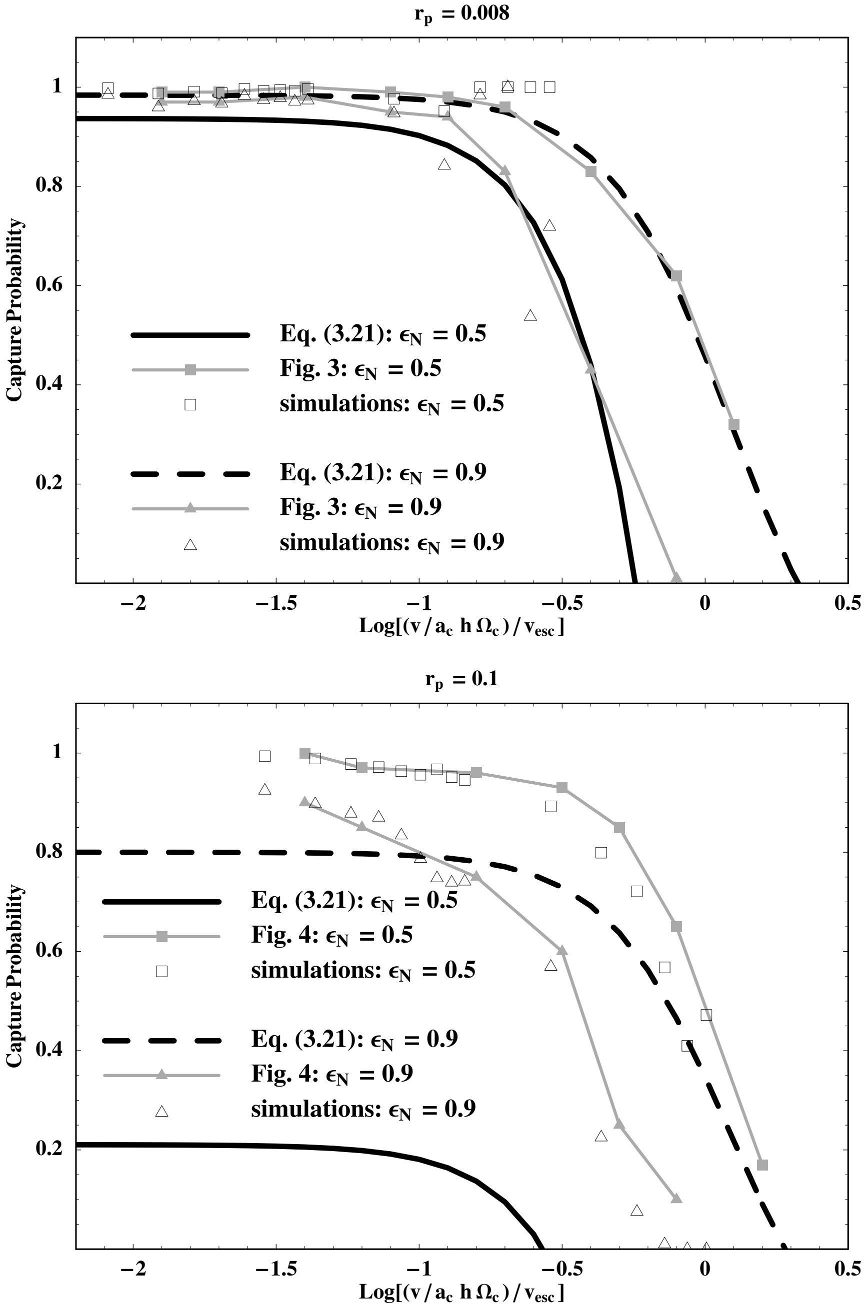

Figure 3.7: Capture probability of two grains in orbit around a central body as a function of scaled orbital velocity $\tilde{v}/v_{\rm esc}$. Integrations were done for $r_{\rm p} = 0.008$ and $r_{\rm p} = 0.1$ in direct comparison to Ohtsuki (1993, Eq. (3.21), Fig. 3 and Fig. 4). Simulations are in good agreement with his results. *Upper part:* Higher relative velocities cause captures to be less probable for $\varepsilon_{\rm N} = 0.9$ than for $\varepsilon_{\rm N} = 0.5$, where the capture probability is overall increased due to a higher dissipation during collisions. An analytical expression may be found in Ohtsuki (1993, Eq. (3.21)). Numerical results match the analytic expression quite well. *Lower part:* The general behavior of $C_{\rm capt}$ remains. However, the analytics does not match numerics anymore since it has been obtained in the limit of high velocity collisions ($r_{\rm p} \ll 1$).

For a direct application to a particular system, it is essential to choose an appropriate velocity distribution. While angular orbital elements remain uniformly distributed, eccentricities and inclinations have to be properly weighted.

Various authors studied this problem (Petit and Henon, 1987; Ida and Makino, 1992; Lissauer, 1993; Ohtsuki and Emori, 2000) and found that eccentricities $\tilde{e}$ and inclinations $\tilde{\imath}$ obey *Rayleigh* distributions

$$f(\tilde{e},\tilde{\imath}) \;=\; \frac{2\tilde{e}}{\tilde{e}_0^2}\exp\left[-\frac{\tilde{e}^{\,2}}{\tilde{e}_0^2}\right]\cdot\frac{2\tilde{\imath}}{\tilde{\imath}_0^2}\exp\left[-\frac{\tilde{\imath}^{\,2}}{\tilde{\imath}_0^2}\right] . \tag{3.38}$$

The velocity distribution $f(\tilde{e},\tilde{\imath})$ is normalized and parameters $\tilde{e}_0$ and $\tilde{\imath}_0$ denote the root mean square values $\tilde{e}_0^2 = \langle\tilde{e}^{\,2}\rangle$ and $\tilde{\imath}_0^2 = \langle\tilde{\imath}^{\,2}\rangle$, respectively. The ratio of $\tilde{e}_0^2$ to $\tilde{\imath}_0^2$ is found to vary from 1 to about 2 in different problems. Since it apparently plays no significant role (Sremčević et al., 2002) this value will be fixed to 2 in accordance with Ohtsuki (1993). Thus, the velocity dispersion is determined by either the eccentricity or inclination alone. Let us concentrate on eccentricities $\tilde{e}$ where the root mean square value reads

$$\tilde{e}_0 \;=\; 2\,\tilde{\imath}_0 = \frac{1}{\sqrt{2}}\frac{c_0}{a_\mathrm{c}\Omega_\mathrm{c}} . \tag{3.39}$$

A single parameter c_0 thus characterizes average orbital velocities and thus the velocity dispersion. In further numerical calculation values of c_0 in the range of $\mathrm{mm\,s^{-1}}$ to $\mathrm{cm\,s^{-1}}$ are applied. Random scaled eccentricities $\tilde{e}$ and inclinations $\tilde{\imath}$, are drawn according to the distribution, Eq. (3.38). Since $\tilde{e}$ and $\tilde{\imath}$ are properly chosen there is no need for further corrections of P_capt. Thus, Eqs. (3.35) and (3.36) provide collision and capture rates resulting in capture probability according to Eq. (3.37).

Covering Saturn's main rings in the range of $r \in [1.6, 2.5]\; R_\mathrm{S}$, particle sizes and size ratios appropriate for Saturn's rings are used. In contrast to Sec. 3.2.3 and Fig. 3.7, where only 1000 collisions per data point were calculated, 5000 collisions are simulated to increase the accuracy of P_capt. First, a constant restitution coefficient of $\varepsilon_\mathrm{N} = 0.3$ is applied, for simplicity, denoting the rough average of the velocity dependent restitution of viscoelastic grains (cf. Chapter 2) also found in experiments. Note, that in this first numerical experiment adhesion is not taken into account. The capture probability is this case is only determined by gravity and dissipation as particle interactions. The size ratio μ is fixed to 1, $c_0 = 0.002\ \mathrm{m\,s^{-1}}$ and the particle sizes vary from 0.1 to 1 m. Establishing a grid of 15×15 data points corresponding to 5000 collisions each, we obtained results presented in Fig. 3.8, where a radial pattern emerges. The capture probability increases with increasing distance. No variation of P_capt with respect to the particle size is visible. Thus, the capture probability depends on radial distance only. Below 1.8 R_S (B to C ring region) capture probability effectively reaches zero. The maximum values of P_capt in this setup are found beyond the F ring and take values of $P_\mathrm{capt} \approx 0.35$. The capture probability of equally sized grains does not exceed 30% throughout the main rings.

The radial pattern in Fig. 3.8 coincides with considerations on agglomerate stability accounting for gravitational interactions only (cf. Sec. 3.1). The general behavior is thus the same as for the limit case of larger bodies of Eq. (3.9) which is illustrated in a direct comparison to Weidenschilling et al. (1984) in Fig. 3.4. These findings generally agree with the idea of the *Roche* limit. Neither the stability criterion nor the numerically obtained capture probability show a particle size dependence! The capture probability may only generally

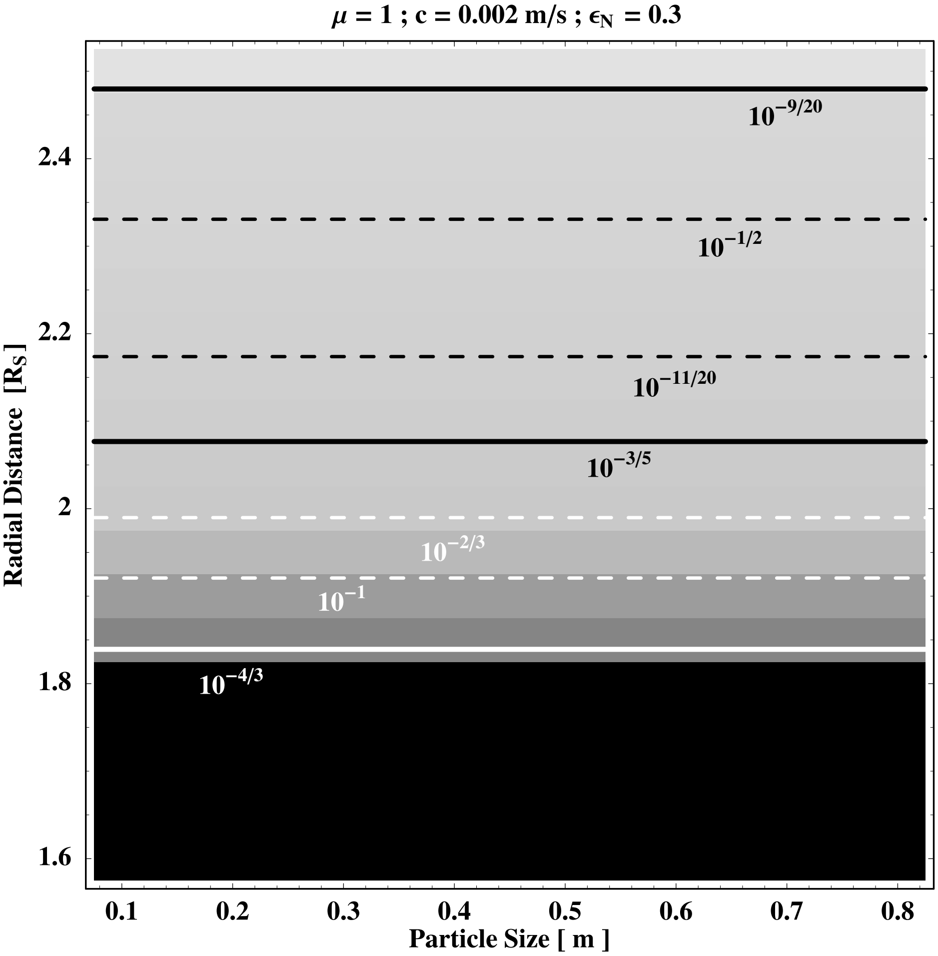

Figure 3.8: Logarithmic capture probability C_{capt} as a function of radial distance and particle size for a constant coefficient of restitution $\varepsilon_N = 0.3$. Clearly, a radial pattern of increasing C_{capt} emerges. Capture is more probable at farther distances. This is an expected finding since gravitational influences of the central body become weaker. The plot consists of 15 × 15 data points of C_{capt} averaged over 5000 simulated collisions each. Capture probability does not exceed 30% throughout the main rings. For distances closer to Saturn than 1.8 R_S the capture probability effectively reaches zero.

be increased by further reducing the coefficient of restitution. Ohtsuki (1993) expects no accretion at all within Saturn's rings if no cohesive forces besides gravity are considered. Weidenschilling et al. (1984) argues that accretion is at least possible for smaller particles being captured by larger ones. In that case r_p is smaller than unity and $\mu \neq 1$. Next, we demonstrate how sensitive adhesion modifies this picture.

Applying the collision model of adhesive, viscoelastic spheres (cf. Chapter 2) as described in Sec. 3.2.3 yields a completely different result. Figure 3.9 shows the logarithmic capture probability obtained by *Monte-Carlo* simulations in analogy to those presented in Fig. 3.8. The average capture probability is smaller than for a constant restitution. However, accretion is generally possible as close to Saturn as 1.6 R_S for particles up to 0.5 m in radius indicated by $P_{\text{capt}} > 0$. The particle size dependence coincides with the main outline given

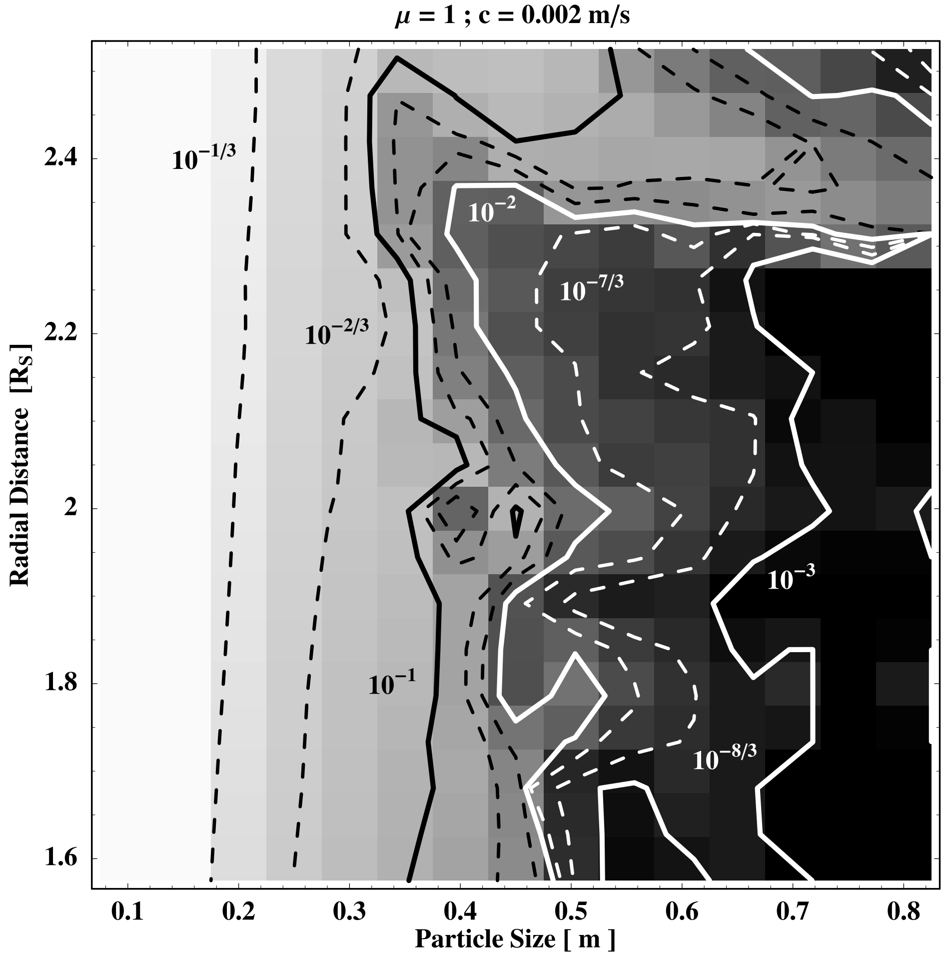

Figure 3.9: Logarithmic capture probability as a function or radial distance and particle size for ε_N as provided by Eq. (2.61). The plot resolution is the same as in Fig. 3.8. In contrast to a constant restitution coefficient the possibility of agglomeration allows for a particle size dependence as already found in Sec. 3.1. Capture in general is possible throughout the main rings. However, particular features raise additional questions of naturally preferred regions in tidal environments.

in Sec. 3.1. The capture probability as well as agglomerate stability are certainly dependent on grain size and not only on the size ratio.

For yet smaller particles than 0.1 m capture probability reaches unity regardless of the distance to the central planet. Larger grains than a meter in size show a minimal capture probability. However, additional cohesive forces do not simply increase the apparent capture probability. Both, an increase and decrease of P_{capt} can be found giving rise to interesting patterns further to be examined. This crucial difference clearly indicates the importance of including cohesive forces while considering planetary ring dynamics. Although the *Roche* zone for ice is located within the A ring at about 2.2 R_S, accretion is possible in the inner rings if adhesive forces are taken into account. An upper critical grain size may be inferred denoting the upper limit of the size distribution as a function of radial distance.

Increasing the average velocity by an order of magnitude to $c_0 = 0.02$ m s^{-1} surprisingly

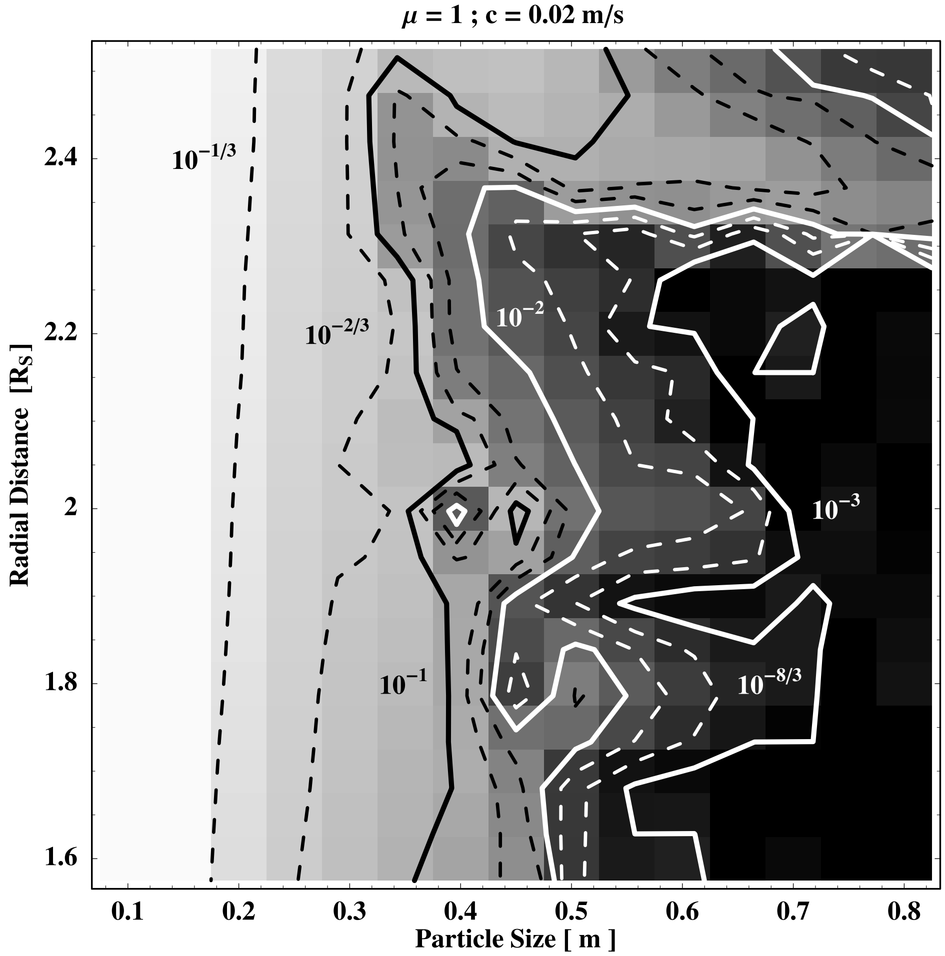

Figure 3.10: Logarithmic capture probability in analogy to Fig. 3.9 while in this case the average ensemble temperature is higher since $c_0 = 0.02$ m s^{-1}. The same gray levels as in Fig. 3.9 has been applied for an easier comparison. The general impression remains the same although particular feature are more pronounced then for $c_0 = 0.002$ m s^{-1}. Certain ring regions seem to preferably allow for aggregation. Note, these results are based on collision dynamics and mutual gravity only.

yields nearly the same results as in Fig. 3.9. Minor differences, only apparent after a closer inspection, can be seen in Fig. 3.10 where the same gray scale is applied to allow for an easy comparison. In general, the major pattern is almost the same as for $c_0 = 0.002$ m s^{-1}. However, features are more pronounced. The capture probability for larger bodies is yet smaller while in case of smaller particles it remains the same. On average the capture probability is lower as expected since higher impact speeds lead to higher rebound velocities and thus larger E_J. Seemingly, the capture probability is only weakly depending on the granular temperature. Anyway, particular particle sizes seem more likely in certain regions of the rings. This general trend cannot be explained by a rather “plain” radial dependence.

Changing the particle size ratio to $\mu = 100$ yields a capture probability as shown in Fig. 3.11. Smaller grains up to 0.2 m have the highest capture probability throughout the rings. Larger bodies are generally less likely to be caught. Interestingly, at 2.4 R_S a sudden increase of

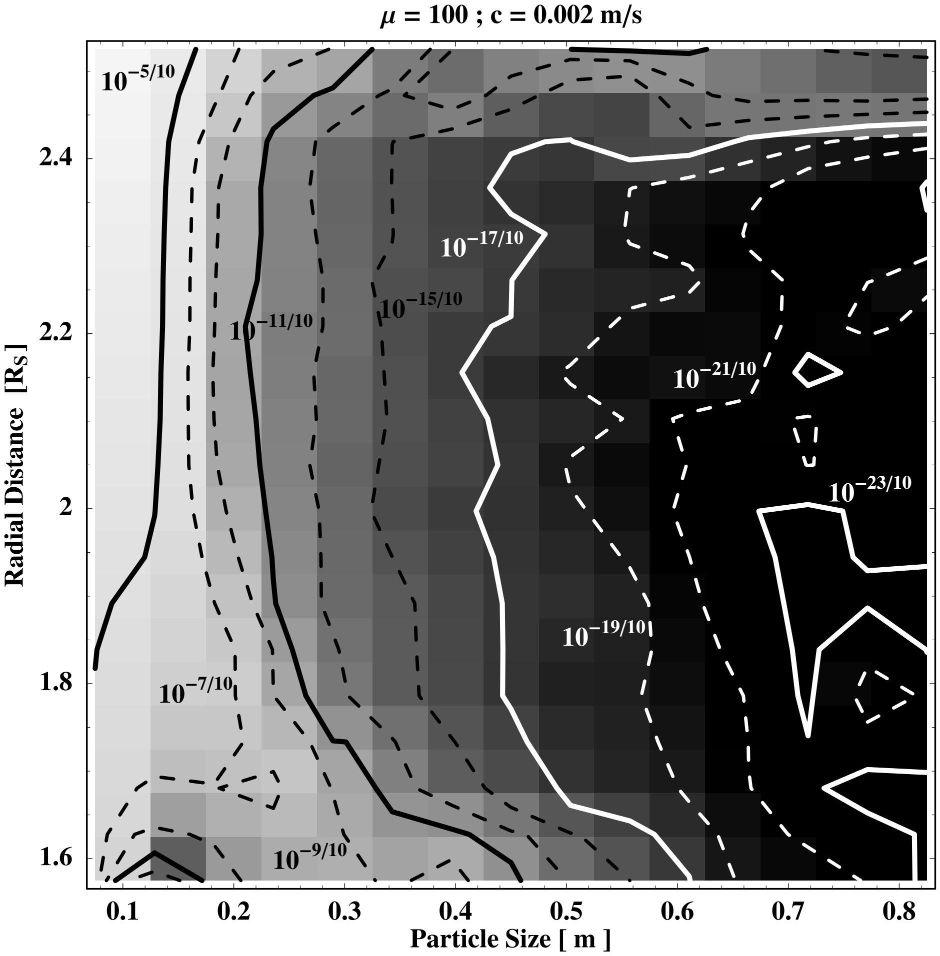

Figure 3.11: Logarithmic capture probability as a function or radial distance and particle size for a size ratio of $\mu = 100$ and $c = 0.002\ \mathrm{m\,s^{-1}}$. In general, small grains are more likely to be caught than larger ones and capture probabilities differ by at least an order of magnitude at according places. As in Figs. 3.9 and 3.10, an increase region of increased capture probability P_{capt} occurs at 2.4 R_{S} probably extending to farther distances. Note, the gray scale is not the same as for $\mu = 1$.

P_{capt} of almost one order of magnitude occurs while increasing the radial distance. This feature is independent of the grain size and falls in line with observations made in case of $\mu = 1$ (cf. Figs. 3.9 and 3.10). Applying $\mu = 0.01$, while keeping all other parameters the same, yields an overall capture probability of unity. This asymmetry with respect to μ arises from fixing the size of one of the masses and not the sum of both.

However, numerical results are by far richer in structure than predicted by the stability estimates. Although perfectly in line with Sec. 3.1, the likelihood of a collision and the actual velocity at impact do influence capture probability. Despite the general trend of smaller particles being more easily caught than larger ones, numerous interesting feature arise. However, the most striking among them, appears at about 2.3 to 2.4 R_{S} (roughly F ring and beyond). While smaller bodies up to 0.3 m still subordinate to the same pattern in P_{capt} as closer to the planet, at this given distance even larger bodies up to 0.7 m in size still show $P_{\text{capt}} = 0.05$. Closer to Saturn bodies of this size more or less do not accrete at all. Additionally, at yet farther distances than 2.4 R_S, bodies of 0.7 m do not accrete that efficiently anymore. This "tongue"-shaped region surprisingly coincides with the F ring region otherwise known to be dynamically active and fast evolving. At this point it is worthy to emphasize that the presented results are based on relative orbit dynamics including an adhesive, viscoelastic collision model. The dynamical features found are in so far independent from additional possible perturbations such as embedded moons and satellites. The particular region of the F ring seems dynamically different from the rest of the rings even though the shepherding moons, Prometheus and Pandora, and possible embedded moons or clumps are not considered in our study.

3.3 Summary and Conclusions

Results presented in this chapter cover analytical as well as numerical investigations. Although two different things, namely stability and capture probability are studied, both approaches complement each other quite nicely. In the limitations of this study, spin and rotational degrees of freedom are either partially (Sec. 3.1) or not accounted for at all (Sec. 3.2). However, follow-up collisions, likeliness of collisions, as well as the possibility of aggregation seem to be more fundamental than actual rotations. Here, results are presented with respect to the Saturnian rings but are applicable to other tidal regimes.

Many authors concerned about the grain sizes in planetary rings have considered only gravity as an attractive force. But critical limit distances as the *Roche* limit can merely determine radial limit distances and thus denote only a rough indication for actual grain sizes. No size dependence can be extracted. Gravity and a constant, non-zero restitution coefficient allow only for a radial dependence of stability and capture probability as shown in numerical simulations (Sec. 3.2). Only the combined consideration of mutual gravity and adhesive forces, or more generally, internal strength, allows for a critical radial distance to the central body as a function of a corresponding critical grain size as given by Eqs. (3.12-3.14). The proposed collision model of adhesive, viscoelastic particle interactions enables a non-zero likelihood of capture as close to Saturn as 1.6 R_S. In the same way the stability of agglomerates is ensured. A general trend is that agglomerate sizes increase with increasing distance to the planet. This if further endorsed by an enhanced capture probability at the same time. Larger grains are expected at farther distances from Saturn as observed by the VIMS-experiment on board the *Cassini* spacecraft (see Fig. 1.2). Extracted agglomerate sizes and a "transition" size of about 0.5 m with respect to the capture probability (cf. Sec. 3.2) point towards decimeter-sized grains for the inner ring system. This roughly coincides with observations (Marouf et al., 1983; Showalter and Nicholson, 1990; French and Nicholson, 2000), where sizes range between a few centimeters and a few meters have been observed.

Based on Sec. 3.1, equally sized agglomerates appear more fragile than those consisting of differently shaped grains. They are easier to be disrupted by either tidal forces or further impacts of third objects. However, larger assemblies of grains, $N > 2$, may as well be compactified during yet additional impacts and would thus become more robust. Additionally, capture is less probable in case of $\mu = 1$ than otherwise. This general qualitative trend coincides with analytical estimates as well as numerical simulations. Smaller grains resting on larger ones are first of all more stable and second more likely to be captured, as is true in a purely gravitational interaction as well. Results on stability and capture probability further promote the existence of regolith layers throughout the main rings. Their thickness most probably varies with radial distance to the central body. Since regolith layers cannot be treated as perfectly smooth spheres anymore, the elasticity of follow-up impacts may depend on their orbit locations and would be decreased with increasing layer thickness. Furthermore, this implies a not only material and impact speed dependent but also location dependent restitution coefficient. This aspect is not included in current literature and would be worthwhile to investigate.

Regolith layers, are likely to be very common, and moreover, are likely to be transient features, since they are apparently as easily established as destroyed. Shattering impacts may temporarily deliver vast amounts of regolith dust into orbit, which eventually will be re-accumulated. This could provide the base to account for a vivid size distribution dynamics within the F-ring. An apparently increased capture probability at orbit distances between 2.3 to 2.4 R_S could enhance such structural reorganizations. A dynamical combination of agglomeration and fragmentation based on collision dynamics implies that small particles can denote the essence of fast dynamical processes. Whether these processes would be perfectly balance is still disputable. A resulting, merely transient dynamics without leading to effective growth processes could be detectable in form of brightness fluctuations. Models proposed and observations made (Showalter, 1998; Poulet et al., 2000b,a; Barbara and Esposito, 2002; Showalter, 2004) would be endorsed while general pattern of ringlet structures and indications about the number of possible moons could be extracted.

Chapter 4

Kinetic description

In the context of the description of granular gases, concepts of kinetic theory are widely used. Dry granular matter is well described by *Boltzmann* or *Chapman-Enskog* equations (Boltzmann, 1896; Chapman and Cowling, 1970; Resibois et al., 1977), where the number of colliding particles is conserved. These models have been extended to allow for inelastic collisions and finite size effects (Goldreich and Tremaine, 1978; Araki and Tremaine, 1986; Jenkins and Richman, 1985). This description fails if either attractive forces play a role and/or the relative (thermal) velocity of the particle ensemble becomes large enough to erode the particles. In these cases coagulation and fragmentation change the mass distribution, the total number of particles, and their individual masses while the total mass is conserved. The interplay between coagulation and fragmentation is important in many fields, but corresponding integro-differential equations mainly focus on the mass distribution only (Silk and Takahashi, 1979; Barrow, 1981; Bishop and Searle, 1983; Family et al., 1986). Coagulation equations are generally based on the *Smoluchowski* equation (Smoluchowski, 1916) and have been modified to account for a restricted coagulation domain (Menci et al., 2002; Mamon, 1992). Many authors introduced "hybrid" models, where the mass evolution is treated with a kinetic-like equation (fragmentation or coagulation), while the velocity and spatial evolution is considered separately (particle in a box or similar approximation (e.g. Greenberg et al., 1978; Wetherill and Stewart, 1993; Krivov et al., 2000)).

All possible collisional outcomes *i)* coagulation[1], *ii)* restitution, and *iii)* fragmentation[2] sensitively depend on collision dynamics (cf. Chapter 2 and e.g. Spahn et al. (2004)). The predominance of the coagulation, the restitution, or the fragmentation regime can vary strongly for different systems and determines the width of the respective domain, roughly sketched in Fig. 4.1. Planetary rings, on one hand, are dominated by restitution where the random walk speed is relatively low (mm/s - cm/s) and tidal forces compete with coagulation (Stewart et al., 1984; Salo, 1995; Albers and Spahn, 2006, and cf. Chapter 3). On the other hand, in pre-planetary disks the restitution regime almost shrinks to a narrow line (Blum and Wurm, 2000) due to larger relative velocities of the grains and less important tidal forces. Yet different from such disks as planetary rings or pre-planetary[3] disks are ensembles dominated

---

[1] Note, that aggregation and coagulation are different processes where the latter is applied to the merging of two liquid droplets while the first denotes agglomeration of two solid grains as discussed in Chapter 2. However, we concentrate on coagulation for simplicity and will nevertheless apply previously obtained results.

[2] Fragmentation may include cratering as well as shattering impacts.

[3] The ensembles show a significant amount of gas besides the grain population. Gas effects the effective net growth as well as the restitution coefficient (Wurm et al., 2004). It therefore cannot be neglected if one

by fragmentation as e.g. the *Edgeworth-Kuiper* belt (Stern, 1995; Krivov et al., 2005) or debris disks such as Vega (Thébault et al., 2003).

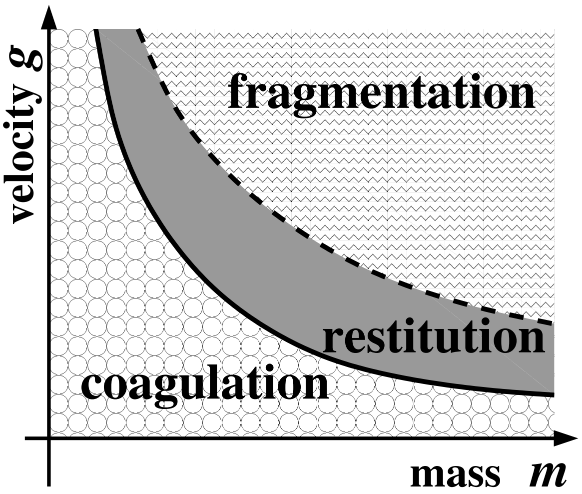

Figure 4.1: "Phase diagram" for different collisional outcomes in the plane defined by the (effective) mass and the impact speed. Domains are defined by critical impact velocities for either restitution (solid line) or in case of higher impact velocities for fragmentation (dashed line) to occur.

4.1 Time Evolution of the Ensemble

4.1.1 General Considerations

Denoting the particle's mass M, location vector $\vec{R}$, velocity $\vec{V}$, and the time t, the generalized distribution function $F = F(M,\vec{R},\vec{V},t)$ with dimension $[F] = \mathrm{kg}^{-1}\ \mathrm{m}^{-6}\ \mathrm{s}^{3}$ is introduced and denotes the number of particles $\mathrm{d}N$ in a phase space volume element $\mathrm{d}^3V\mathrm{d}^3R\ \mathrm{d}M$ by $\mathrm{d}N = F(M,\vec{R},\vec{V},t)\ \mathrm{d}^3V\mathrm{d}^3R\ \mathrm{d}M$. In order to emphasize the essentials only spherical particles will be discussed here. In analogy to the *Stoßzahlansatz* introduced by *Boltzmann* the time evolution of F referring to a given point in phase space is the difference between gain $\mathcal{G}$ and loss terms $\mathcal{L}$

$$\frac{\mathrm{D}}{\mathrm{D}t}\,F(M,\vec{R},\vec{V},t) \quad = \quad \left.\frac{\mathrm{d}F}{\mathrm{d}t}\right|_{\text{coagulation}} + \left.\frac{\mathrm{d}F}{\mathrm{d}t}\right|_{\text{restitution}} + \left.\frac{\mathrm{d}F}{\mathrm{d}t}\right|_{\text{fragmentation}} . \tag{4.1}$$

Each part corresponds to gains and losses generated by the three collisional outcomes: *(i)* coagulation, *(ii)* restitution, and *(iii)* fragmentation. In this context the system dynamics is implicitly given by the total time derivative $\mathrm{D}/\mathrm{D}t = \partial/\partial t + \vec{V}\cdot\partial/\partial\vec{R} + \vec{f}\cdot\partial/\partial\vec{V}$ where $\vec{f} = -\partial/\partial\vec{R}\ \Phi_{\mathrm{ext}}(\vec{R})/M$ and separated from mutual particle interactions Φ_{ij} covered by $\mathcal{G}$ and $\mathcal{L}$. Here, particle interactions in form of physical collisions of two particles, $\vec{x}_1 = (m_1,\vec{r}_1,\vec{v}_1)$ and $\vec{x}_2 = (m_2,\vec{r}_2,\vec{v}_2)$, will be discussed. At this point, their mutual gravitational influence is deliberately neglected. Two major assumptions are generally made:

A) **Low density assumption**:
If the system under consideration is sufficiently dilute, particle contacts are binary

---

describes pre-planetary disks.

collisions only. In terms of the BBGKY-hierarchy[4], it furthermore ensures a cut-off of higher correlation ($m > 3$). Thus, binary interactions in general may be considered as a scattering of grains into and out of a given phase space volume d^7X. It furthermore justifies the gain and loss approach.

B) **The molecular chaos assumption**:
In order to apply this simple ansatz of a master or balance equation, the particle distribution functions must be uncorrelated. Therefore, following the BBGKY hierarchy the two-particle distribution function is expressed as

$$F^{(2)}(\vec{x}_1,\vec{x}_2,t) \quad = \quad F^{(1)}(\vec{x}_1,t)\cdot F^{(1)}(\vec{x}_2,t)\ , \tag{4.2}$$

where the usually added correlation term $h(\vec{x}_1,\vec{x}_2,t)$ is considered negligible.[5]

A collision of two particles, $\vec{x}_1$ and $\vec{x}_2$, is accounted for by the collision kernel $W(\vec{x}_1,\vec{x}_2,\vec{X})$ that includes all information about the changes of F, in mass, space, and velocities, at a given collision point $\vec{X} = (M,\vec{R},\vec{V})$ and may be interpreted as a collision probability. Thus, $W(\vec{x}_1,\vec{x}_2,\vec{X})\ \mathrm{d}^7X$ denotes a number of particles where W has the dimension $[W] = \mathrm{kg}^{-1}\ \mathrm{m}^{-6}\ \mathrm{s}^2$. Now, picturing a particle immersed in an ensemble and moving along with it, every possible collision with any possible other particle has to be accounted for. Thus,

- **gain** $\mathcal{G}$ is the number of collisions in Δt by which a particle in $(m,m+\Delta m;\vec{r},\vec{r}+\Delta\vec{r};\vec{v},\vec{v}+\Delta\vec{v})$ is deflected into the phase space interval under consideration $(M,\vec{R},\vec{V})$

$$\mathcal{G} \quad = \quad \int \mathrm{d}^7x_1 \int \mathrm{d}^7x_2\ W^{(\mathcal{G})}(\vec{x}_1,\vec{x}_2,\vec{X})\ F(\vec{x}_1)\ F(\vec{x}_2)\ . \tag{4.3}$$

- **loss** $\mathcal{L}$ is the number of collisions in Δt by which the particles are scattered out of the volume under consideration $(M,\vec{R},\vec{V})$

$$\mathcal{L} \quad = \quad \int \mathrm{d}^7x_1 \int \mathrm{d}^7x_2\ W^{(\mathcal{L})}(\vec{x}_1,\vec{x}_2,\vec{X})\ F(\vec{x}_1)\ F(\vec{x}_2)\ . \tag{4.4}$$

The evolution of a distribution function $F(\vec{X},t)$ in time is given by the basic kinetic equation

$$\frac{\mathrm{D}}{\mathrm{D}t}F(\vec{X}) \quad = \quad \int \mathrm{d}^7x_1 \int \mathrm{d}^7x_2\ \left(W^{(\mathcal{G})}(\vec{x}_1,\vec{x}_2,\vec{X}) - W^{(\mathcal{L})}(\vec{x}_1,\vec{x}_2,\vec{X})\right)\ F(\vec{x}_1)\ F(\vec{x}_2)\ , \tag{4.5}$$

where

$$W^{(\mathcal{G}/\mathcal{L})}(\vec{x}_1,\vec{x}_2,\vec{X}) \quad = \quad \sigma\ v_{\mathrm{imp}}\ \mathcal{F}\ \ \delta(\vec{r}_1-\vec{r}_2)\ \mathcal{P}(\vec{x}_1,\vec{x}_2,\vec{X})\ . \tag{4.6}$$

The flux of incoming particles $\sigma\ v_{\mathrm{imp}}\ \mathcal{F}$ contains the geometrical cross section σ and the relative impact speed of both grains $v_{\mathrm{imp}} = |\vec{g}| = |\vec{v}_2 - \vec{v}_1|$. It furthermore accounts for focusing effects $\mathcal{F}$, thus denoting a possibility to at least partially incorporate long-range particle interactions as e.g. gravitational focusing in terms of the *Safronov* factor $\mathcal{F} = \mathcal{F}_{\mathrm{Saf}} = (1+v_{\mathrm{esc}}^2/g^2)$ (Safronov, 1969; Stewart and Ida, 2000) or Coulomb forces (Ivlev et al., 2002), that can either increase or decrease the effective cross section. This may be illustrated as

---

[4] In general, dynamics is described in terms of an N-particle distribution function. The BBGKY hierarchy introduces reduced distribution functions for one, two, and more particles. The time evolution of the n^{th} order distribution function is then determined by the order $n+1$.

[5] For simplicity, $F^{(1)}(\vec{x},t)$ will further on be denoted as $F(\vec{x},t)$ as introduced above.

an either larger or smaller volume occupied by the grains. The geometrical cross section of two spherical particles reads

$$\sigma(m_1, m_2) = \pi \left(\frac{3}{4\pi\rho}\right)^{2/3} \left(m_1^{1/3} + m_2^{1/3}\right)^2 , \qquad (4.7)$$

where ρ denotes the grain's density. The δ-function $\delta(\vec{r}_1 - \vec{r}_2)$ provides the impact condition, i.e. whether particles do collide or not and additionally serves as a normalization. The distribution $\mathcal{P} = \mathcal{P}(\vec{x}_1, \vec{x}_2, \vec{X})$ accounts for the collisional outcome as there can be *(i)* coagulation, *(ii)* restitution, and *(iii)* fragmentation (cf. Chapter 2). It contains information about the number of remaining particles, and conservation of energy and momentum after the impact. In case of fragmentation, it additionally gives the fragment mass and velocity distribution. Thus, $\int \mathrm{d}^7 X\, \mathcal{P}$ denotes the number of fragments N_f where $\mathcal{P}$ has the dimension $[\mathcal{P}] = \mathrm{kg}^{-1}\ \mathrm{m}^{-6}\ \mathrm{s}^3$. In general, $N_\mathrm{f} > 2$, since $N_\mathrm{f} = 1$ and $N_\mathrm{f} = 2$ refer to coagulation and restitution, respectively. In particular, $\mathcal{P}$ reads for different collision scenarios:

- **"producing" one particle**: (gain term of coagulation)
  If two particles, $\vec{x}_1$ and $\vec{x}_2$, coagulate they will form a single spherical particle of mass $M = m_1 + m_2$ and velocity $\vec{V} = \vec{v}_\mathrm{c}$ at point $\vec{R}$, where $\vec{v}_\mathrm{c}$ denotes the center of mass velocity of both grains. Thus,

$$\mathcal{P}(\vec{x}_1, \vec{x}_2, \vec{X}) = \delta(\vec{R} - \vec{r}_1)\, \delta(M - (m_1 + m_2))\, \delta(\vec{V} - \vec{v}_\mathrm{c}) . \qquad (4.8)$$

- **"destroying" one particle**: (loss term of coagulation or fragmentation)
  If two particles collide and will either form a single one as above or will, even if only partially, be destroyed, they are lost to that particular phase space volume. This can be expressed as

$$\mathcal{P}(\vec{x}_1, \vec{x}_2, \vec{X}) = \delta(\vec{R} - \vec{r}_1)\, \delta(M - m_1)\, \delta(\vec{V} - \vec{v}_1) . \qquad (4.9)$$

- **"generating" a new distribution of particles**: (gain term of fragmentation)
  In case of fragmenting collisions, debris has a distinct mass and velocity distribution that can generally be given as $p(\vec{x}_1, \vec{x}_2, \vec{X})$ with dimension $[p] = \mathrm{kg}^{-1}\ \mathrm{m}^{-3}\ \mathrm{s}^3$. Laboratory experiments and theoretical discussions provide details about the distribution and may "simply be plugged in" at this point. Thus the only condition that is necessary in this general framework is to account for the actual location of the particle at impact

$$\mathcal{P}(\vec{x}_1, \vec{x}_2, \vec{X}) = \delta(\vec{R} - \vec{r}_1)\, p(\vec{x}_1, \vec{x}_2, \vec{X}) . \qquad (4.10)$$

- **"changing" the velocity of particles**: (gain and loss term of restitution)
  In case of restitution the mass distribution will remain unchanged whereas the velocity distribution is changed according to the geometry of the impact and the particle properties. Thus, one has to account for energy and momentum conservation only

$$\mathcal{P}(\vec{x}_1, \vec{x}_2, \vec{X}) = \delta(\vec{R} - \vec{r}_1)\, \delta(M - m_1)\, \delta(\vec{v}_\mathrm{c} - \vec{v}_\mathrm{c}\,')\, \delta(\frac{1}{2}(\vec{g} - \vec{g}\,')) . \qquad (4.11)$$

Any possible scenario could be expressed in terms of integration kernels or transition probabilities. This kinetic approach is rather general and as usual gains complexity with including more and more dynamical details. However, any of the outcomes is determined by the masses of both particles, m_1 and m_2, and the relative impact velocity $\vec{g}$ according to Fig. 4.1 and in agreement with Chapter 2. If the impact velocity is smaller than a critical velocity for restitution to occur $\vec{g}_\mathrm{c}$, the outcome can only be a coagulating collision. In case of high impact velocities a second critical velocity $\vec{g}_\mathrm{f}$, distinguishes between fragmentation and restitution. These critical parameters are either obtained by theoretical modeling (cf. Sec. 2.4.1) or experimentally for either coagulation (e.g. Hatzes et al., 1991; Dilley and Crawford, 1996) or fragmentation (e.g. Higa et al., 1998). In terms of kinetic theory these are merely input parameters and will henceforth be treated as such.

4.1.2 Equations for Coagulation and Fragmentation

Changes to the mass distribution are introduced by coagulation (c) and fragmentation (f). Restitution, however, may only indirectly contribute while modifying the velocity distribution. Velocities, and especially the relative velocity, determine not only the outcome of a collision but the collision probability as well, which gives a direct feedback to the size distribution. Restitutive collisions, which can be very frequent after shattering impacts can rapidly thermalize the ensemble (Salo, 1995). Considerable changes of the mass distribution require a huge number of collisions whereas for thermalization only a few of them are necessary. Thus, in order to extract the essence of possible growth processes or considerable changes of the size or mass distribution, in this section we concentrate on coagulation and fragmentation alone.

In terms of the “phase diagram” in Fig. 4.1 there remain only the corresponding two domains and Eq. (4.5) may be written as (Spahn et al., 2004)

$$\frac{\mathrm{D}}{\mathrm{D}t} F(\vec{X}) = \mathcal{G}^{\,\mathrm{(c/f)}}(\vec{X}) - \mathcal{L}^{\,\mathrm{(c/f)}}(\vec{X}) \,. \tag{4.12}$$

It is easier to express all velocities in the center of mass frame where $\vec{v}_\mathrm{c}$ and $\vec{g}$ denote the center of mass and relative velocity according to $\vec{v}_\mathrm{c} = (m_1\vec{v}_1 + m_2\vec{v}_2)/(m_1+m_2)$ and $\vec{g} = \vec{v}_2 - \vec{v}_1$. The velocity of each particle is then expressed as $\vec{v}_1 = \vec{v}_\mathrm{c} - m_1\,\vec{g}/(m_1+m_2)$ and $\vec{v}_2 = \vec{v}_\mathrm{c} + m_2\,\vec{g}/(m_1+m_2)$. The two dynamical domains, defined by $\vec{g}_\mathrm{c}$ and $\vec{g}_\mathrm{f}$ and denoted by $\mathcal{D}_\mathrm{c/f}$, give rise to the following gain and loss expressions

$$\mathcal{G}^{\,\mathrm{(c/f)}}(\vec{X}) = \int_0^\infty \mathrm{d}m_1 \int_0^\infty \mathrm{d}m_2 \int_{\mathbb{R}^3} \mathrm{d}^3v_\mathrm{c} \int_{\mathcal{D}_\mathrm{c/f}} \mathrm{d}^3g\, W_{\mathcal{G}}^{\mathrm{(c/f)}}(M,\vec{V};m_1,m_2,\vec{g})\, F(\vec{x}_1)\, F(\vec{x}_2) \tag{4.13}$$

$$\mathcal{L}^{\,\mathrm{(c/f)}}(\vec{X}) = \int_0^\infty \mathrm{d}m_1 \int_0^\infty \mathrm{d}m_2 \int_{\mathbb{R}^3} \mathrm{d}^3v_\mathrm{c} \int_{\mathcal{D}_\mathrm{c/f}} \mathrm{d}^3g\, W_{\mathcal{L}}^{\mathrm{(c/f)}}(M,\vec{V};m_1,m_2,\vec{g})\, F(\vec{x}_1)\, F(\vec{x}_2) \,. \tag{4.14}$$

Note, that these equations have already been integrated with respect to $\delta(\vec{r}_1 - \vec{r}_2)$. In case of coagulation the according kernels may written according to Eqs. (4.6), (4.8), and (4.9) in a more compact way as

$$W_{\mathcal{G}/\mathcal{L}}^{\mathrm{(c)}} = \frac{1}{2}\,\sigma\,|\vec{g}|\,\mathcal{F}(m_1,m_2,\vec{g})\,\delta(m_{\mathcal{G}/\mathcal{L}} - M)\,\delta\left(\vec{v}_{\mathcal{G}/\mathcal{L}} - \vec{V}\right)\,, \tag{4.15}$$

where $m_\mathcal{G} = m_1 + m_2$ and $m_\mathcal{L} = m_2$, and $\vec{v}_\mathcal{G} = (m_1\vec{v}_1 + m_2\vec{v}_2)/(m_1+m_2)$ and $\vec{v}_\mathcal{L} = \vec{v}_2$. The factor of $1/2$ arises due to the symmetry with respect to an exchange of particles.

Fragmentation on the other hand forms post-collisional mass and velocity distributions as indicated before. In contrast to coagulation where a single particle with a distinct mass and velocity is created, fragments may cover a broad range of masses and velocities which are difficult to derive from basic principles. Gain and loss term may then be formulated in accordance to Eqs. (4.6), (4.10), and (4.9) as follows (Krivov et al., 2000; Spahn et al., 2004; Krivov et al., 2005)

$$W^{(\mathrm{f})}_{\mathcal{G}/\mathcal{L}} \;=\; \sigma\,|\vec{g}|\;\mathcal{F}\,(m_1,m_2,\vec{g})\left[\mathcal{T}\,(M,\vec{V}|m_1,m_2,\vec{g}) - \delta(m_2-M)\;\delta(\vec{v}_2-\vec{V})\right]\;, \quad (4.16)$$

where $\mathcal{T}$ denotes the normalized distribution of fragments. Neglecting the direct effects of restitutive collisions, critical velocities for coagulation and fragmentation to occur can be considered to be almost the same $g_{\mathrm{c}} \approx g_{\mathrm{f}}$, which is very likely in pre-planetary disks.

4.2 Evolution of the Mass Distribution

All information about the ensemble is stored in the generalized distribution function whereas the physical interactions are covered by the integral kernels. This, however, is a highly complex problem to be investigated in this general manner. Concentrating on a particular part of the distribution function as e.g. the mass distribution or the velocity distribution alone, would simplify the analytical treatment of this problem. Both examples are already known in literature and treated in a more phenomenological way as the *Smoluchowski* (Smoluchowski, 1916) and the *Boltzmann* equation (Boltzmann, 1896), respectively. In the following, we emphasize the mass distribution considering coagulation and continue in the line of this thesis, i.e. determining overall influences of aggregating collisions.

4.2.1 General Assumptions

In order to extract information about sizes alone, a separation ansatz for the distribution function may be applied

$$F(\vec{x},t) \;=\; n(m,\vec{r},t)\cdot f(m,\vec{v})\;, \quad (4.17)$$

where $n(m,\vec{r},t)$ denotes the size and space, and $f(m,\vec{v})$ the velocity distribution. As a first step and in order to continue analytically a *Maxwellian* velocity distribution with a dispersion according to energy equipartition $v_{\mathrm{th}} = \sqrt{(2T/m_{\mathrm{eff}})}$ (Ivlev et al., 2002; Lee, 2000) is assumed, where T denotes the granular temperature and $k_{\mathrm{B}} = 1$. Furthermore, the ensemble is thermalized having the same granular temperatures at any point, i.e. $T = T_1 = T_2$. Then,

$$\begin{aligned} F(\vec{x}_1,t)\cdot F(\vec{x}_2,t) &= n(m_1,\vec{r}_1,t)\;f(m_1,\vec{v}_1)\cdot n(m_2,\vec{r}_2,t)\;f(m_2,\vec{v}_2) && (4.18)\\ &= n(m_1,\vec{r}_1,t)\cdot n(m_2,\vec{r}_2,t) \\ &\quad\times C_1\exp\left[-\frac{m_1}{2T}\,\vec{v}_1^{\,2}\right]\;C_2\exp\left[-\frac{m_2}{2T}\,\vec{v}_2^{\,2}\right] && (4.19)\end{aligned}$$

where C_1 and C_2 are the normalization constants. Since $m_1\vec{v}_1^{\,2} + m_2\vec{v}_2^{\,2} = (m_1+m_2)\vec{v}_{\mathrm{c}}^{\,2} + m_{\mathrm{eff}}\vec{g}^{\,2}$ the distribution functions read

$$\begin{aligned} F(\vec{x}_1,t)\;F(\vec{x}_2,t) &= n(m_1,\vec{r}_1,t)\cdot n(m_2,\vec{r}_2,t) \\ &\quad\times C_{\vec{v}_{\mathrm{c}}}\;\exp\left[-\frac{(m_1+m_2)}{2T}\,\vec{v}_{\mathrm{c}}^{\,2}\right]\;C_{\vec{g}}\;\exp\left[-\frac{m_{\mathrm{eff}}}{2T}\vec{g}^{\,2}\right]\;, && (4.20)\end{aligned}$$

where

$$C_{\vec{v}_{\rm c}} = \left(\frac{(m_1+m_2)}{2\pi T}\right)^{3/2} \quad \text{and} \quad C_{\vec{g}} = \left(\frac{m_{\rm eff}}{2\pi T}\right)^{3/2} = v_{\rm th}^{-3}\pi^{-3/2} . \tag{4.21}$$

4.2.2 Coagulation Equation

Apart from considering all complex dynamical interactions of fragmentation and coagulation, many systems can be described by coagulation or fragmentation alone. While concentrating on coagulation, only growth processes are taken into account. At this point it will be interesting to restrict interactions to physical collisions and to apply results obtained in Chapter 2. Then, restitution is implicitly included.

The influence of physical collisions is best studied in the free case, where all external forces are neglected, i.e. $\mathrm{D}/\mathrm{D}t \to \partial/\partial t$. Equation (4.12) then reads

$$\frac{\partial}{\partial t} F(\vec{X}) = \mathcal{G}^{\,(\rm c)}(\vec{X}) - \mathcal{L}^{\,(\rm c)}(\vec{X}) . \tag{4.22}$$

Using the separation ansatz and in particular Eq. (4.20) allows for the direct evaluation of at least some of the integrals. Eq. (4.12) is written in its explicit and complete form together with Eqs. (4.13), (4.15), (4.20), and (4.21). They can simply be integrated with respect to mass m_2 using $\delta(m_{\mathcal{G}/\mathcal{L}} - M)$ and $\vec{V}$ using $\delta(\vec{v}_{\mathcal{G}/\mathcal{L}} - \vec{V})$. Expressing m_1 as m hereafter for convenience, Eq.(4.20) can be written as

$$\begin{aligned}
\frac{\partial}{\partial t} n(M,\vec{R},t) = {} & \frac{1}{2}\int\limits_0^M \mathrm{d}m \int\limits_{\mathbb{R}^3} \mathrm{d}^3 v_{\rm c} \int\limits_{\mathcal{D}_{\rm c}} \mathrm{d}^3 g\, \sigma\, |\vec{g}|\, \mathcal{F}\,(m, M-m, \vec{g})\, n(m,\vec{r},t) n(M-m,\vec{r},t) \\
& \times C_{\vec{v}_{\rm c}}^{(\mathcal{G})} \exp\left[-\frac{M}{2T}\vec{v}_{\rm c}^{\,2}\right] C_{\vec{g}}^{(\mathcal{G})} \exp\left[-\frac{m_{\rm eff}}{2T}\vec{g}^{\,2}\right] \\
& - n(M,\vec{R},t) \int\limits_0^\infty \mathrm{d}m \int\limits_{\mathbb{R}^3} \mathrm{d}^3 v_{\rm c} \int\limits_{\mathcal{D}_{\rm c}} \mathrm{d}^3 g\, \sigma\, |\vec{g}|\, \mathcal{F}\,(m, M, \vec{g})\, n(m,\vec{r},t) \\
& \times C_{\vec{v}_{\rm c}}^{(\mathcal{L})} \exp\left[-\frac{(M+m)}{2T}\vec{v}_{\rm c}^{\,2}\right] C_{\vec{g}}^{(\mathcal{L})} \exp\left[-\frac{m_{\rm eff}}{2T}\vec{g}^{\,2}\right] ,
\end{aligned} \tag{4.23}$$

where

$$C_{\vec{v}_{\rm c}}^{(\mathcal{G})} = \left(\frac{M}{2\pi T}\right)^{3/2} , \quad C_{\vec{g}}^{(\mathcal{G})} = \left(\frac{m_{\rm eff}}{2\pi T}\right)^{3/2} = v_{\rm th}^{(\mathcal{G})}\pi^{-3/2} , \tag{4.24}$$

$$C_{\vec{v}_{\rm c}}^{(\mathcal{L})} = \left(\frac{M+m}{2\pi T}\right)^{3/2} , \quad C_{\vec{g}}^{(\mathcal{L})} = \left(\frac{Mm}{2\pi T(m+M)}\right)^{3/2} = v_{\rm th}^{(\mathcal{L})}\pi^{-3/2} , \tag{4.25}$$

and

$$\left(v_{\rm th}^{(\mathcal{L})}\right)^2 = \left(v_{\rm th}^{(\mathcal{G})}\right)^2 \left(1 - \frac{m}{M}\right)^2 . \tag{4.26}$$

The integration with respect to $\vec{v}_{\rm c}$ is easily done provided a thermalization of the ensemble can be assumed. As mentioned above, restitutive collisions occurring for velocities higher than the critical impact speed $|\vec{g}| > |\vec{g}_{\rm cr}| = |\vec{g}_{\rm c}|$ may sufficiently contribute to this process.

Equation (4.23) yields a coagulation equation accounting for a possible restriction of the dynamical domain $\mathcal{D}_\mathrm{c}$ and reads

$$\begin{aligned}\frac{\partial}{\partial t}\, n(M,\vec{R},t) &= \frac{1}{2}\int_0^M \mathrm{d}m \int_{\mathcal{D}_\mathrm{c}} \mathrm{d}^3 g\, \frac{\sigma\,|\vec{g}|}{\pi^{3/2}(v_\mathrm{th}^{(\mathcal{G})})^3}\, \mathcal{F}\,(m,M-m,\vec{g}) \\ &\quad \times\, n(m,\vec{r},t)\, n(M-m,\vec{r},t)\, \exp\left[-\frac{\vec{g}^{\,2}}{(v_\mathrm{th}^{(\mathcal{G})})^2}\right] \\ &\quad - n(M,\vec{R},t)\int_0^\infty \mathrm{d}m \int_{\mathcal{D}_\mathrm{c}} \mathrm{d}^3 g\, \frac{\sigma\,|\vec{g}|}{\pi^{3/2}(v_\mathrm{th}^{(\mathcal{L})})^3}\, \mathcal{F}\,(m,M,\vec{g}) \\ &\quad \times\, n(m,\vec{r},t)\, \exp\left[-\frac{\vec{g}^{\,2}}{(v_\mathrm{th}^{(\mathcal{L})})^2}\right]\,. \end{aligned} \tag{4.27}$$

The critical velocity $\vec{g}_\mathrm{cr}$ restricts the probability of coagulation. Its three spatial components $(v_\mathrm{cr}, t_\mathrm{cr}, b_\mathrm{cr})$ may be considered separately, where then results obtained in Chapter 2 may be easily applied. Excluding any particle interaction besides direct collisions, i.e. $\mathcal{F}\,(m,M-m,\vec{g}) = \mathcal{F}\,(m,M,\vec{g}) = 1$, and excluding any binormal particle motion by approximating $\varepsilon_\mathrm{B} \approx \varepsilon_\mathrm{T}$ and thus $b_\mathrm{cr} \approx t_\mathrm{cr}$, the following integral generally accounts for the reduced phase space

$$\tilde{\mathcal{C}}\,(v_\mathrm{th}, v_\mathrm{cr}, t_\mathrm{cr}) = \int_{\mathcal{D}_\mathrm{c}} \mathrm{d}^3 g\, |\vec{g}|\, \exp[-\frac{\vec{g}^{\,2}}{v_\mathrm{th}^2}] = \int_{\mathcal{D}_\mathrm{c}} \mathrm{d}^3 g\, f(\vec{g})\,. \tag{4.28}$$

v_cr and t_cr denote the critical normal and possible tangential impact speed. Even if binormal motion is omitted completely, $\varepsilon_\mathrm{B} = 1$, the corresponding velocity space would yet be larger since $b_\mathrm{cr} \longrightarrow \infty$ and thus $b_\mathrm{cr} \gg t_\mathrm{cr}$. Choosing $b_\mathrm{cr} \approx t_\mathrm{cr}$, the dynamical domain and can be considered as a limit case within this study. As it is apparent, only particles approaching each other can collide and therefore $\vec{g}\cdot\vec{e}_d \geq 0$, where $\vec{e}_d$ is the unit vector $\vec{e}_d = (\vec{r}_2 - \vec{r}_1)/|\vec{r}_2 - \vec{r}_1|$ as defined in Chapter 2.

The integration of Eq. (4.28) is presented in Appendix A and yields

$$\tilde{\mathcal{C}}\,(v_\mathrm{th}, v_\mathrm{cr}, t_\mathrm{cr}) = \int_{\mathcal{D}_\mathrm{c}} \mathrm{d}g\, g^3\, \exp[-\frac{g^2}{v_\mathrm{th}^2}] = 2\pi[\ \mathrm{Integral}_\mathbf{A} + \mathrm{Integral}_\mathbf{B}\ ]\,, \tag{4.29}$$

as given in Eq. (A.6) together with Eqs. (A.4) as $\mathrm{Integral}_\mathbf{A}$ and (A.5) as $\mathrm{Integral}_\mathbf{B}$. The full equation may be found in Appendix A and will be applied in numerical simulations below. Restricting merely the absolute value of the critical velocity g_cr instead of single components yields an equation much easier to handle (cf. Eq. (A.11), Spahn et al. (2004))

$$\tilde{\mathcal{C}}\,(v_\mathrm{th}, g_\mathrm{cr}) = \int_{\mathcal{D}_\mathrm{c}} \mathrm{d}g\, f(\vec{g}) = 2\pi \int_0^{g_\mathrm{cr}} \mathrm{d}^3 g \int_0^{\pi/2} \mathrm{d}\vartheta\, g^3 \cos\vartheta \sin\vartheta\, \exp[-\frac{g^2}{v_\mathrm{th}^2}]\,. \tag{4.30}$$

In general, both approaches show the same behavior and may be written as $\tilde{\mathcal{C}} = \pi v_\mathrm{th}^4 \mathcal{C}$. The asymptotic limit for either $v_\mathrm{cr} \longrightarrow \infty$ and $t_\mathrm{cr} \longrightarrow \infty$, Eq. (A.9), or $g_\mathrm{cr} \longrightarrow \infty$, Eq. (A.12), yields the same result

$$\lim_{t_\mathrm{cr}\to\infty}\ \lim_{v_\mathrm{cr}\to\infty} \tilde{\mathcal{C}}\,(v_\mathrm{th}, v_\mathrm{cr}, t_\mathrm{cr}) = \lim_{g_\mathrm{cr}\to\infty} \tilde{\mathcal{C}}\,(v_\mathrm{th}, g_\mathrm{cr}) = \pi v_\mathrm{th}^4\,. \tag{4.31}$$

Obviously, one may write $\mathcal{C} = 1$ in these limit cases. These correction factors corresponding to either gain or loss only differ in according thermal velocities, either $v_{\mathrm{th}}^{\mathcal{G}}$ or $v_{\mathrm{th}}^{\mathcal{L}}$. The exact behavior of $\mathcal{C}$ as a function of impact speed g_{cr} is shown in Fig. 4.2. Clearly, coagulation is always possible in the above mentioned limit cases. However, if a critical impact velocity is applied an almost non-continuous transition occurs denoting the separation of coagulation and restitution. If normal and tangential components of $\vec{g}_{\mathrm{cr}}$ are considered separately as in Eq. (4.29), the transition is not that sudden anymore and a local minimum of transition probability arises. Thermal velocities merely shift the transition zone in favor of restitution.

Therefore, in case of a generally restricted coagulation domain the coagulation equation Eq. (4.27) reads (Spahn et al., 2004)

$$\begin{aligned}\frac{\partial}{\partial t}\, n(M,\vec{r},t) \;&=\; \frac{1}{2}\int_{0}^{M} \mathrm{d}m\, \frac{\sigma\,(v_{\mathrm{th}}^{\mathcal{G}})}{\sqrt{\pi}}\, \mathcal{C}\,(v_{\mathrm{th}}^{\mathcal{G}},\vec{g}_{\mathrm{cr}})\; n(m,\vec{r},t)\; n(M-m,\vec{r},t) \\ &\quad - n(M,\vec{r},t)\int_{0}^{\infty} \mathrm{d}m\, \frac{\sigma\,(v_{\mathrm{th}}^{\mathcal{L}})}{\sqrt{\pi}}\, \mathcal{C}\,(v_{\mathrm{th}}^{\mathcal{L}},\vec{g}_{\mathrm{cr}})\; n(m,\vec{r},t)\;. \end{aligned} \tag{4.32}$$

Equation (4.32) is a coagulation equation describing the evolution of the mass spectrum in time when the considered dynamical regimes include coagulation and restitution. In the asymptotic limit of $\vec{g}_{\mathrm{cr}} \longrightarrow 0$ the dynamical regime will denote restitution alone. Then, the coagulation equation reduces to $\partial/\partial t\; n(M,\vec{r},t) = 0$ as obviously no mass changes are to be expected. The opposite limit case of $\vec{g}_{\mathrm{cr}} \longrightarrow \infty$ results in a simplified coagulation equation referring to coagulation alone. It is identical to the *Smoluchowski* equation and is discussed in the next section.

4.2.3 The *Smoluchowski* Equation

If any possible collision leads to coagulation, the velocity phase space is not reduced at all. The correction factor (either Eq. (4.29) or (4.30)) becomes unity $\tilde{\mathcal{C}} \longrightarrow 1$ as shown in Eq. (4.31) and illustrated in Fig. 4.2. Coagulation alone is the only possible collisional outcome. Equation (4.32) then reduces to

$$\begin{aligned}\frac{\partial}{\partial t}\, n(M,\vec{r},t) \;&=\; \frac{1}{2}\int_{0}^{M} \mathrm{d}m\, \frac{\sigma\,(v_{\mathrm{th}}^{\mathcal{G}})}{\sqrt{\pi}}\; n(m,\vec{r},t)\; n(M-m,\vec{r},t) \\ &\quad - n(M,\vec{r},t)\int_{0}^{\infty} \mathrm{d}m\, \frac{\sigma\,(v_{\mathrm{th}}^{\mathcal{L}})}{\sqrt{\pi}}\; n(m,\vec{r},t)\;. \end{aligned} \tag{4.33}$$

This equation has otherwise been stated in a phenomenological way and is also known as the *Smoluchowski* equation (Smoluchowski, 1916; Chandrasekhar, 1943). However, as shown above, it is possible to analytically derive this equation from basic principles[6].

Apart from more general assumptions in terms of kinetic theory as the *Stoßzahlansatz*, the molecular chaos assumption, and the low density assumption which have been listed in Sec. 4.1.1, additional restrictions have to be applied in order to reproduce Eq. (4.33). They

---

[6] In analogy to the derivation of the coagulation equation, the *Boltzmann* equation can be reproduced using Eqs. (4.5) and (4.11).

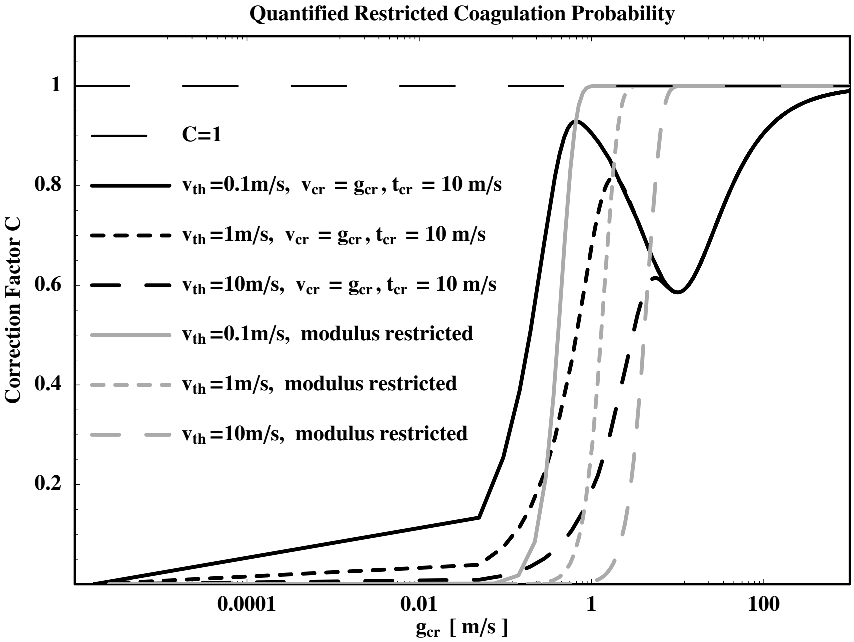

Figure 4.2: Quantified correction factor for different thermal velocities as a function of the critical impact velocity $g_{\rm cr}$. Results are computed according to either Eq. (4.29) (black lines) or Eq. (4.30) (gray lines). $g_{\rm cr}$ denotes the normal critical impact speed $v_{\rm cr}$ for the first and the absolute critical impact speed $|\vec{g}_{\rm cr}|$ for the latter. A critical tangential $t_{\rm cr}$ is fixed as $t_{\rm cr} = 10$ m s^{-1} for illustration. The introduction of a critical velocity and thus a restricted coagulation domain clearly leads to a sharp transition from restitution to coagulation. The larger the critical velocity, the broader the coagulation domain becomes implying an increasing $\mathcal{C}$. Eventually, $\mathcal{C} \rightarrow 1$ for $g_{\rm cr} \rightarrow \infty$ denoting the *Smoluchowski* limit case of $\mathcal{C} = 1$.

mainly denote simplifications made beforehand in order to proceed analytically. Nevertheless, these are not only necessary for reproducing but in turn are to be kept in mind while applying or adopting the *Smoluchowski* equation. Thus, systems described by Eq. (4.33) implicitly obey the following:

- **separable distribution function** $F(\vec{x},t)$ according to Eq. (4.17)
- coagulation probability reaches unity implying **sticking upon every contact**
- **well-defined velocity distributions**, here *Maxwellians*, and **energy equipartition** Note, that in general all well-defined velocity distributions yield a similar result. Such may e.g. be *Rayleigh* or three-axial *Gaussian* distributions.

Equation (4.33), and thus the *Smoluchowski* equation, is widely used in terms of molecular dynamics (Ernst et al., 1984). Most of the equations applied are *Smoluchowski*-type equations. They only differ in the mass dependence of the kernel $K(m_1,m_2)$. Although analytical solutions can be obtained (Safronov, 1969; Trubnikov, 1971; Silk and Takahashi, 1979; Wetherill, 1990) these equations are mainly solved numerically. For a detailed review on aggregation processes see Leyvraz (2003).

4.3 Numerical simulations

In order to quantify analytical results of the previous sections numerical simulations are needed. In order to implement an integro-differential equation as Eq. (4.32) numerically, continuous equations alike are discretized thereby assuring conservation principles. Here, the conservation of total mass is the only conservation principle mandatory to account for. A minimum $m_{\min}$ and maximum mass $m_{\max}$ are introduced while discretizing the mass spectrum itself. Two different approaches can generally be taken in order to assign a certain mass bin. Moving "batches" or bins may be introduced as in Wetherill and Stewart (1993). There, the mass of each according bin is not fixed but varied appropriately to match mass conservation. In contrast to the previous method, we use fixed mass bins while mass conservation is accounted for by the discretized coagulation equation. A brief description of the discretization can be found in Appendix B.

In general, discrete time t and mass m are introduced as independent variables. A discrete mass spectrum of 200 mass bins ranges between $m_{\min} = 10^{-9}$ kg and $m_{\max} = 10^{6}$ kg for corresponding sizes of $r_{\min} = 0.1$ mm and $r_{\max} = 10$ m. Bins are equidistantly distributed on a logarithmic scale. Approximately 5000 adaptive time steps within the interval of $t \in [0, 10^{12}]$ s ≈ 31710 years are chosen for each simulation. Mass gain and loss in a single bin is restricted to a fixed percentage of current content of the corresponding bin, respectively. Since there is no explicit time dependence in the coagulation equation, this requirement determines the adopted time step Δt_{i}. Values $n(m,t)$ smaller than $10^{-20}\max[n(m,t)]$ at given time t are considered as zero. The numerical code was tested using initial conditions and analytical solutions of the *Smoluchowski* equation derived by Silk and Takahashi (1979) and Trubnikov (1971), and were in good agreement as shown below. The latter case investigates an integration kernel of the form $K(m_1,m_2) = m_1 + m_2$ and its analytical and numerical solution using Eq. (4.33) and (Trubnikov, 1971, their Eq. (31)) of the number density per unit mass $n(m,t)$ is shown in Fig. 4.3 as a function of mass m. Mass changes in specific bins are restricted to 5% and 0.15% for gain and loss, respectively. Numerical results and analytical solution show a good agreement.

An initial distribution of the form $n(m,t=0) = C_0\ m\ \exp[-C_1 m]$, where C_0 and C_1 are constants, is taken as provided in Silk and Takahashi (1979, p. 244 (ii)). The initial particle number density is obtained by an Earth mass evenly spread in a circumsolar disk with a semi-opening angle of 3 degrees placed in between Venus and Mars. In this case a lower accuracy was sufficient and gain and loss restrictions are merely 50% and 25% respectively. A good agreement has been reached as shown in Fig. 4.4. Deviations for the lower part of the distribution function from the analytical solution arise for three reasons. First, it denotes an approximative solution for a power-law kernel $W \sim m_1^{\lambda/2}\ m_2^{\lambda/2} (\lambda = 1/6)$, with *Dirac*'s delta function as initial condition and $\mathcal{C} = 1$. Nevertheless, the agreement further validates the numerical code and gives analytic tools to study unrestricted growth in time $(\mathcal{C} \to 1)$. Thus, numerically solving the *Smoluchowski* equation, Eq. (4.33), for a total mass $M_{\mathrm{tot}} = M_{\mathrm{Earth}}$ and a characteristic values $v_{\mathrm{char}} = 1\ \mathrm{m\,s^{-1}}$ and $R_{\mathrm{char}} = 1$ cm, yields results shown in Fig. 4.4. In case of $\mathcal{C} = 1$, the *Smoluchowski* limit case, the mean mass $\langle m \rangle$ of the ensemble is steadily increasing. Growth will effectively continue until all available grains have coagulated into one single, big body of mass $\langle m \rangle = M_{\mathrm{tot}}$. The shape of the distribution function itself is perfectly self-similar and literally merely shifted through the mass spectrum. Growth occurs homogeneously and the creation of larger bodies is just a matter of time. This perfectly demonstrates a *Smoluchowski*-type ensemble evolution.

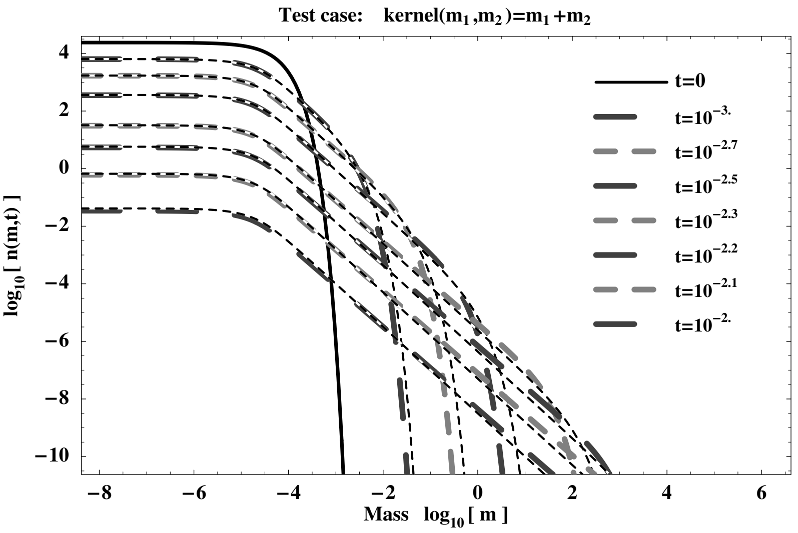

Figure 4.3: Solution of the *Smoluchowski* equation, Eq. (4.33), for initial condition and analytical solution as provided in Trubnikov (1971). The number density per unit mass $n(m,t)$ is plotted at different time steps as function of mass m. Thick gray long-dashed lines denote the simulation results while thinner black dashed lines show the analytical solution at according time steps. In this test case, units are arbitrary.

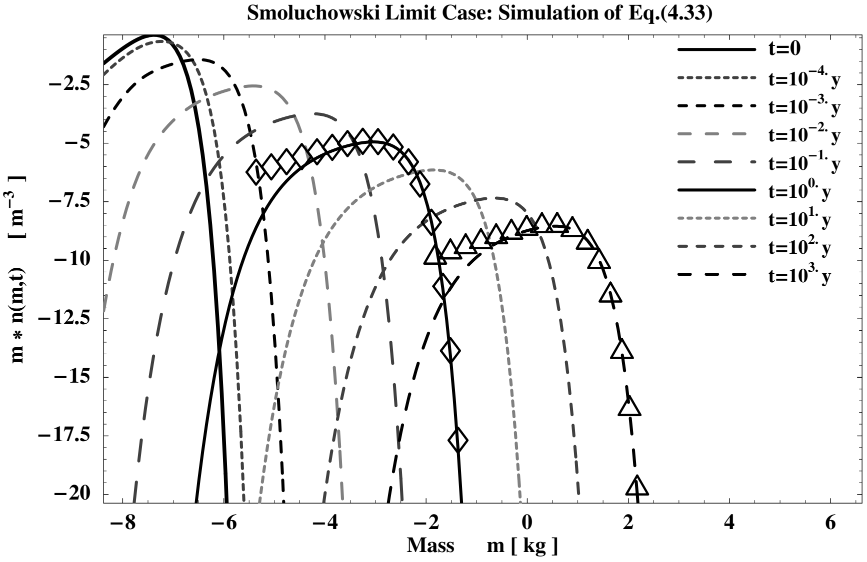

Figure 4.4: Solution of Eq. (4.33) using initial conditions as provided in Silk and Takahashi (1979) for a total mass $M_{\rm tot}$ of Earth and a thermal velocity $v_{\rm th} = 1\ {\rm m\,s^{-1}}$ of centimeter sized grains. The mass spectrum $m\ n(m,t)$ is plotted for different time steps up to 3000 years. A solid line denotes the initial condition $n(m,t=0)$. As time is passing grains continuously coagulate resulting in a steadily increasing mean mass $\langle m \rangle$. Growth will effectively continue until all available grains have coagulated into one single, big body of mass $m = M_{\rm tot}$. This perfectly demonstrates the essence of *Smoluchowski*-type ensemble evolution.

Using initial settings as for the comparison to Silk and Takahashi (1979), numerical integrations of different collision scenarios are performed. Thermal velocities $v_{\rm th}$, are fixed in every simulation since Eq. (4.32) describes a thermalized ensemble. They denote the granular temperature T of the system which is attributed by a characteristic particle size $R_{\rm char}$ and velocity $v_{\rm char}$ as $T = 3\, m_{\rm char} v_{\rm char}^2/2$ where $m_{\rm char}$ is the corresponding characteristic mass. Characteristic sizes are fixed to centimeter sized grains and velocities are chosen out of $v_{\rm char} \in [0.1, 1.0, 10.0]\ {\rm m\,s^{-1}}$. Thermal velocities exemplary illustrated in Fig. 4.5.Critical velocities have been obtained in analytical (Dominik and Tielens, 1997; Brilliantov and Poeschel, 2005) and numerical studies (Spahn et al., 2004; Albers and Spahn, 2006) and may simply be applied here (cf. Chapter 2). Larger critical velocities allow for broader coagulation domains as shown in Fig. 4.2. Thus, possible impact speeds of two grains leading to coagulation range from 0 to $g_{\rm cr}$. However, $g_{\rm cr}$ itself is determined by the masses of the same two grains and varies for each possible pair of colliding masses.

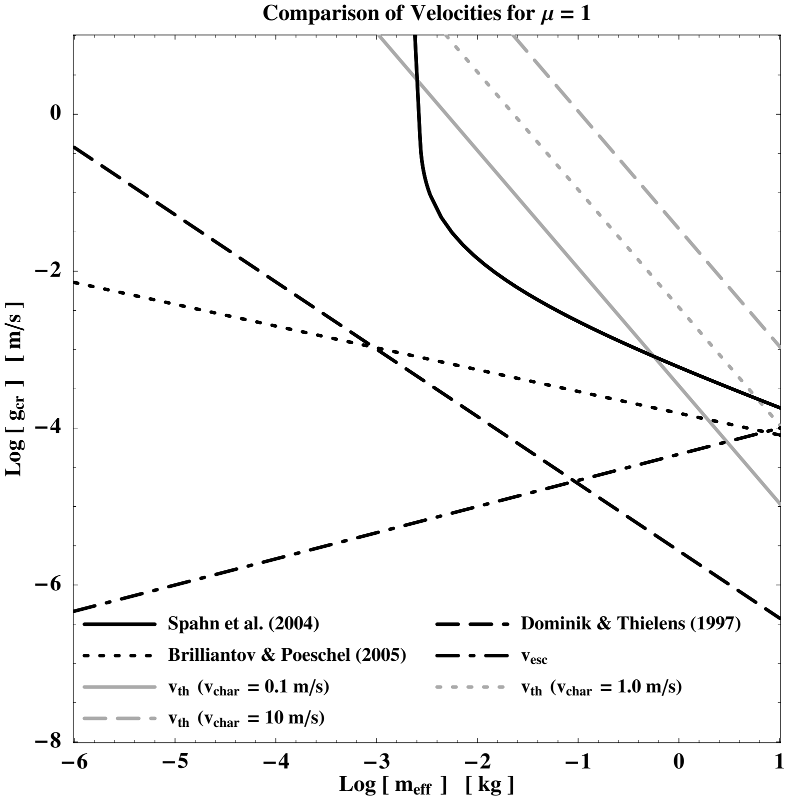

Figure 4.5: Critical velocities $g_{\rm cr}$ in comparison with the two-body escape velocity $v_{\rm esc}$ and thermal velocities $v_{\rm th}$ corresponding to different characteristic values $v_{\rm char}$ (according to $T = 3\ m_{\rm char}\ v_{\rm char}^2/2$ and $T = m_{\rm eff}\ v_{\rm th}^2/2$ with $R_{\rm char} = 1$ cm). While the escape velocity is increasing with larger mass, critical velocities are generally decreasing. Dominik and Tielens (1997, Eq. (9)) and Brilliantov and Poeschel (2005, Eq. (8.101)) obtained critical velocities in form of power-laws. The critical velocity obtained in Chapter 2 clearly differs from the previous two. Although being approximated for higher masses by a power-law (Spahn et al., 2004, Eq.(11)), $g_{\rm cr}$ exponentially approaches infinity for smaller grains. Thus, $g_{\rm cr} > v_{\rm th}$ for smaller grains and denotes the necessary condition to allow for coagulation in a thermalized ensemble. All critical velocities shown are either analytically or numerically obtained. To our knowledge of the current literature, detailed measurements of the mass-dependent $g_{\rm cr}$ are still missing.

The above mentioned different scenarios are accounted for by different integral kernels $K(m_1,m_2) = \sigma v_{\mathrm{th}} C(v_{\mathrm{th}},\vec{g}_{\mathrm{cr}})/\sqrt{\pi}$, cf. Eq. (4.32). Although clearly velocity dependent are merely functions of two interacting masses, m_1 and m_2. Their mass dependence $K(m_1,m_2)$ is further qualified by different correction factors $\mathcal{C}(m_1,m_2) = C(v_{\mathrm{th}},\vec{g}_{\mathrm{cr}}(m_1,m_2))$ arising from different domains $\mathcal{D}_{\mathrm{c}}$ and thus $g_{\mathrm{cr}}(m_1,m_2)$. At this point, we will concentrate on three major cases as there are: *(a)* $\mathcal{C} = 1$ as the *Smoluchowski* limit, *(b)* $\mathcal{C}$ according to Eq. (4.29), and *(c)* $\mathcal{C}$ according to Eq. (4.30) as examples for a restricted coagulation.

Covering mass ranges from m_{min} to m_{max} the three integration kernel $K(m_1,m_2)$ are shown in Fig. 4.6 for a characteristic velocity of $v_{\mathrm{char}} = 1\ \mathrm{m\,s^{-1}}$ of centimeter sized grains. The trivial case of $\mathcal{C} = 1$ (*Smoluchowski* limit) denotes a coagulating event at any given contact of any m_1 and m_2 but has not been illustrated. The left and right part of Fig. 4.6 denote cases of restricted coagulation clearly indicated by dark regions. The left part of Fig. 4.6 shows the integration kernel $K(m_1,m_2)$ where the critical velocity is defined as the maximum of the two-body escape v_{esc} and absolute critical impact speed g_{cr} obtained as v_{cr} in Chapter 2. Using Eq. (4.30) grains heavier than 1 g almost do not coagulate. Only larger ones with more than 100 kg are again able to noticeably influence each other for $\mu = 1$ due to their mutual gravity (v_{esc}). Smaller ones may always stick to larger ones. However, a "gap" exists for intermediate sized grains. The right part of Fig. 4.6 shows the influence of a tangential critical velocity t_{cr} besides the normal one v_{cr}. Although the rotational degrees of freedom are not accounted for within this context, we assume an estimate of t_{cr} from a very basic consideration. Let us assume a complete transformation of relative tangential kinetic energy $E_{\mathrm{t}} = m_{\mathrm{eff}} {v_{\mathrm{t}}}^2/2$ into rotational energy of two grains rotating around each other with respect to their common center of mass. Then, there exists a maximum spin of the agglomerate when the sticking bond F_{ad} according to Eq. (2.30) outbalances centrifugal forces. If the grains rotate faster, the sticking bond will be broken. Finding this maximum rotation frequency gives a maximum tangential impact speed $v_{\mathrm{T}}^{\mathrm{max}} = t_{\mathrm{cr}}$. Here, neither gravitational influences in form of v_{esc} nor mutual attraction of grains are considered. The general behavior of $K(m_1,m_2)$ remains similar although coagulation probabilities are generally higher than before. A belt of coagulation can be found for masses between $10^{-4.5}$ and 10^{-3} kg. An additional region of less likely coagulation appears for smaller grains of almost equal size. Agglomerates are more stable for smaller grains resting on larger ones ($\mu \neq 1$ and cf. Eq. (2.30)) and are likely to withstand inertia forces. Naturally, domains are symmetric with respect to an exchange of particles and thus a reflexion along the diagonal where $m_1 = m_2$. A symmetric kernel $K(m_1,m_2)$ is mandatory in order to conserve the mass in the coagulation equation.

But different from growth processes predicted by the *Smoluchowski* equation as shown above, a restricted coagulation domains leads to inhibited growth. The numerical integration of Eq. (4.32) using Eq. (4.30) with respect to the mass spectrum is shown in Fig. 4.7 for different time steps up to 4000 years. Initial particle density and thermal velocity are chosen as in the previous case. Using the critical velocity obtained in Chapter 2 (cf. Fig. 2.8) for parameters roughly those of ice at low temperatures, the initial stages are exactly the same as for $\mathcal{C} = 1$. Grains stick at any given contact and growth steadily continues. The mean mass $\langle m \rangle$ continuously increases until a certain size is reached and the evolution of the mass spectrum comes to a halt. At that point, the distribution function $n(m,t)$ becomes narrower and constituents simply "pile" up in a small range of masses. Growth is further on inhibited and does not continue beyond this certain threshold mass or size. Coagulation probability is effectively zero and the entire system is frozen in an almost steady-state. Even if the sim-

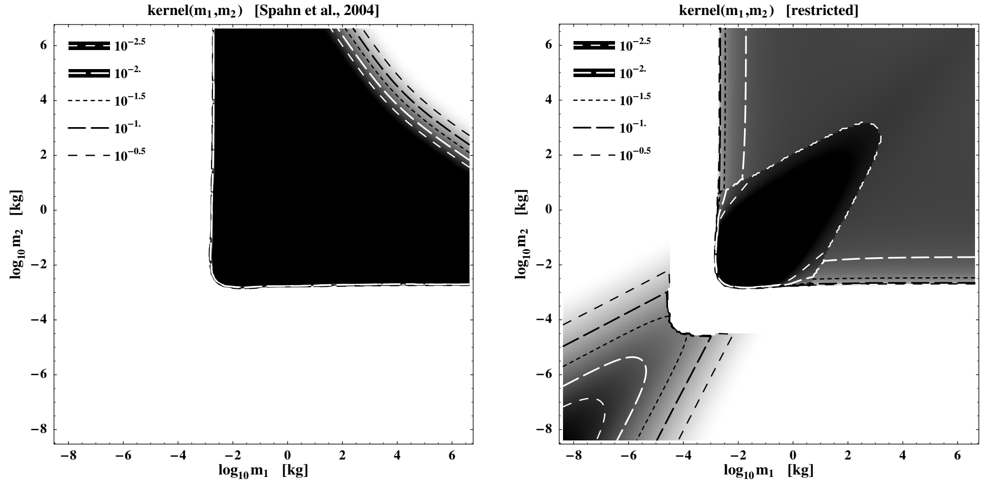

Figure 4.6: Integration ranges for masses used in numerical simulations. The same gray scales are applied in all subfigures. White regions denote areas of high coagulation probability while darker ones indicate less likely coagulating collisions. In all cases, the thermal velocity is chosen as $v_{\text{th}} = 0.1$ m s^{-1}. Domains are symmetric with respect to an exchange of particles and thus a reflexion along the diagonal where $m_1 = m_2$. *Left part:* Restricted coagulation using $\mathcal{C}$ according to Eq. (4.30) plus effects of gravitational captures accounted for in terms of escape velocity v_{esc}. *Right part:* Restricted coagulation using $\mathcal{C}$ according to Eq. (4.29) where a normal v_{cr} and tangential critical velocity t_{cr} is applied.

ulation is continued beyond 3000 years no significant growth can be observed. No larger bodies will form and the maximum grain size will be within centimeters. The particular critical size is determined by the ratio of g_{cr} and v_{th}. Coagulation can still take place, but the growth rate is enormously decreased.

On the other hand, solving Eq. (4.32) using Eq. (4.29) while applying the same initial conditions and parameters as above yields results presented in Fig. 4.8. Results obtained in Chapter 2 with respect to the critical velocity are taken as a normal critical impact speed $g_{\text{cr}} = v_{\text{cr}}$ since the presented collision dynamics covered the normal component only. However, Eq. (4.29) accounts for a tangential cut-off speed as well. It can be estimated by a maximum spin of the agglomerate as explained before. Applying these two critical velocities, the evolution of the mass distribution is shown up to 3000 years and generally shows the same features as those in Fig. 4.7. The evolution starts slower than the one where only the absolute value of the impact speed is restricted (cf. Fig. 4.7). The distribution function further on develops a second peak as $\mu = 1$, i.e. same sized bodies, are not favored to coalesce (Fig. 4.6 exemplifies this). Thus a part of the ensemble experiences a delayed evolution. However, reaching the critical grains size the distribution “piles” up and the second peak follows in line. Although growth is more irregular for two restrictive components the overall outcome is the same. Reaching a certain critical grain size of about centimeter sized grains, effective growth ceases. Even longer simulation times do not result in any further growth. The main aspect, as before, is that the evolution of the mass distribution comes to a halt and no larger bodies can form in this process of pure coagulation.

The character of obtained solutions is insensible to changes of the initial conditions. While collision frequency and growth rate do change, time is scalable in terms of the disk param-

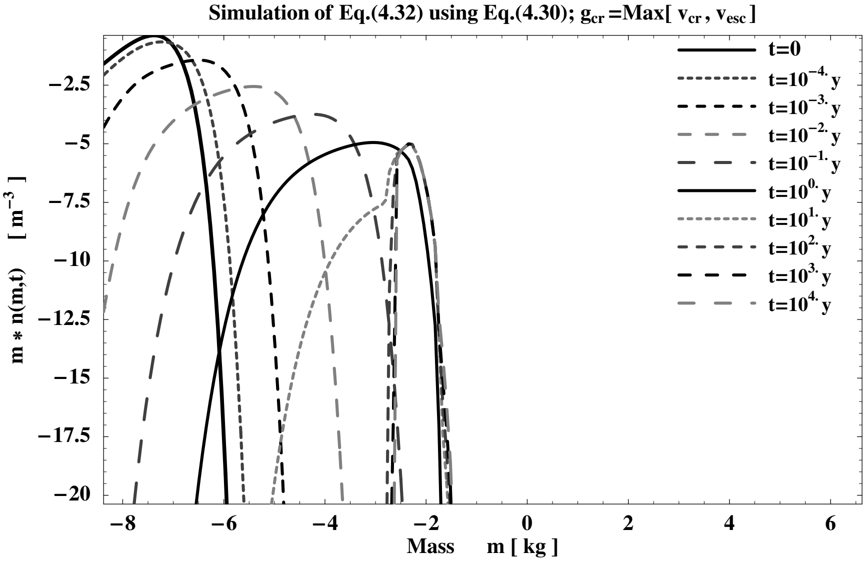

Figure 4.7: Solution of Eq. (4.32) using Eq. (4.30) while applying the same initial condition $n(m,t=0)$ and parameters as in Fig. 4.4. The used critical velocity has been obtained in Chapter 2 (cf. Fig. 2.8) and is given in Fig. 4.5 for comparison. g_{cr} is then applied as a cut-off for the absolute value of relative impact speed. The mass distribution is plotted for different time steps up to 4000 years. After a couple of years of *Smoluchowski*-like continuous growth, the evolution of the mass spectrum comes to a halt. At an average size of merely cm-sized grains, particles do not coagulate anymore. Coagulation probability is effectively zero, thereby "freezing" the entire system. An almost steady-state has been reached. No larger bodies will form, even if the simulation is continued in time. Note that this is not a result of a balanced equilibrium between erosive and agglomerating processes.

eters. In general, the result of the numerical solutions is unsurprisingly coagulation that evolves to higher masses during time. In Fig. 4.9 the mass distribution for different time steps according Eqs. (4.32) and (4.30) is shown (black lines) and compared to results obtained using $C=1$ (Eq. (4.31) and the *Smoluchowski* equation (gray lines). This is basically a direct comparison of Figs. 4.4 and 4.7 where in the first case, the ensemble's mean mass is continuously growing in time, and in the latter the growth stops after a time which depends on the ratio of g_{cr} and v_{th}. By then smaller grains will have coagulated into or onto larger ones. Nevertheless, grain size did not exceed centimeters and these particles never reached the point where their mutual gravitational influence could significantly contribute. For the thermal velocity we used $v_{\mathrm{th}} = 1\ \mathrm{m\,s^{-1}}$ for 1 cm particles as given in Colwell and Taylor (1999) for the sake of possible astrophysical applications. All simulations are initiated from the same initial distribution. It is clearly visible that up to 10^7 s growth evolves in the exact same manner for $\mathcal{C} \to 1$ and $\mathcal{C}(g_{\mathrm{cr}}, v_{\mathrm{th}})$. After that for $\mathcal{C}(g_{\mathrm{cr}}, v_{\mathrm{th}})$ the creation of larger bodies is prevented while the width of the distribution decreases. Thus, due to the restricted coagulation an approximately monodisperse distribution establishes. The diamonds in Fig. 4.9 represent an approximate asymptotic analytical solution (Silk and Takahashi, 1979) for a power-law kernel $W \sim m_1^{\lambda/2}\, m_2^{\lambda/2} (\lambda = 1/6)$, with *Dirac*'s delta function as the initial condition and $\mathcal{C} = 1$. The differences in lower masses arise due to the assumed power-law kernel and initial delta-function. Nevertheless, the agreement further validates our numerical code and gives analytic tools to study unrestricted growth in time $(\mathcal{C} \to 1)$.

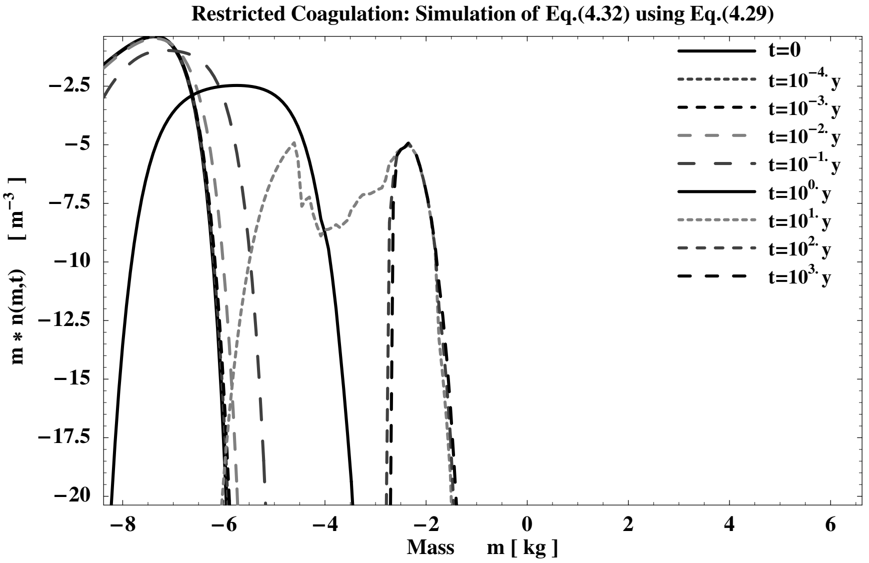

Figure 4.8: Solution of Eq. (4.32) using Eq. (4.29) while applying the same initial condition $n(m,t=0)$ and parameters as in Fig. 4.4. The mass spectrum $m\,n(m,t)$ is plotted for different time steps up to 3000 years. Although growth is more irregular than in case of Eq. (4.30) a critical mass is reached as in Fig. 4.7.

The growth rate is obtained as $\langle m\rangle \sim \rho^{6/5}T^{3/5}t^{6/5}$ where ρ is the disk mass density ($\rho = \int \mathrm{d}m\, m\, n(m)$) and T the granular temperature. Figure 4.10 shows $\langle m\rangle$ as a function of time for different granular temperatures $T \sim v_{\mathrm{th}}^2$ and g_{cr}, obtained from simulations with $\mathcal{C} = 1$ and $\mathcal{C}(g_{\mathrm{cr}}, v_{\mathrm{th}})$. In the latter case, the growth can again be restored, but at a slower rate. Variations of v_{th} also shift the onset of laggard growth. As long as $v_{\mathrm{th}} > g_{\mathrm{cr}}$ holds, the growth process will be inhibited in its evolution. To provoke a case of perfect coalescence the thermal velocity and thus the granular temperature has to be small enough, implying a dynamically cold ensemble. Since g_{cr} is a material-dependent quantity, perfect coalescence cannot be obtained for thermal velocities applied here. In case of silicates, ice, or metal-rock composites g_{cr} remains fairly small.

4.4 Summary and Conclusions

In this chapter a self-consistent treatment of mass, spatial, and velocity distribution in terms of a general kinetic concept is introduced. All possible outcomes of a binary, physical collision are incorporated and denote coagulation, restitution, and fragmentation. They can be understood as domains in a parameter space of mass and impact velocity as was shown in Fig. 4.1. These domains are defined by mass dependent critical impact speed for either restitution or fragmentation to occur, which merely represent input parameters to the kinetic description. Thus, these dynamical domains can naturally be described as coexisting regimes. Separating coagulation from restitution, the critical velocity obtained in Chapter 2 for icy grains has been applied. Coagulation has been emphasized as adhesive particle interaction denote the main subject of study. Fragmentation may be accounted for by denoting a critical speed for fragmentation to occur and a preferred size and velocity distribution function for the debris. A further generalization and thus future perspective could be the combined description of fragmentation and coagulation.

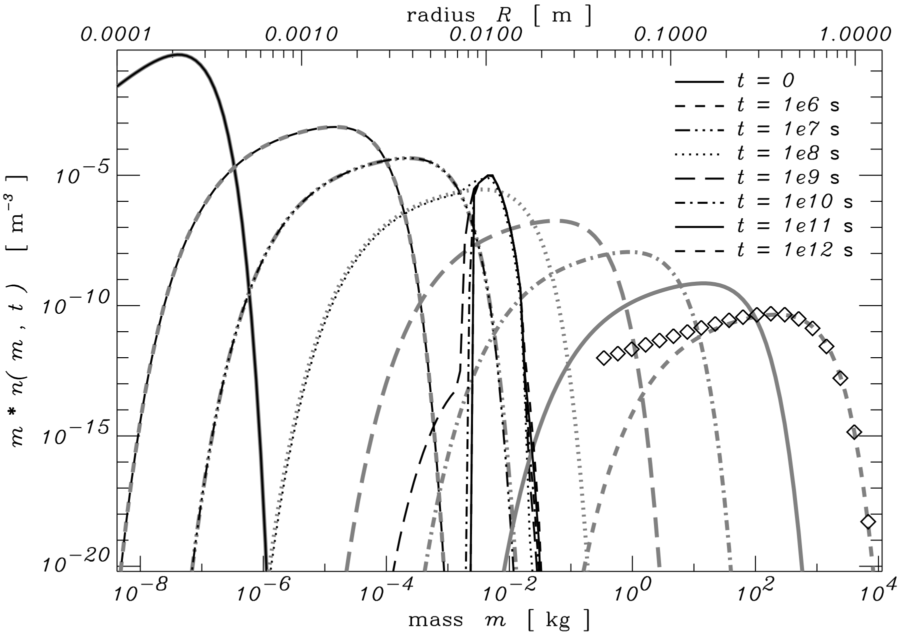

Figure 4.9: The time evolution of the mass spectrum $m\,n(m,t)$ in case of $\mathcal{C} = 1$ (gray lines) and $\mathcal{C}(g_{\mathrm{cr}}, v_{\mathrm{th}})$ according to Eq. (4.30) (black lines), where $v_{\mathrm{th}} = 1\ \mathrm{m\,s^{-1}}$ and a characteristic grain size of $R_{\mathrm{char}} = 1$ cm. Any pair of graphs refers to a distinct time step. Snapshots in time are taken for each elapsed order of magnitude, showing a perfect match to a *Smoluchowski* evolution at the beginning but a drastic difference for later stages. The diamonds in Fig. 4.9 represent an approximate asymptotic analytical solution (Silk and Takahashi, 1979) for a power-law kernel $W \sim m_1^{\lambda/2}\, m_2^{\lambda/2} (\lambda = 1/6)$, with *Dirac*'s delta function as the initial condition and $\mathcal{C} = 1$.

Concentrating on the evolution of the mass distribution a general coagulation equation has been derived. It may partially account for long-range interactions and implicitly includes restitution as well. A correction factor $\mathcal{C}$ to the probability of physical agglomeration has been found to account for reduced coagulation. Besides commonly used assumptions in the context of kinetic descriptions as the *Stoßzahlansatz*, separable generalized distribution function, and molecular chaos and low-density assumptions, *Maxwellian* velocity distributions are assumed in order to allow for an analytical treatment. Furthermore, energy equipartition is assumed. Despite knowing that these assumption are rather restrictive for a general discussion, the otherwise phenomenological *Smoluchowski* equation has been reproduced. It denotes a limit case of $\mathcal{C} \to 1$ and implies coagulation at any possible contact. However, assumptions made in order to derive this equation are, on the other hand, conditions that a system of application has to fulfill.

In the limit of this study, only spherical particles and effective coagulation rather than agglomeration have been assumed for the sake of simplicity. Agglomeration and thus a growth of fractal shaped bodies (Kempf et al., 1999) can be accounted for by $m \sim R^{D_{\mathrm{f}}}$ were D_{f} denotes the fractal dimension. Rotational degrees of freedom are generally treatable in the same manner but would significantly increase the complexity of the problem.

Numerical simulations of the full coagulation equation, Eq. (4.32) in Sec. 4.3, lead to the conclusion that considering coagulation alone while starting with an ensemble of smaller

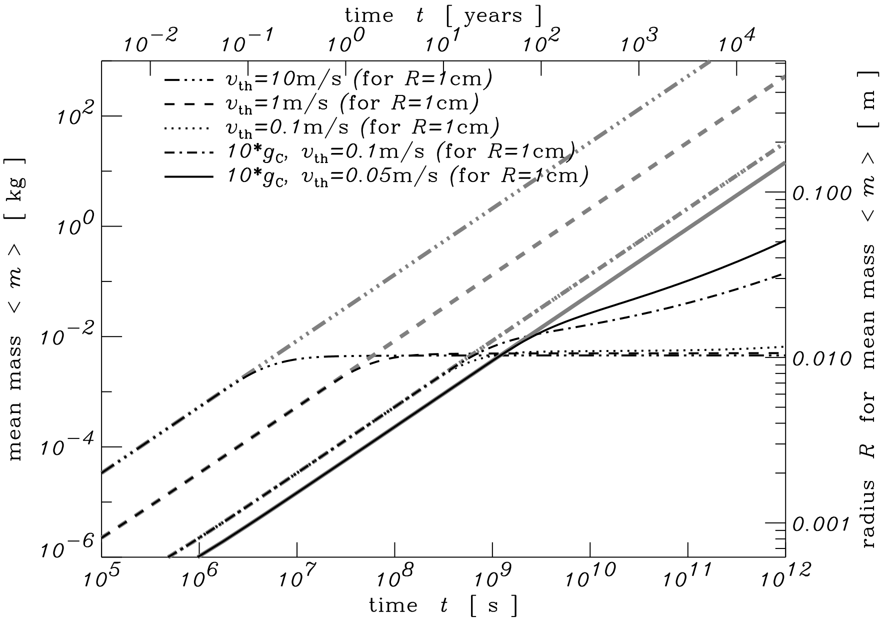

Figure 4.10: The evolution of the mean mass $\langle m \rangle$ in time is shown as black thin lines for different ratios of g_{cr} and v_{th}. The influence of thermal velocity v_{th} and threshold velocity g_{cr} is demonstrated. Gray curves denote the evolution of the mass spectrum according to the *Smoluchowski* equation, Eq. (4.33). Whenever $v_{\mathrm{th}} \gg_{\mathrm{cr}}$ the growth process is almost stopped which implies that it takes aeons for larger bodies to form. With ten times higher g_{cr} (or ten times lower v_{th}) growth can be continued at a slower rate beyond the critical size of 1 cm.

grains does not result in the formation of larger bodies. After a certain time an almost monodisperse mass distribution establishes and very slowly continues to develop in favor of larger bodies. A simple correction for rotational degrees of freedom does not change this rather general result. Changing ensemble parameters such as critical impact speeds or its thermal velocity, and thus its temperature, in a reasonable way does not influence the ceasing growth. Using other estimates of g_{cr} (Dominik and Tielens, 1997; Brilliantov and Poeschel, 2005) which yield yet lower critical velocities (cf. Fig. 4.5), coagulation would stop even earlier. Additionally, if the critical velocity never exceeds the thermal velocity, which applies to all pure power-law solutions of the critical velocity, coagulation does not take place at all. However, changing the parameters to $v_{\mathrm{char}} = 0.05\ \mathrm{m\,s^{-1}}$ and $R_{\mathrm{char}} = 1$ cm while artificially increasing the critical velocity as in Chapter 2 by a factor of ten, the region of ceased growth can be overcome in a reasonable time. Inhibited or laggard growth are inevitable. Furthermore, in the absence of additional physical processes, that could alter the coagulation probability $K(m_1, m_2)$, coagulation alone is not sufficient to produce larger bodies. These results suggest severe implications for the scenario of planetary growth, since and "easy" transition from centimeter-sized particles to planetesimals seemingly does not occur (for parameters used in this study). A constant supply of smaller grains due to fragmenting collisions has been investigated aside, since smaller grains have an effectively higher sticking probability (cf. Chapters 2 and 3). First results of this ongoing study, however, allow for the combined description of fragmentation and coagulation under certain assumptions. No significant growth is found although smaller grains are constantly replenished. Merely an almost steady-state is reached and the coagulation process still ceases at about centimeter sized grains. This is in agreement with other studies who merely employ the *Smoluchowski* equation while feeding smaller grains. They observe a quasi-stationary state Dullemond and Dominik (2005) that in their case slows down the growth which happens to quick compared to timescales appropriate in planet formation. Although the approach of this study is different, we agree on the main observation that fragmentation does neither speed up nor favor growth.

Effects of perturbations such as turbulent velocity fields or the “simple” tracing of granular temperature instead of assuming an average thermal *Brownian* velocity could denote a next step to tackle this problem and investigate to further depth. The existence of an already large body, i.e. approximately 10^3 kg, enabling the possibility of runaway growth (Safronov, 1969) could furthermore resolve this dilemma. Additionally, instabilities such as gravitational instability (Goldreich and Ward, 1973) which would set in at an average size of centimeter-sized grains or vortices in a gaseous disk (Kley et al., 1993) could enforce an ongoing growth beyond the found critical grain size by collective effects. Particles have to grow at least to meter-sized bodies in order to decouple from turbulence (Weidenschilling, 1995). However, at this point, it remains unresolved how larger bodies become to be. Further investigations are mandatory in order to deepen the understanding of restricted growth.

Chapter 5

Summary and Conclusions

The relevance of particle adhesion to the size distribution dynamics of either force-free granular gases or those under the influence of *Keplerian* shear has been studied. This denotes an extension to the otherwise dry granular matter approach. A main application to the presented theoretical models are the planetary rings of Saturn. Generally, implications are given of accretion and growth of larger bodies in accretion disks and planetary rings.

The work presented in this thesis addresses three main aspects:

- **Development of a contact model for low-velocity collisions of adhesive, viscoelastic granular particles.** Based on a static contact model (Johnson et al., 1971), an existing viscoelastic collision model (Brilliantov et al., 1996) has been extended to account for adhesive particle interactions (Spahn et al., 2004; Albers and Spahn, 2006). It allows for agglomeration and restitution which can be distinguished in terms of the restitution coefficient. Furthermore, it provides a size dependent critical velocity which denotes the maximum impact speed at which agglomeration is still possible.

- **Introduction of a self-consistent kinetic concept accounting for agglomeration, restitution, and fragmentation.** A master equation including all three collisional outcomes describes the evolution of mass, spatial, and velocity distribution of an ensemble. In particular, a coagulation equation is derived from basic principles. It covers the evolution of the mass spectrum in coagulation and restitution domains and reproduces the otherwise phenomenological *Smoluchowski* equation as a limit case.

- **Qualitative and quantitative analysis of the relevance of adhesion to the size distribution in force-free ensembles and those under the influence of *Keplerian* shear.** Capture probability, agglomerate stability, and the occurrence of growth are investigated in the context of adhesive interactions. Their impact on agglomerate sizes in planetary rings has been shown (Albers and Spahn, 2006). In contrast to the *Roche* limit, a critical grain size has been obtained for a given orbit location. Numerical simulations of the derived coagulation equation yield maximum grain sizes of about centimeters (Spahn et al., 2004) and thus question the formation of larger bodies.

5.1 Results

A binary contact model for adhesive, viscoelastic collisions has been developed. It's validity within the *quasistatic* approximation restricts impact speeds to below the material's speed of sound and is thus not capable of describing a fragmenting collision. It, however, accounts for agglomeration and restitution and reproduces experimentally observed collision features such as an oscillatory motion during collision, the formation of an inter-particle bond in case of agglomeration, and the overall reduced restitution coefficient compared to purely viscoelastic contact. The model is in agreement with experimental findings for ice at low temperatures and impact speeds up to decimeters per second, suitable for an application to planetary rings, reproduces fairly well measured size and velocity dependences of the normal restitution coefficient ε_{N}. The collisional outcomes are distinguished in terms of ε_{N}. Denoting a complete dissipation of relative kinetic energy, ε_{N} vanishes in case of agglomeration. For impact speeds below $\mathrm{mm\,s^{-1}}$ of centimeter-sized grains, any collision will result in agglomeration. A critical maximal impact velocity for agglomeration to occur has been obtained as a function of the colliding masses. This denotes a single parameter characterizing any impact and thus an essential input parameter allowing for a combined treatment of agglomeration and restitution in terms of kinetic theory.

A self-consistent treatment of mass, spatial, and velocity distribution of an ensemble in terms of kinetic theory has been proposed in this thesis. Since critical velocities, either for agglomeration or for fragmentation to occur, are merely input parameters, the collision model provides a link to treat dynamical regimes in a combined manner. The kinetic model covers agglomeration, restitution, as well as fragmentation. Conservation laws such as the conservation of mass and momentum as well as collision conditions are naturally accounted for in appropriate integral kernels. Emphasizing the evolution of the mass distribution, a coagulation equation has been derived from basic principles. It includes a restricted domain for possible coagulation. The restitution domain is implicitly included, since it does not affect the mass spectrum at all. Fragmentation has been disregarded in order to concentrate on growth processes alone. The otherwise phenomenological *Smoluchowski* equation has been reproduced as a limit case of infinite critical velocity. Solving the full coagulation equation revealed that, contrary to *Smoluchowski* continuous growth, any coagulation ceases if the mean mass of the size distribution reaches about centimeter sized grains. This critical size is determined by the ratio of critical and thermal velocity of the ensemble. Changing this ratio does still not allow for a growth on timescales appropriate for e.g. planet formation.

While probing for the influence of particle adhesion on ensemble dynamics, the orbit evolution of two grains has been studied analytically and numerically under conditions of Saturn's rings. The adhesive bond in case of a two-body agglomerate, together with their gravitational attraction, allows to withstand *Keplerian* shear. A critical radial distance from the central planet has been obtained as a function of the agglomerate size and provides an estimate refining the *Roche* criterion. The *Roche* limit denotes a limit case of the present study in case of large bodies, i.e. in the limit of gravitational interactions alone. In turn, a critical agglomerate size at a given radial distance from the planet has been obtained that provides an upper cut-off of the size distribution. A general trend of increasing particle sizes with increasing distance to Saturn is in agreement with data from the Visual and Infrared Mapping Spectrometer (VIMS) onboard the *Cassini* spacecraft (Planetary Photojournal, JPL, PIA06349).

Furthermore, the two-body capture probability has been obtained as a function of radial distance and particles size with respect to Saturn's rings. If only gravitational interactions and a constant, non-zero coefficient of restitution (contrary to the findings in this thesis) are applied, capture probability is only dependent on the radial distance to the central body. The actual grain or agglomerate size is unimportant, while the size ratio denotes the only important information. Implementing the collision model developed in this thesis results in drastic changes. Despite the first intuition that adhesion increases stability and capture probability in general, this has not been confirmed. A particles size of about 0.5 m denotes a transition size where the capture probability drops by one order of magnitude, leaving larger particles less likely to be caught. In addition, an interesting region is found at about 2.3-2.4 Saturn radii where a "tongue"-like feature of enhanced capture probability coincides with the outer boundary of main rings and the orbit location of the "lively" F ring (Showalter et al., 1992; Barbara and Esposito, 2002; Showalter, 2004; Porco et al., 2005; Murray et al., 2005).

5.2 Limitations

In the line of this work a number of simplifying assumptions are made. Future progress can be achieved by improving various aspects listed below:

- **Grains are assumed as smooth and spherically homogeneous.** Furthermore, two solid grains are assumed to coalesce instead of aggregate in the kinetic approach. However, treating fractal growth in terms of kinetic theory is possible (Kempf et al., 1999). Multiple collisions could prove fatal for growing agglomerates and decrease the likelihood of coagulation. Additionally, surface irregularities could be modeled as random deviations from the surface normal.

- **Contact model allows for low-velocity impacts only.** It's validity is restricted to impact speeds much below the material's speed of sound (*quasistatic* approximation). Crack propagation and eventual break-up of grains cannot be accounted for, at least not in a simple manner.

- **Rotational degrees of freedom of the particles and friction are neglected.** The proposed collision model covers only the normal component of contacts. Collisions are generally assumed as frictionless, i.e. $\varepsilon_T = 1$ for the tangential restitution in particular. Oblique impacts are treated here, but only in the frictionless case. With respect to the kinetic theory, rotational degrees of freedom are neglected due the increasing complexity of the problem.

- **Details of the kinetic concept covers coagulation alone.** Although the proposed kinetic concept covers coagulation, restitution, and fragmentation, the emphasis has been put on the mass distribution dynamics, where fragmentation was disregarded. Provided for a contact model to cover break-ups and debris' size and velocity distribution, fragmentation can be tackled by the presented kinetics. An alternative would be to use phenomenological equations describing the fragment generation, as it has been done by Krivov et al. (e.g. 2005).

Some of above limitations were taken deliberately since the emphasis of this thesis is on adhesion and aggregating or coagulating processes. Thus, they not necessarily denote limitations to the model as such.

5.3 Conclusions and Future Perspectives

This thesis demonstrates the relevance of particle adhesion in physical problems of interest. Even in cases when adhesion does not contribute to effective growth, it strongly influences the dynamics and kinetics of granular gases. Including adhesion denotes a significant extension to dry granular media. Besides a purely theoretical interest, we seek a deeper understanding of structure evolution in granular gases, shaping of planetary rings, and planet formation.

The presented kinetic model incorporates coagulation, restitution, and fragmentation, and seems to be the proper tool to tackle collision-dominated systems. Numerous authors successfully applied kinetic theory to planetary rings (e.g. Goldreich and Tremaine, 1978; Hameen-Anttila, 1978; Araki and Tremaine, 1986; Frezzotti, 2001). Collective effects can be described in a self-consistent way and vivid dynamical processes, as suspected to dominate the F ring of Saturn, could provide an interesting application in order to further test adhesive interactions. Due to the two shepherding moons, Prometheus and Pandora, this region is dynamically complex and far enough from Saturn so that weak tidal stresses promote capture. The *Cassini* mission continues to bring a wealth of data and much more detailed and complex pictures of the F ring is emerging. The time is ripe to extend previous studies (Barbara and Esposito, 2002), utilizing more detailed collision models, including possible adhesion, and spatial and, most importantly, velocity distributions (e.g. Krivov et al., 2005, who used an orbital elements description).

The F ring hosts transient features as brightness fluctuations (Showalter et al., 1992), that could originate either from a population of hidden moonlets or larger chunks in that region (Barbara and Esposito, 2002) or from micrometeoroid impacts (Showalter, 2004). In both cases, regolith would be released on impact. Collision dynamics, agglomerate stability, as well as capture probability, promote the existence of regolith layers varying in thickness according to the size of the underlying body and its radial distance to the central body. Multiple subsequent collisions, that were not considered in context of this study, could shatter these regolith layers, thereby temporarily releasing vast amounts of small particles. Frequent collision could also compactify loose agglomerates. In both cases, future collisions might be more elastic than before. If the mean thickness of the regolith layer depends on the radial orbit location, so does the restitution coefficient. Including adhesion leads to a radial dependence of accretion rate and the maximum size of aggregates.

An application of the kinetic theory with respect to planet formation leads to question the current opinion about the formation of larger bodies. In the absence of gas, adhesion and gravity alone do not provide an effective growth on reasonable timescales to grow planets. According to the restricted coagulation, presented in this thesis, effective growth ceases at an average size of centimeter-sized grains. Even constantly replenishing smaller grains by cratering or fragmenting larger bodies, does not change the result that this is not effective to build larger bodies. It merely leads to a stagnant growth as observed in test cases in this study or applications to *Smoluchowski* growth (Dullemond and Dominik, 2005). In the absence of other physical processes, such as perturbations as e.g. gravitational instabilities (Goldreich and Ward, 1973) or turbulent velocity fields (Sekiya, 1998), the process of planet formation as we understand it today is questionable. Undergoing a purely collisional cascade is apparently not sufficient to create a planet, the link between small bodies and planetesimals being still missing.

Acknowledgments

This work would not have been possible without the help of many people. In particular, I wish to thank:

My supervisor Dr habil Frank Spahn for his support, scientific advises, and the opportunity to work on this topic. I especially acknowledge his flexibility during the final stage of this thesis.

Prof Larry W. Esposito for scientific advises and his warm hospitality during my stay at the University of Colorado at Boulder.

Prof Dr Jürgen Kurths for his support and helpful advises during my years at the University of Potsdam. I thank the AGNLD group for the friendly atmosphere.

Dr Nikolai V. Brilliantov, Marcel Hörning, Martin Makuch, Prof Dr Alexander V. Krivov, Martin Seiß, Dr Jürgen Schmidt, Dr Frank Spahn, and Dr Miodrag Sremčević for interesting discussions at the “Ring”-seminar and the warm ambience. In particular, Dr Miodrag Sremčević for his help and numerous advises while I was acquainting myself with Mathematica.

Martin Makuch and Dr Miodrag Sremčević for their support.

Sandra Zeretzke for her support and various, helpful advises.

Dr Nikolai V. Brilliantov, Dr Jim Howard, Martin Makuch, Dr Jürgen Schmidt, Dr Frank Spahn, and Dr Miodrag Sremčević, for corrections to the manuscript.

Jörg-Uwe Tessmer for his support and maintenance of the computer network.

Birgit Voigt for her friendliness and help in the office.

This work was supported by the STUDIENSTIFTUNG des deutschen Volkes.

Bibliography

Aggarwal, H. R. and Oberbeck, V. R. (1974). Roche Limit of a Solid Body. *Astrophysical Journal*, 191:577–588.

Albers, N. (2002). Collision dynamics of granular particles: Astrophysical applications. Master's thesis, Universität Potsdam.

Albers, N. and Spahn, F. (2005). Saturn's rings. In *Roche Limits and Roche Lobes, in press*.

Albers, N. and Spahn, F. (2006). The influence of particle adhesion on the stability of agglomerates in Saturn's rings. *Icarus*, 181(1):292–301.

Araki, S. and Tremaine, S. (1986). The dynamics of dense particle disks. *Icarus*, 65:83–109.

Attard, P. and Parker, J. L. (1992). Deformation and adhesion of elastic bodies in contact. *Physical Review A: General Physics*, 46:7959–7971.

Barbara, J. M. and Esposito, L. W. (2002). Moonlet Collisions and the Effects of Tidally Modified Accretion in Saturn's F Ring. *Icarus*, 160:161–171.

Barrow, J. D. (1981). Coagulation with fragmentation . *Journal of Physics A Mathematical General*, 14:729–733.

Binney, J. and Tremaine, S. (1987). *Galactic dynamics*. Princeton, NJ, Princeton University Press, 1987, 747 p.

Bishop, J. E. L. and Searle, T. M. (1983). Power-law asymptotic mass distributions for systems of accreting or fragmenting bodies. *Monthly Notices of the Royal Astronomical Society*, 203:987–1009.

Blum, J. and Wurm, G. (2000). Experiments on Sticking, Restructuring, and Fragmentation of Preplanetary Dust Aggregates. *Icarus*, 143:138–146.

Boltzmann, L. (1896). *Vorlesungen über Gastheorie*. Barth, Leipzig.

Bridges, F., Hatzes, A., and Lin, D. (1984). Structure, stability and evolution of Saturn's rings. *Nature*, 309:333–338.

Bridges, F. G., Supulver, K. D., Lin, D. N. C., Knight, R., and Zafra, M. (1996). Energy Loss and Sticking Mechanisms in Particle Aggregation in Planetesimal Formation. *Icarus*, 123:422–435.

Brilliantov, N., Spahn, F., Hertzsch, J.-M., and Pöschel, T. (1996). Model for collisions in granular gases. *Physical Review E: Statistical, Nonlinear, and Soft Matter Physics*, 53(5):5382–5392.

Brilliantov, N. V. and Poeschel, T. (2005). Collision of Adhesive Viscoelastic Particles. *ArXiv Condensed Matter e-prints*.

Burns, J. A. (1999). *Planetary Rings*, pages 221–+. The New Solar System.

Chandrasekhar, S. (1943). Stochastic problems in physics and astronomy. *Review of Modern Physics*, 15:1–89.

Chandrasekhar, S. (1969). *Ellipsoidal figures of equilibrium. The Silliman Foundation Lectures*. Yale University Press, New Haven.

Chapman, S. and Cowling, T. G. (1970). *The Mathematical Theory of Nonuniform Gases*. Cambridge University Press, New York.

Colwell, J. E. and Esposito, L. W. (1992). Origins of the rings of Uranus and Neptune. I - Statistics of satellite disruptions. *Journal of Geophysical Research*, 97:10227–+.

Colwell, J. E. and Esposito, L. W. (1993). Origins of the rings of Uranus and Neptune. II - Initial conditions and ring moon populations. *Journal of Geophysical Research*, 98:7387–7401.

Colwell, J. E., Esposito, L. W., and Bundy, D. (2000). Fragmentation rates of small satellites in the outer solar system. *Journal of Geophysical Research*, 105:17589–17600.

Colwell, J. E. and Taylor, M. (1999). Low-Velocity Microgravity Impact Experiments into Simulated Regolith. *Icarus*, 138:241–248.

Cuzzi, J. N. and Estrada, P. R. (1998). Compositional Evolution of Saturn's Rings Due to Meteoroid Bombardment. *Icarus*, 132:1–35.

Davidsson, B. J. R. (1999). Tidal Splitting and Rotational Breakup of Solid Spheres. *Icarus*, 142:525–535.

Davidsson, B. J. R. (2001). Tidal Splitting and Rotational Breakup of Solid Biaxial Ellipsoids. *Icarus*, 149:375–383.

Dilley, J. and Crawford, D. (1996). Mass dependence of energy loss in collisions of icy spheres: An experimental study. *Journal of Geophysical Research*, 101(.10):9267–9270.

Dilley, J. P. (1993). Energy loss in collisions of icy spheres: Loss mechanism and size-mass dependence. *Icarus*, 105:225–234.

Dobrovolskis, A. R. (1990). Tidal disruption of solid bodies. *Icarus*, 88:24–38.

Dominik, C. and Tielens, A. G. G. M. (1997). The Physics of Dust Coagulation and the Structure of Dust Aggregates in Space. *Astrophysical Journal*, 480:647–672.

Dones, L. (1991). A recent cometary origin for Saturn's rings? *Icarus*, 92:194–203.

Dullemond, C. P. and Dominik, C. (2005). Dust coagulation in protoplanetary disks: A rapid depletion of small grains. *Astronomy and Astrophysics*, 434:971–986.

Durda, D. D., Greenberg, R., and Jedicke, R. (1998). Collisional Models and Scaling Laws: A New Interpretation of the Shape of the Main-Belt Asteroid Size Distribution. *Icarus*, 135:431–440.

Ernst, M. H., Hendriks, E. M., and Leyvraz, F. (1984). Smoluchowski's equation and the θ-exponent for branched polymers. *Journal of Physics A: Mathematical and General*, 17:2137–2144.

Esposito, L. W. (2002). Planetary rings . *Reports of Progress in Physics*, 65:1741–1783.

Esposito, L. W., Colwell, J., and Sremčević, M. (2006). Cassini observations and ring history. EGU Conference.

Family, F., Meakin, P., and Deutch, J. M. (1986). Kinetics of coagulation with fragmentation: Scaling behavior and fluctuations. *Physical Review Letters*, 57:727–730.

French, R. G. and Nicholson, P. D. (2000). Saturn's Rings II. Particle sizes inferred from stellar occultation data. *Icarus*, 145:502–523.

Frezzotti, A. (2001). DSMC simulation of the vertical structure of planetary rings. *Astronomy and Astrophysics*, 380:761–775.

Gan-Mor, S. and Galili, N. (2000). Rheological model of fruit collision with an elastic plate. *Journal of agricultural Engeneering Research*, 75:139–147.

Goldreich, P. and Tremaine, S. D. (1978). The velocity dispersion in Saturn's rings. *Icarus*, 34:227–239.

Goldreich, P. and Ward, W. R. (1973). The Formation of Planetesimals. *Astrophysical Journal*, 183:1051–1062.

Greenberg, R., Hartmann, W. K., Chapman, C. R., and Wacker, J. F. (1978). Planetesimals to planets - Numerical simulation of collisional evolution. *Icarus*, 35:1–26.

Greenwood, J. A. (1997). Adhesion of elastic spheres. *Proceedings of the Royal Society London: A*, 453:1277–1297.

Greenwood, J. A. and Johnson, K. L. (1981). The mechanics of adhesion of viscoelastic solids. *Philosophical Magazine A*, 43:697–711.

Haff, P. K. (1986). A physical picture of kinetic granular fluids. *Journal of Rheology*, 30(5):931–948.

Hameen-Anttila, K. A. (1978). An improved and generalized theory for the collisional evolution of Keplerian systems. *Astrophysics and Space Science*, 58:477–519.

Hamilton, D. P. and Burns, J. A. (1994). Origin of Saturn's E Ring: Self-Sustained, Naturally. *Science*, 264:550–553.

Harris, A. W. (1984). The origin and evolution of planetary rings. In *Planetary Rings*, pages 641–659. University of Arizona Press, Tucson.

Hartmann, W. K. (1978). Planet formation: Mechanism of early growth. *Icarus*, 33:50–61.

Hatzes, A., Bridges, F., Lin, D., and Sachtjen, S. (1991). Coagulation of particles in Saturn‘s rings: Measurements of the cohesive force of water frost. *Icarus*, 89:113–121.

Hatzes, A. P., Bridges, F. G., and Lin, D. N. C. (1988). Collisional properties of ice spheres at low impact velocities. *Monthly Notices of the Royal Astronomical Society*, 231:1091–1115.

Helbing, D. (2001). Traffic and related self-driven many-particle systems. *Reviews Modern Physics*, 73(4):1067–1141.

Hertz, H. (1882). Über die Berührung fester elastischer Körper. *Journal der Reinen Angewandten Physik*, 92:156–171.

Hertzsch, J. (2002). A model for surface effects in slow collisions of icy grains. *Planetary and Space Science*, 50:745–755.

Hertzsch, J.-M., Spahn, F., and Brilliantov, N. V. (1995). On Low-Velocity Collisions of Viscoelastic Particles. *Journal de Physique II*, 5:1725–1738.

Higa, M., Arakawa, M., and Maeno, N. (1998). Size Dependence of Restitution Coefficients of Ice in Relation to Collision Strength. *Icarus*, 133:310–320.

Hill, G. W. (1878). Researches in the lunar theory. *American Journal of Mathematics*, 1:5–26,129–147,245–260.

Horanyi, M., Burns, J. A., and Hamilton, D. P. (1992). The dynamics of Saturn's E ring particles. *Icarus*, 97:248–259.

Hudson, J. A. (1980). *The excitation and propagation of elastic waves*. Cambridge University Press.

Ida, S. and Makino, J. (1992). N-body simulation of gravitational interaction between planetesimals and a protoplanet. I - Velocity distribution of planetesimals. *Icarus*, 96:107–120.

Ida, S. and Nakazawa, K. (1989). Collisional probability of planetesimals revolving in the solar gravitational field. III. *Astronomy and Astrophysics*, 224:303–315.

Ivlev, A. V., Morfill, G. E., and Konopka, U. (2002). Coagulation of Charged Microparticles in Neutral Gas and Charge-Induced Gel Transitions. *Physical Review Letters*, 89(19):195502–+.

Jenkins, J. T. and Richman, M. W. (1985). Kinetic theory for plane flows of a dense gas of identical, rough, inelastic, circular disks. *Physics of Fluids*, 28:3485–3494.

Johnson, J. K. and Greenwood, J. A. (2005). An approximate JKR theory for elliptical contacts. *Journal of Physics D: Applied Physics*.

Johnson, K., Kendall, K., and Roberts, A. (1971). Surface energy and the contact of elastic solids. *Proceedings of the Royal Society London: A*, 324:301–313.

Kempf, S., Pfalzner, S., and Henning, T. K. (1999). N-Particle-Simulations of Dust Growth. I. Growth Driven by Brownian Motion. *Icarus*, 141:388–398.

Kleiber, R. and Glatzel, W. (1999). On the stability of viscous accretion tori. *Monthly Notices of the Royal Astronomical Society*, 303:107–115.

Kley, W., Papaloizou, J. C. B., and Lin, D. N. C. (1993). On the Angular Momentum Transport Associated with Convective Eddies in Accretion Disks. *Astrophysical Journal*, 416:679–+.

Kolvoord, R. A. and Burns, J. A. (1992). Three-dimensional perturbations of particles in a narrow planetary ring. *Icarus*, 95:253–264.

Kolvoord, R. A., Burns, J. A., and Showalter, M. R. (1990). Periodic features in Saturn's F ring - Evidence for nearby moonlets. *Nature*, 345:695–697.

Krivov, A. V. and Hamilton, D. P. (1997). Martian Dust Belts: Waiting for Discovery. *Icarus*, 128:335–353.

Krivov, A. V., Mann, I., and Krivova, N. A. (2000). Size distributions of dust in circumstellar debris discs. *Astronomy and Astrophysics*, 362:1127–1137.

Krivov, A. V., Sremčević, M., and Spahn, F. (2005). Evolution of a Keplerian disk of colliding and fragmenting particles: a kinetic model with application to the Edgeworth-Kuiper belt. *Icarus*, 174:105–134.

Krivov, A. V., Sremčević, M., Spahn, F., Dikarev, V. V., and Kholshevnikov, K. V. (2003). Impact-generated dust clouds around planetary satellites: spherically symmetric case. *Planetary and Space Science*, 51:251–269.

Landau, L. D. and Lifshitz, E. M. (1959). *Course of theoretical physics: Theory of elasticity*. Pergamon Press.

Lee, M. H. (2000). On the Validity of the Coagulation Equation and the Nature of Runaway Growth. *Icarus*, 143:74–86.

Lewis, M. C. and Stewart, G. R. (2000). Collisional Dynamics of Perturbed Planetary Rings. I. *Astronomical Journal*, 120:3295–3310.

Lewis, M. C. and Stewart, G. R. (2005). Expectations for Cassini observations of ring material with nearby moons. *Icarus*, 178:124–143.

Leyvraz, F. (2003). Scaling theory and exactly solved models in the kinetics of irreversible aggregation. *Physics Reports*, 383:95–212.

Lissauer, J. J. (1993). Planet formation. *Annual Review in Astronomy and Astrophysics*, 31:129–174.

Longaretti, P.-Y. (1989). Saturn's main ring particle size distribution - an analytic approach. *Icarus*, 81:51–73.

Lynden-Bell, D. and Pringle, J. E. (1974). The evolution of viscous discs and the origin of the nebular variables. *Monthly Notices of the Royal Astronomical Society*, 168:603–637.

Makuch, M., Brilliantov, N. V., Sremčević, M., Spahn, F., and Krivov, A. V. (2006). Stochastic circumplanetary dynamics of rotating non-spherical dust particles. *Planetary and Space Science*, accepted for publication.

Makuch, M., Krivov, A. V., and Spahn, F. (2005). Long-term dynamical evolution of dusty ejecta from Deimos. *Planetary and Space Science*, 53:357–369.

Mamon, G. A. (1992). Are cluster ellipticals the products of mergers? *Astrophysical Journal Letters*, 401:L3–L6.

Marouf, E. A., Tyler, G. L., Zebker, H. A., Simpson, R. A., and Eshleman, V. R. (1983). Particle size distributions in Saturn's rings from Voyager 1 radio occultation. *Icarus*, 54:189–211.

Menci, N., Cavaliere, A., Fontana, A., Giallongo, E., and Poli, F. (2002). Binary Aggregations in Hierarchical Galaxy Formation: The Evolution of the Galaxy Luminosity Function. *Astrophysical Journal*, 575:18–32.

Morishima, R. and Salo, H. (2004). Spin rates of small moonlets embedded in planetary rings I. Three-body calculations. *Icarus*, 167:330–346.

Muller, V. M., Yushchenko, V. S., and Derjaguin, B. V. (1980). On the influence of molecular forces on the deformation of an elastic sphere and its sticking to a rigid plane. *Journal of Colloid and Interface Science*, 77:91–101.

Murray, C. D., Chavez, C., Beurle, K., Cooper, N., Evans, M. W., Burns, J. A., and Porco, C. C. (2005). How Prometheus creates structure in Saturn's F ring. *Nature*, 437:1326–1329.

Murray, C. D., Gordon, M. K., and Giuliatti Winter, S. M. (1997). Unraveling the Strands of Saturn's F Ring. *Icarus*, 129:304–316.

Nakazawa, K. and Ida, S. (1988). Hill's approximation in the three-body problem. *Progress of Theoretical Physics Supplement*, 96:167–174.

Nakazawa, K., Ida, S., and Nakagawa, Y. (1989). Collisional probability of planetesimals revolving in the solar gravitational field. I - Basic formulation. *Astronomy and Astrophysics*, 220:293–300.

Ohtsuki, K. (1993). Capture probability of colliding planetesimals - Dynamical constraints on accretion of planets, satellites, and ring particles. *Icarus*, 106:228–246.

Ohtsuki, K. (2004). On the rotation of a moonlet embedded in planetary rings. *Icarus*, 172:432–445.

Ohtsuki, K. (2005). Rotation Rates of Particles in Saturn's Rings. *Astrophysical Journal Letters*, 626:L61–L64.

Ohtsuki, K. and Emori, H. (2000). Local N-Body Simulations for the Distribution and Evolution of Particle Velocities in Planetary Rings. *Astronomical Journal*, 119:403–416.

Papaloizou, J. C. B. and Lin, D. N. C. (1989). Nonaxisymmetric instabilities in thin self-gravitating rings and disks. *Astrophysical Journal*, 344:645–668.

Petit, J. M. and Hénon, M. (1986). Satellite encounters. *Icarus*, 66:536–555.

Petit, J.-M. and Henon, M. (1987). A numerical simulation of planetary rings. I - Binary encounters. *Astronomy and Astrophysics*, 173:389–404.

Petzschmann, O., Schwarz, U., Spahn, F., Grebogi, C., and Kurths, J. (1999). Length Scales of Clustering in Granular Gases. *Physical Review Letters*, 82:4819–4822.

Planetary Photojournal (JPL). `http://photojournal.jpl.nasa.gov/catalog/`.

Porco, C. C., Baker, E., Barbara, J., Beurle, K., Brahic, A., Burns, J. A., Charnoz, S., Cooper, N., Dawson, D. D., Del Genio, A. D., Denk, T., Dones, L., Dyudina, U., Evans, M. W., Giese, B., Grazier, K., Helfenstein, P., Ingersoll, A. P., Jacobson, R. A., Johnson, T. V., McEwen, A., Murray, C. D., Neukum, G., Owen, W. M., Perry, J., Roatsch, T., Spitale, J., Squyres, S., Thomas, P., Tiscareno, M., Turtle, E., Vasavada, A. R., Veverka, J., Wagner, R., and West, R. (2005). Cassini Imaging Science: Initial Results on Saturn's Rings and Small Satellites. *Science*, 307:1226–1236.

Poulet, F., Sicardy, B., Dumas, C., Jorda, L., and Tiphène, D. (2000a). The Crossings of Saturn Ring Plane by the Earth in 1995: Ring Thickness. *Icarus*, 145:147–165.

Poulet, F., Sicardy, B., Nicholson, P. D., Karkoschka, E., and Caldwell, J. (2000b). Saturn's Ring-Plane Crossings of August and November 1995: A Model for the New F-Ring Objects. *Icarus*, 144:135–148.

Ramírez, R., Pöschel, T., Brilliantov, N. V., and Schwager, T. (1999). Coefficient of restitution of colliding viscoelastic spheres. *Physical Review E: Statistical, Nonlinear, and Soft Matter Physics*, 60:4465–4472.

Resibois, P. M. V., De Leneer, M., and De Leener, M. (1977). *Classical Kinetic Theory of Fluids*. John Wiley & Sons Inc.

Roche, E. A. (1847). *Académie des Sciences et Lettres de Montpellier. Mémoires de la Section des Sciences*, 1:243–262.

Safronov, V. S. (1969). Evolution of the protoplanetary cloud and the formation of the earth and planets. *Nauka*, NASA TTF-677.

Salo, H. (1987). Numerical simulations of collisions between rotating particles. *Icarus*, 70:37–51.

Salo, H. (1991). Numerical simulations of dense collisional systems. *Icarus*, 90:254–270.

Salo, H. (1995). Simulations of dense planetary rings. III. Self-gravitating identical particles. *Icarus*, 117:287–312.

Salo, H., Karjalainen, R., and French, R. G. (2004). Photometric modeling of Saturn's rings. II. Azimuthal asymmetry in reflected and transmitted light. *Icarus*, 170:70–90.

Salo, H., Schmidt, J., and Spahn, F. (2001). Viscous Overstability in Saturn's B Ring. I. Direct Simulations and Measurement of Transport Coefficients. *Icarus*, 153:295–315.

Savkoor, A. R. and Briggs, G. A. D. (1977). The effect of tangential force on the contact of elastic solids in adhesion. *Proceedings of the Royal Society London: A*, 356:103–114.

Schmidt, J., Salo, H., Petzschmann, O., and Spahn, F. (1999). Vertical distribution of temperature and density in a planetary ring. *Astronomy and Astrophysics*, 345:646–652.

Schmidt, J., Salo, H., Spahn, F., and Petzschmann, O. (2001). Viscous Overstability in Saturn's B-Ring. II. Hydrodynamic Theory and Comparison to Simulations. *Icarus*, 153:316–331.

Schmit, U. and Tscharnuter, W. M. (1995). A fluid dynamical treatment of the common action of self-gravitation, collisions, and rotation in Saturn's B-ring. *Icarus*, 115:304–319.

Schmit, U. and Tscharnuter, W. M. (1999). On the Formation of the Fine-Scale Structure in Saturn's B Ring. *Icarus*, 138:173–187.

Seiß, M., Spahn, F., Sremčević, M., and Salo, H. (2005). Structures induced by small moonlets in Saturn's rings: Implications for the Cassini Mission. *Geophysical Research Letters*, 32:11205–+.

Sekiya, M. (1998). Quasi-Equilibrium Density Distributions of Small Dust Aggregations in the Solar Nebula. *Icarus*, 133:298–309.

Showalter, M. R. (1991). Visual detection of 1981S13, Saturn's eighteenth satellite, and its role in the Encke gap. *Nature*, 351:709–713.

Showalter, M. R. (1998). Detection of Centimeter-Sized Meteoroid Impact Events in Saturn's F Ring. *Science*, 282:1099–+.

Showalter, M. R. (2004). Disentangling Saturn's F Ring. I. Clump orbits and lifetimes. *Icarus*, 171:356–371.

Showalter, M. R., Cuzzi, J. N., and Larson, S. M. (1991). Structure and particle properties of Saturn's E Ring. *Icarus*, 94:451–473.

Showalter, M. R., Cuzzi, J. N., Marouf, E. A., and Esposito, L. W. (1986). Satellite 'wakes' and the orbit of the Encke Gap moonlet. *Icarus*, 66:297–323.

Showalter, M. R. and Nicholson, P. D. (1990). Saturn's rings through a microscope - Particle size constraints from the Voyager PPS scan. *Icarus*, 87:285–306.

Showalter, M. R., Pollack, J. B., Ockert, M. E., Doyle, L. R., and Dalton, J. B. (1992). A photometric study of Saturn's F Ring. *Icarus*, 100:394–411.

Shu, F. H., Dones, L., Lissauer, J. J., Yuan, C., and Cuzzi, J. N. (1985a). Nonlinear spiral density waves - Viscous damping. *Astrophysical Journal*, 299:542–573.

Shu, F. H., Yuan, C., and Lissauer, J. J. (1985b). Nonlinear spiral density waves - an inviscid theory. *Astrophysical Journal*, 291:356–376.

Shukhman, I. G. (1984). Collisional Dynamics of Particles in Saturn's Rings. *Soviet Astronomy*, 28:574–585.

Sicardy, B. (2005). Dynamics and Composition of Rings. *Space Science Reviews*, 116:457–470.

Silk, J. and Takahashi, T. (1979). A statistical model for the initial stellar mass function. *Astrophysical Journal*, 229:242–256.

Smoluchowski, M. (1916). Drei Vorträge über Diffusion, Brownsche Bewegung und Koagulation von Kolloidteilchen. *Physikalische Zeitschrift*, 17:557–585.

Soter, S. (1971). The dust belts of Mars. Report of Center for Radiophysics and Space Research No. 462.

Spahn, F., Albers, N., Hörning, M., Kempf, S., Krivov, A. V., Makuch, M., Schmidt, J., Seiß, M., and Sremčević, M. (2006a). E ring dust sources: Implications from cassini's dust measurements. *Planetary and Space Science*, accepted for publication.

Spahn, F., Albers, N., Sremčević, M., and Thornton, C. (2004). Kinetic description of coagulation and fragmentation in dilute granular particle ensembles. *Europhysics Letters*, 67(4):545–551.

Spahn, F. and Schmidt, J. (2006). Planetary science: Saturn's bared mini-moons. *Nature*, 440:614–615.

Spahn, F., Schmidt, J., Albers, N., Hörning, M., Makuch, M., Seiß, M., Kempf, S., Srama, R., Dikarev, V., Helfert, S., Moragas-Klostermeyer, G., Krivov, A. V., Sremčević, M., Tuzzolino, A. J., Economou, T., and Grün, E. (2006b). Cassini Dust Measurements at Enceladus and Implications for the Origin of the E Ring. *Science*, 311:1416–1418.

Spahn, F. and Sponholz, H. (1989). Existence of moonlets in Saturn's rings inferred from the optical depth profile. *Nature*, 339:607–608.

Spahn, F. and Sremčević, M. (2000). Density patterns induced by small moonlets in Saturn's rings? *Astronomy and Astrophysics*, 358:368–372.

Spahn, F., Thiessenhusen, K.-U., Colwell, J. E., Srama, R., and Grün, E. (1999). Dynamics of dust ejected from Enceladus: Application to the Cassini dust detector. *Journal of Geophysical Research*, 104:24111–24120.

Spahn, F. and Wiebicke, H.-J. (1988). Long-term gravitational influence of moonlets in planetary rings. *Icarus*, 77:124–134.

Sremčević, M., Krivov, A. V., Krüger, H., and Spahn, F. (2005). Impact-generated dust clouds around planetary satellites: model versus Galileo data. *Planetary and Space Science*, 53:625–641.

Sremčević, M., Krivov, A. V., and Spahn, F. (2003). Impact-generated dust clouds around planetary satellites: asymmetry effects. *Planetary and Space Science*, 51:455–471.

Sremčević, M., Spahn, F., and Duschl, W. J. (2002). Density structures in perturbed thin cold discs. *Monthly Notices of the Royal Astronomical Society*, 337:1139–1152.

Stern, S. A. (1995). Collisional Time Scales in the Kuiper Disk and Their Implications. *Astronomical Journal*, 110:856–868.

Stewart, G. R. and Ida, S. (2000). Velocity Evolution of Planetesimals: Unified Analytical Formulas and Comparisons with N-Body Simulations. *Icarus*, 143:28–44.

Stewart, G. R., Lin, D. N. C., and Bodenheimer, P. (1984). Collision-induced transport processes in planetary rings. In Greenberg, R. and Brahic, A., editors, *Planetary Rings*, pages 447–512. University of Arizona Press, Tucson.

Supulver, K. D., Bridges, F. G., and Lin, D. N. C. (1995). The coefficient of restitution of ice particles in glancing collisions: Experimental results for unfrosted surfaces. *Icarus*, 113:188–199.

Supulver, K. D., Bridges, F. G., Tiscareno, S., Lievore, J., and Lin, D. N. C. (1997). The Sticking Properties of Water Frost Produced under Various Ambient Conditions. *Icarus*, 129:539–554.

Thébault, P., Augereau, J. C., and Beust, H. (2003). Dust production from collisions in extrasolar planetary systems. The inner beta Pictoris disc. *Astronomy and Astrophysics*, 408:775–788.

Thornton, C. (1997). Coefficient of restitution for collinear collisions of elastic-perfectly plastic spheres. *Journal of Applied Mechanics*, 64:383–386.

Tiscareno, M. S., Burns, J. A., Hedman, M. M., Porco, C. C., Weiss, J. W., Dones, L., Richardson, D. C., and Murray, C. D. (2006). 100-metre-diameter moonlets in saturn's a ring from observations of "propeller" structures. *Nature*, 440:648–650.

Toomre, A. (1964). On the gravitational stability of a disk of stars. *Astrophysical Journal*, 139:1217–1238.

Tremaine, S. (2003). On the Origin of Irregular Structure in Saturn's Rings. *Astronomical Journal*, 125:894–901.

Trubnikov, B. A. (1971). Solution of the coagulation equations in the case of a bilinear coefficient of adhesion of particles. *Soviet Physics: Doklady*, 16:124–126.

Tschoegl, N. W. (1989). *The phenomenological theory of linear viscoelastic behaviour: An introduction*. Springer Verlag.

Weidenschilling, S. J. (1995). Can gravitation instability form planetesimals? *Icarus*, 116:433–435.

Weidenschilling, S. J., Chapman, C. R., Davis, D. R., and Greenberg, R. (1984). Ring particles. In *Planetary Rings*, pages 367–415. University of Arizona Press, Tucson.

Wetherill, G. W. (1990). Comparison of analytical and physical modeling of planetesimal accumulation. *Icarus*, 88:336–354.

Wetherill, G. W. and Stewart, G. R. (1993). Formation of planetary embryos - Effects of fragmentation, low relative velocity, and independent variation of eccentricity and inclination. *Icarus*, 106:190–+.

Wisdom, J. and Tremaine, S. (1988). Local simulations of planetary rings. *Astronomical Journal*, 95:925–940.

Wolf, D. E., Schreckenberg, M., and Brachem, A., editors (1996). *Traffic and granular flow*. World Scientific, Singapore.

Wurm, G., Paraskov, G., and Krauss, O. (2004). On the Importance of Gas Flow through Porous Bodies for the Formation of Planetesimals. *Astrophysical Journal*, 606:983–987.

Zebker, H. A., Marouf, E. A., and Tyler, G. L. (1985). Saturn's rings - Particle size distributions for thin layer model. *Icarus*, 64:531–548.

Appendix A

Integration with Respect to Relative Velocity while Accounting for a Restricted Volume

The dynamical domains as illustrated in Fig. 4.1 yield a restricted phase space volume of considered velocities. The corresponding equation was introduced in Chapter 4 as Eq. (4.28) and reads

$$\tilde{C}\ (v_{\text{th}}, v_{\text{cr}}, t_{\text{cr}}) \ \equiv\ \tilde{C}\ (v_{\text{th}}, \vec{g}_{\text{cr}}) \ =\ \int\limits_{\mathcal{D}_{\text{c}}} \mathrm{d}^3 g\ |\vec{g}|\ \exp[-\frac{\vec{g}^{\,2}}{v_{\text{th}}^2}] \ =\ \int\limits_{\mathcal{D}_{\text{c}}} \mathrm{d}^3 g\ f(\vec{g})\ , \qquad \text{(A.1)}$$

where v_{cr} and t_{cr} denote the critical normal and possible tangential impact speed while the binormal component, usually denoted as b_{cr}, has been omitted.

In order to solve Eq. (A.1) we change to spherical coordinates. The transformation reads $\mathrm{d}^3 g = g^2\ \sin\vartheta\ \mathrm{d}g\ \mathrm{d}\vartheta\ \mathrm{d}\varphi$, while $g_{\text{x}} = g\ \cos\varphi\ \sin\vartheta$, $g_{\text{y}} = g\ \sin\varphi\ \sin\vartheta$, and $g_{\text{z}} = g\ \cos\vartheta$. Or, $g_{\text{x}} = t_{\text{cr}}$, $g_{\text{y}} = b_{\text{cr}}$, and $g_{\text{z}} = v_{\text{cr}}$. The binormal component will be omitted and approximated as mentioned in Chapter 4 by $\varepsilon_{\text{B}} \approx \varepsilon_{\text{T}}$ i.e. $b_{\text{cr}} \approx t_{\text{cr}}$ for simplicity, which results in a φ-symmetric tangential cut-off speed. The corresponding velocity space $\mathcal{D}_{\text{c}}$ is illustrated in the left part Fig. A.1 and takes the shape of a cylinder given by normal v_{cr} and tangential critical speeds t_{cr}. With respect to the φ-symmetry there is only a rectangle to be considered further where ϑ and g can be expressed in terms of v_{cr} and t_{cr}. In order to cover the entire area we split it along its diagonal into part **A** and **B** referring to either ϑ or θ. The integration limits may then be expressed as

(**A**) $0 < \vartheta < \vartheta_{\text{A}} = \arctan(t_{\text{cr}}/v_{\text{cr}})$ and $0 < g < g_{\text{A}} = v_{\text{cr}}\sqrt{1+\tan^2\vartheta}$,

(**B**) $0 < \theta < \theta_{\text{B}} = \arctan(v_{\text{cr}}/t_{\text{cr}})$ and $0 < g < g_{\text{B}} = t_{\text{cr}}\sqrt{1+\tan^2\theta}$,

where the identity $1+\tan^2 x = \cos^{-2} x = \sec^2 x$ has been applied.

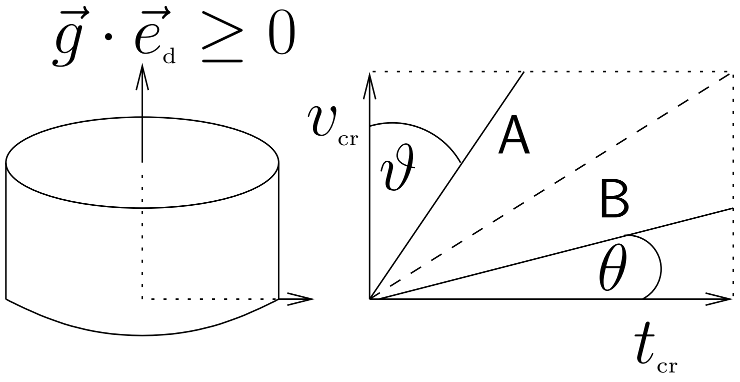

Figure A.1: The shape of the velocity volume considered is a cylinder. Due to the φ-symmetry the integration domain is further given by a rectangle and may be divided according to limits described in **A** and **B**. The integration is split into two parts referring to either ϑ or θ.

Accordingly, the integral is split into two parts and yields

$$\begin{aligned}\int\limits_{\mathcal{D}\mathrm{c}} \mathrm{d}^3g\, f(\vec{g}) &= 2\pi\left[\ \mathrm{Integral}_{\mathbf{A}} \ + \ \mathrm{Integral}_{\mathbf{B}}\ \right] \\ &= 2\pi\left[\left\{\int\limits_0^{\vartheta_{\mathbf{A}}} \mathrm{d}\vartheta \sin\vartheta \int\limits_0^{g_{\mathbf{A}}} \mathrm{d}g\, g^2\, f(\vec{g})\right\} + \left\{\int\limits_0^{\theta_{\mathbf{B}}} \mathrm{d}\theta \sin\theta \int\limits_0^{g_{\mathbf{B}}} \mathrm{d}g\, g^2\, f(\vec{g})\right\}\right] .\end{aligned} \tag{A.2}$$

The integrals evaluate to

$$\begin{aligned}\mathrm{Integral}_{\mathbf{A}} &= 2\pi \int\limits_0^{\vartheta_{\mathbf{A}}} \mathrm{d}\vartheta\ \sin\vartheta \int\limits_0^{g_{\mathbf{A}}} \mathrm{d}g\, g^3 \exp[-\frac{g^2}{v_{\mathrm{th}}^2}] \\ &= \pi v_{\mathrm{th}}^4 \left\{ 1 - \sqrt{\left(1+\frac{t_{\mathrm{cr}}^2}{v_{\mathrm{cr}}^2}\right)^{-1}} - \exp\left[-\frac{v_{\mathrm{cr}}^2}{v_{\mathrm{th}}^2}\right] \right. \\ &\quad + \sqrt{\left(1+\frac{t_{\mathrm{cr}}^2}{v_{\mathrm{cr}}^2}\right)^{-1}} \exp\left[-\frac{v_{\mathrm{cr}}^2}{v_{\mathrm{th}}^2}\left(1+\frac{t_{\mathrm{cr}}^2}{v_{\mathrm{cr}}^2}\right)^{-1}\right] \\ &\quad + \frac{v_{\mathrm{cr}}}{v_{\mathrm{th}}}\sqrt{\pi}\left(\mathrm{Erf}\left[\frac{v_{\mathrm{cr}}}{v_{\mathrm{th}}}\sqrt{1+\frac{t_{\mathrm{cr}}^2}{v_{\mathrm{cr}}^2}}\right] - \mathrm{Erf}\left[\frac{v_{\mathrm{cr}}}{v_{\mathrm{th}}}\right]\right) \\ &\quad \left. - \frac{v_{\mathrm{cr}}}{v_{\mathrm{th}}}\frac{\sqrt{\pi}}{2}\left(\mathrm{Erf}\left[\frac{v_{\mathrm{cr}}}{v_{\mathrm{th}}}\sqrt{1+\frac{t_{\mathrm{cr}}^2}{v_{\mathrm{cr}}^2}}\right] - \mathrm{Erf}\left[\frac{v_{\mathrm{cr}}}{v_{\mathrm{th}}}\right]\right) \right\} ,\end{aligned} \tag{A.3}$$

which can be further simplified, and reads

$$\begin{aligned}\mathrm{Integral}_{\mathbf{A}} &= \pi v_{\mathrm{th}}^4 \left\{ 1 - \exp\left[-\frac{v_{\mathrm{cr}}^2}{v_{\mathrm{th}}^2}\right] - \sqrt{\left(1+\frac{t_{\mathrm{cr}}^2}{v_{\mathrm{cr}}^2}\right)^{-1}} \left(1 - \exp\left[-\frac{v_{\mathrm{cr}}^2}{v_{\mathrm{th}}^2}\left(1+\frac{t_{\mathrm{cr}}^2}{v_{\mathrm{cr}}^2}\right)^{-1}\right]\right) \right. \\ &\quad \left. + \frac{\sqrt{\pi}}{2}\frac{v_{\mathrm{cr}}}{v_{\mathrm{th}}}\left(\mathrm{Erf}\left[\frac{v_{\mathrm{cr}}}{v_{\mathrm{th}}}\sqrt{1+\frac{t_{\mathrm{cr}}^2}{v_{\mathrm{cr}}^2}}\right] - \mathrm{Erf}\left[\frac{v_{\mathrm{cr}}}{v_{\mathrm{th}}}\right]\right) \right\} .\end{aligned} \tag{A.4}$$

In order to evaluate the 2^{nd} part, **B**, it is sufficient to exchange v_{cr} and t_{cr}, i.e. $g_{\mathbf{A}}$ becomes $g_{\mathbf{B}}$ and $\vartheta_{\mathbf{A}}$ becomes $\theta_{\mathbf{B}}$, respectively.

$$\begin{aligned}\mathrm{Integral}_{\mathbf{B}} \;=\; \pi v_{\mathrm{th}}^{4} & \left\{ 1-\exp\left[-\frac{t_{\mathrm{cr}}^{2}}{v_{\mathrm{th}}^{2}}\right]-\sqrt{\left(1+\frac{v_{\mathrm{cr}}^{2}}{t_{\mathrm{cr}}^{2}}\right)^{-1}}\left(1-\exp\left[-\frac{t_{\mathrm{cr}}^{2}}{v_{\mathrm{th}}^{2}}\left(1+\frac{v_{\mathrm{cr}}^{2}}{t_{\mathrm{cr}}^{2}}\right)^{-1}\right]\right)\right. \\ & \left. +\frac{\sqrt{\pi}}{2}\frac{t_{\mathrm{cr}}}{v_{\mathrm{th}}}\left(\mathrm{Erf}\left[\frac{t_{\mathrm{cr}}}{v_{\mathrm{th}}}\sqrt{1+\frac{v_{\mathrm{cr}}^{2}}{t_{\mathrm{cr}}^{2}}}\right]-\mathrm{Erf}\left[\frac{t_{\mathrm{cr}}}{v_{\mathrm{th}}}\right]\right)\right\} . \qquad (A.5)\end{aligned}$$

The relative size of the phase space volume $\tilde{\mathcal{C}}\ (v_{\mathrm{th}},v_{\mathrm{cr}},t_{\mathrm{cr}})$ then reads according to Eq. (A.1)

$$\tilde{\mathcal{C}}\ (v_{\mathrm{th}},v_{\mathrm{cr}},t_{\mathrm{cr}}) \;=\; \int\limits_{\mathcal{D}_{\mathrm{C}}} \mathrm{d}g\ g^{3}\ \exp[-\frac{g^{2}}{v_{\mathrm{th}}^{2}}] \;=\; 2\pi[\ \mathrm{Integral}_{\mathbf{A}} \ +\ \mathrm{Integral}_{\mathbf{B}}\ ]\ . \qquad (A.6)$$

Its asymptotic behavior is given by

$$\lim_{t_{\mathrm{cr}}\to\infty}\tilde{\mathcal{C}}\ (v_{\mathrm{th}},v_{\mathrm{cr}},t_{\mathrm{cr}}) \;=\; \pi v_{\mathrm{th}}^{4}\left\{1-\exp\left[-\frac{v_{\mathrm{cr}}^{2}}{v_{\mathrm{th}}^{2}}\right]+\frac{\pi}{2}\frac{v_{\mathrm{cr}}}{v_{\mathrm{th}}}\left(1-\mathrm{Erf}\left[\frac{v_{\mathrm{cr}}}{v_{\mathrm{th}}}\right]\right)\right\}, \qquad (A.7)$$

$$\lim_{v_{\mathrm{cr}}\to\infty}\tilde{\mathcal{C}}\ (v_{\mathrm{th}},v_{\mathrm{cr}},t_{\mathrm{cr}}) \;=\; \pi v_{\mathrm{th}}^{4}\left\{1-\exp\left[-\frac{t_{\mathrm{cr}}^{2}}{v_{\mathrm{th}}^{2}}\right]+\frac{\pi}{2}\frac{t_{\mathrm{cr}}}{v_{\mathrm{th}}}\left(1-\mathrm{Erf}\left[\frac{t_{\mathrm{cr}}}{v_{\mathrm{th}}}\right]\right)\right\}, \qquad (A.8)$$

while the limiting value reads

$$\lim_{t_{\mathrm{cr}}\to\infty}\ \lim_{v_{\mathrm{cr}}\to\infty}\tilde{\mathcal{C}}\ (v_{\mathrm{th}},v_{\mathrm{cr}},t_{\mathrm{cr}}) \;=\; \pi v_{\mathrm{th}}^{4}\ . \qquad (A.9)$$

Thus, (A.7) and (A.8) refer to integration domains $g\in[0,v_{\mathrm{cr}}/\cos\vartheta]$ and $\vartheta\in[0,\pi/2]$, and $g\in[0,t_{\mathrm{cr}}/\sin\vartheta]$ and $\vartheta\in[0,\pi/2]$, respectively, while still $\varphi\in[0,2\pi]$.

However, instead of using single components of the critical velocity, the absolute value of $|\vec{g}_{\mathrm{cr}}|=g_{\mathrm{cr}}$ may be applied. Then, the phase space volume under consideration in that case is not a cylinder anymore as illustrated in Fig. A.1, but a half-sphere of radius g_{cr} since, as before, only approaching particles are able to collide. Transforming Eq. (A.1) into spherical coordinates $\mathrm{d}^{3}g=g^{2}\ \sin\vartheta\ \mathrm{d}g\ \mathrm{d}\vartheta\ \mathrm{d}\varphi$, but applying appropriate integration limits as $g\in[0,g_{\mathrm{cr}}]$, $\varphi\in[0,2\pi]$, and $\vartheta\in[0,\pi/2]$ to become $\mathrm{d}^{3}g=2\pi g^{2}\ \mathrm{d}g$, yields

$$\begin{aligned}\tilde{\mathcal{C}}\ (v_{\mathrm{th}},g_{\mathrm{cr}}) &= \int\limits_{\mathcal{D}_{\mathrm{C}}}\mathrm{d}^{3}g\ f(\vec{g}) \;=\; 2\pi\int\limits_{0}^{g_{\mathrm{cr}}}\mathrm{d}g\ g^{3}\ \exp[-\frac{g^{2}}{v_{\mathrm{th}}^{2}}] \qquad (A.10)\\ &= \pi v_{\mathrm{th}}^{4}\left\{1-\left(1+\frac{g_{\mathrm{cr}}^{2}}{v_{\mathrm{th}}^{2}}\right)\exp\left[-\frac{g_{\mathrm{cr}}^{2}}{v_{\mathrm{th}}^{2}}\right]\right\}\ . \qquad (A.11)\end{aligned}$$

The asymptotic limit remains the same

$$\lim_{g_{\mathrm{cr}}\to\infty}\tilde{\mathcal{C}}\,(v_{\mathrm{th}},g_{\mathrm{cr}})=\pi v_{\mathrm{th}}^{4}\ . \qquad (A.12)$$

Appendix B

Discretization of the Integral Equation

In the following a brief overview of the discretization of Eq. (4.32) is given. Gain and loss term must be transformed independently. Since the transformation of the loss term is easier to perform we will start with the loss term and then consider the gain term.

Equation (4.32) can be written as

$$\frac{\partial}{\partial t}\,n(M,\vec{r},t) \;=\; \left[\frac{\partial}{\partial t}\,n(M)\right]_{\mathcal{G}} - \left[\frac{\partial}{\partial t}\,n(M)\right]_{\mathcal{L}} \tag{B.1}$$

where the spatial dependence has been dropped for simplicity. The loss term may be split in two parts

$$\left[\frac{\partial}{\partial t}\,n(M)\right]_{\mathcal{L}} \;=\; n(M)\int\limits_{0}^{\infty}\mathrm{d}m\;K(m,M)\;n(m) \tag{B.2}$$

$$=\; n(M)\int\limits_{0}^{M}\mathrm{d}m\;K(m,M)\;n(m)+n(M)\int\limits_{M}^{\infty}\mathrm{d}m\;K(m,M)\;n(m) \tag{B.3}$$

$$=\; [\;\;\mathrm{Integral}_{\mathbf{1}} \;\;+\;\; \mathrm{Integral}_{\mathbf{2}}\;\;]\;. \tag{B.4}$$

Integral$_{\mathbf{1}}$ and Integral$_{\mathbf{2}}$ may be separately transformed into

$$\mathrm{Integral}_{\mathbf{1}} \;=\; \int\limits_{0}^{\infty}\mathrm{d}m_1\int\limits_{0}^{m_1}\mathrm{d}m_2\;\delta(m_1-M)\;K(m_1,m_2)\;n(m_1)\;n(m_2) \tag{B.5}$$

and

$$\mathrm{Integral}_{\mathbf{2}} \;=\; \int\limits_{0}^{\infty}\mathrm{d}m_2\int\limits_{m_2}^{\infty}\mathrm{d}m_1\;\delta(m_2-M)\;K(m_1,m_2)\;n(m_1)\;n(m_2)\;. \tag{B.6}$$

Note, that a symmetric kernel $K(m_1,m_2) = K(m_2,m_1)$ has been assumed and denotes a crucial condition to ensure mass conservation. Transforming the integration domain

$$\left.\begin{array}{c} 0\le m_2\le\infty \\ m_2\le m_1\le\infty \end{array}\right\}\Longleftrightarrow\left\{\begin{array}{l} 0\le m_1\le\infty \\ 0\le m_2\le m_1 \end{array}\right. \tag{B.7}$$

Integral$_2$ may be written as

$$\text{Integral}_2 = \int\limits_0^{\infty} \mathrm{d}m_1 \int\limits_0^{m_1} \mathrm{d}m_2\ \delta(m_2 - M)\ K(m_1,m_2)\ n(m_1)\ n(m_2)\ . \tag{B.8}$$

The actual discretization is done according to

$$\int \mathrm{d}m_1 \longrightarrow \sum_{im_1} \Delta m_1 \quad \text{and} \quad \int \mathrm{d}m_1\ \delta(m_1 - M) \longrightarrow \sum_{im_1} \delta_{im_1,iM}\ . \tag{B.9}$$

Then, Eq. (B.2) may be rewritten using $L(m_1,m_2) = K(m_1,m_2)n(m_1)n(m_2)$ and Eqs. (B.5) and (B.8)

$$\begin{aligned}\left[\frac{\partial}{\partial t}\, n(M)\right]_{\mathcal{L}} &= \int_0^{\infty} \mathrm{d}m_1 \int_0^{m_1} \mathrm{d}m_2\ \delta(m_1 - M)\ L(m_1,m_2) \\ &\quad + \int_0^{\infty} \mathrm{d}m_1 \int_0^{m_1} \mathrm{d}m_2\ \delta(m_2 - M)\ L(m_2,m_1) &\text{(B.10)} \\ &\Longrightarrow \sum_{im_1=0}^{\infty} \sum_{im_2=0}^{im_2 \le im_1} \Delta m_{im_2}\ \delta_{im_1,iM}\ L(im_1,im_2) \\ &\quad + \sum_{im_1=0}^{\infty} \sum_{im_2=0}^{im_2 \le im_1} \Delta m_{im_1}\ \delta_{im_2,iM}\ L(im_1,im_2) &\text{(B.11)}\end{aligned}$$

Equation (B.11) is then implemented in numerical algorithms. The gain term is treated in a similar manner and reads

$$\left[\frac{\partial}{\partial t}\, n(M)\right]_{\mathcal{G}} \Longrightarrow \sum_{im_1=0}^{\infty} \sum_{im_2=0}^{im_2 \le im_1} \Delta m_{im_1}\ \Delta m_{im_2}\ L(im_1,im_2)\ \frac{(m_{im_1} + m_{im_2})}{\Delta M_{iM} M_{iM}}\ . \tag{B.12}$$

In this way the conservation of mass is exactly enforced, which can be proven by similar transformations as above.